

**Characterization of Mixture Formation and
Combustion Processes of Diesel Spray of Multi-Hole
Injector with Split Injection Strategy**

**(多噴孔ディーゼルインジェクタ噴霧の分割噴射時の混
合気形成と燃焼過程の特性解析)**

By

(Samir Chandra Ray)

Dissertation

Submitted in Partial Fulfillment of the Requirements for the
Degree of Doctor of Engineering

at

Mechanical Power and Motor Systems Laboratory

Department of Mechanical Systems Engineering

Graduate School of Engineering

Hiroshima University

September 2022

ABSTRACT

The fundamental concept of the Laser Absorption Scattering (LAS) technique is to understand the fuel concentration by attenuation of both visible and ultraviolet light. The intensity of visible light is only attenuated by the liquid scattering, while that of ultraviolet light is attenuated by vapors absorption as well as liquid scattering. The temperature dependence of the absorbance of the tracer fuel used in the dual-wavelength laser absorption and scattering method. The absorbance was measured in this study to acquire the molar absorption coefficient that was used to calculate the concentration of the air-fuel mixture using the tracer LAS method. Moreover, the effect of atmospheric pressure and temperature on absorbance was experimentally examined. The effects of the split ratio and dwell times on the mixture formation and combustion process of a diesel spray in a constant-volume chamber were experimentally investigated. The effects of the split ratio as well as dwell time were investigated when the total amount of fuel injection was 5.0 mg/hole. Three split ratios were selected: 3:7, 5:5, and 7:3, while the dwell time of 0.12 ms was same for every condition. Again, three dwell times were chosen, i.e. 0.12, 0.32, and 0.54 ms, with a same split ratio of 7:3. A laser absorption-scattering technique was employed to observe the mixture formation with regarding to the equivalence ratio. A high-speed video camera was employed to record the natural flame luminosity, and a two-color pyrometer technique was employed to evaluate the temperature and soot concentrations in the flame. In the experiment, a commercial seven-hole injector with a hole diameter of 0.123 mm allowing high injection pressure up to 100 MPa was used to avoid the potential inconsistencies with single-hole test injector. The diesel surrogate fuel which consists of 97.5 % n-tridecane and 2.5 % of volume-based 1-methylnaphthalene was used. Among the distribution ratios tested in this study, the 7:3 split ratio exhibited the best performance for the lean mixture formation considering the overall equivalence ratio distribution. In the shortest dwell time of 0.12 ms, the equivalence ratio distribution decreases uniformly from the rich mixture region to the lean mixture region. For the 7:3 split ratio, the interaction of the burned gas with the ambient gas inside the combustion chamber during the injection pause time promoted combustion and reduced soot oxidation. Consequently, 0.12 ms can be considered the optimal dwell time due to the ignition delay and relatively low soot emission afforded.

The conventional LAS uses the ND: YAG pulse laser, CCD cameras and one shot for one spray, which takes time and effort. Moreover, temporal variation measurement of a single shot spray is not possible by the conventional LAS. To record the distribution of the whole vapor phase in an injection event and measure the liquid and vapor concentration inside the spray, a high-speed laser absorption scattering (HS-LAS) method was established applying continuous diode light source, high-speed video cameras, and image intensifier for UV light, which can provide the temporal variation of a single shot spray. Furthermore, the injection amounts were set as 2.5 as well as 5.0 mg/hole to examine the effect of the injection mass on the diesel spray characteristics and mixture formation process by using this new method.

TABLE OF CONTENTS

ABSTRACT.....	I
TABLE OF CONTENTS	III
NOMENCLATURES	VI
CHAPTER 1 INTRODUCTION.....	1
1.1 BACKGROUND AND MOTIVATION.....	1
1.2 OBJECTIVE AND APPROACHES	5
1.3 OUTLINE	6
1.4 REVIEW OF PREVIOUS WORKS.....	7
1.4.1 Characterization of Diesel Spray.....	7
1.4.2 Characterization of Diesel Combustion.....	11
1.4.3 Multiple Injection.....	15
1.4.4 Optical Diagnostic Techniques for Spray and Combustion.....	18
CHAPTER 2 EXPERIMENTAL APPERATUS AND MEASURING METHODS	24
2.1 HIGH-PRESSURE AND HIGH-TEMPERATURE CONSTANT VOLUME CHAMBER.....	24
2.2 FUEL INJECTION SYSTEM.....	25
2.3 INJECTION RATE MEASUREMENT SYSTEM	26
2.4 TRACER LAS TECHNIQUE FOR MIXTURE CONCENTRATION MEASUREMENT.....	28
2.4.1 Principle of Tracer Laser Absorption Scattering (LAS) Technique ...	28
2.4.2 Optical Arrangement for LAS System.....	32
2.4.3 Tracer LAS Fuel Selection	33
2.5 HIGH-SPEED LAS SYSTEM.....	35
2.5.1 Specification of Light Source and Image Intensifier	35
2.5.2 Optical Arrangement for HS-LAS System	36
2.5.3 Multi-Hole Injector Adaptor and Image Processing Area.....	38
2.6 MOLAR ABSORPTION COEFFICIENT MEASUREMENT	40

2.6.1	Principle of Molar Absorption Coefficient	40
2.6.2	Problems with Conventional Absorbance Measurement.....	40
2.6.3	Improvement of Problem	41
2.6.4	Experimental Setup	42
2.6.5	Operation Procedure	43
2.7	TWO-COLOR PYROMETRY FOR FLAME TEMPERATURE AND SOOT CONCENTRATION MEASUREMENT.....	43
2.7.1	Experimental Setup	43
2.7.2	Principle of Two-Color Pyrometry.....	44
2.7.3	Calibration Method	45
CHAPTER 3 MOLAR ABSORPTION COEFFICIENT OF TRACER LAS TEST FUEL.....		
3.1	INTRODUCTION.....	47
3.2	EXPERIMENTAL CONDITIONS	48
3.3	RESULTS AND DISCUSSION.....	49
3.3.1	Absorption Spectrum.....	49
3.3.2	Temporal Variation of 266 nm Absorbance	51
3.3.3	Correlation Between the Absorbance and the Concentration	55
3.3.4	Molar Absorption Coefficient on the Effect of Atmospheric Temperature and Pressure	56
3.4	SUMMARY.....	58
CHAPTER 4 SPLIT INJECTION ON MIXTURE FORMATION AND COMBUSTION.....		
4.1	INTRODUCTION.....	60
4.2	EXPERIMENTAL CONDITIONS	61
4.3	EFFECT OF SPLIT RATIO	63
4.3.1	Injection Rate	63
4.3.2	Spray Mixture Concentration Distribution.....	63
4.3.3	Spray Combustion Characteristics	69

4.4	EFFECT OF DWELL TIME	81
4.4.1	Injection Conditions and Injection Rate.....	81
4.4.2	Spray Mixture Concentration Distribution.....	82
4.4.3	Spray Combustion Characteristics	88
4.5	SUMMARY.....	94
CHAPTER 5 TEMPORAL DEVELOPMENT OF MIXTURE DISTRIBUTION OF FUEL SPRAY		96
5.1	INTRODUCTION.....	96
5.2	EXPERIMENTAL CONDITIONS	97
5.3	RESULT AND DISCUSSION.....	99
5.3.1	Comparison of UV and Vis Optical Thickness of Non-Evaporating Spray	99
5.3.2	Optical Thickness Images.....	100
5.3.3	Comparison of Fuel Mass of Completely Evaporated Spray and Injected Mass	103
5.3.4	Axisymmetric Analysis	104
5.3.5	Non-Axisymmetric Analysis.....	109
5.4	SUMMARY.....	114
CHAPTER 6 CLOSURE.....		116
RECOMMENDATIONS FOR FUTURE WORKS		120
AKNOWLEDGEMENT.....		121
REFERENCES.....		122

NOMENCLATURES

ASOI	After Start of Injection
ASOE	After Start of Energize
α -MN	α Methyl naphthalene
BSFC	Brake Specific Fuel Consumption
C_d	Mass Concentration of Droplets, kg/m^3
C_v	Mass Concentration of Vapor, kg/m^3
CCD	Charge-Coupled Device
CDC	Conventional Diesel Combustion
CF	Correction Factor
CI	Compression Ignition
CIDI	Compression Ignition Direct Injection
CO	Carbon Monoxide
CVSC	Constant Volume Spray Chamber
D	Injector Hole Diameter, mm
D.I.	Direct Injection
DBI	Diffused Back-illumination Imaging
DMN	Dimethyl naphthalene
DT	Dwell Time
ϵ	Molar Absorption Coefficient
ECN	Engine Combustion Network
EGR	Exhaust Gas Recirculation
EOI	End of Injection
HCCI	Homogeneous Charge Compression Ignition

HCPC	Homogenous Charge Progressive Combustion
HD	Heavy Duty
HS-LAS	High Speed Laser Absorption Scattering
HSV	High-Speed Video
HRR	Heat Release Rate
ICE	Internal Combustion Engines
LAS	Laser Absorption Scattering
LDV	Laser Doppler Velocimetry
LIEF	Laser Induced Exciplex Fluorescence
LIF	Laser Induced Fluorescence
LRS	Laser Rayleigh Scattering
LTC	Low Temperature Combustion
LRS	Laser Rayleigh Scattering
LIF	Laser Induced Fluorescence
ND	Natural-density
PCCI	Premixed Charge Compression Ignition
PIV	Particle Image Velocimetry
P_{inj}	Injection Pressure
PLRS	Planar Laser Rayleigh Scattering
PM	Particulate Matter
PODE	Polyoxymethylene Dimethyl Ethers
PPI	Partially Premixed Combustion
RCCI	Reactivity-Controlled Compression Ignition
SI	Spark Ignition
SMD	Sauter Mean Diameter

SOI	Start of Injection
STP	Spray Tip Penetration
SRS	Spontaneous Raman Scattering
TDC	Top Dead Center
UHC	Unburned Hydrocarbons
UV	Ultraviolet
Vis	Visible

CHAPTER 1 INTRODUCTION

1.1 BACKGROUND AND MOTIVATION

Since 1876, when N. A. Otto invented the first four-stroke spark ignition (SI) engine as well as 1892, when R. Diesel developed the compression ignition (CI) engine, where the internal combustion (IC) engine has undergone continual development to meet the consecutively increasing demands of the mankind. It might have been assumed that the IC engine would have been perfected after so many years of development. On the contrary, each decade seems to bring with it new challenges. The most recent challenge has been the air pollution in the environment. Diesel engines emit two main pollutants: particulate matter (PM) and nitrogen oxides (NO_x), both are detrimental to the environment and public health [1].

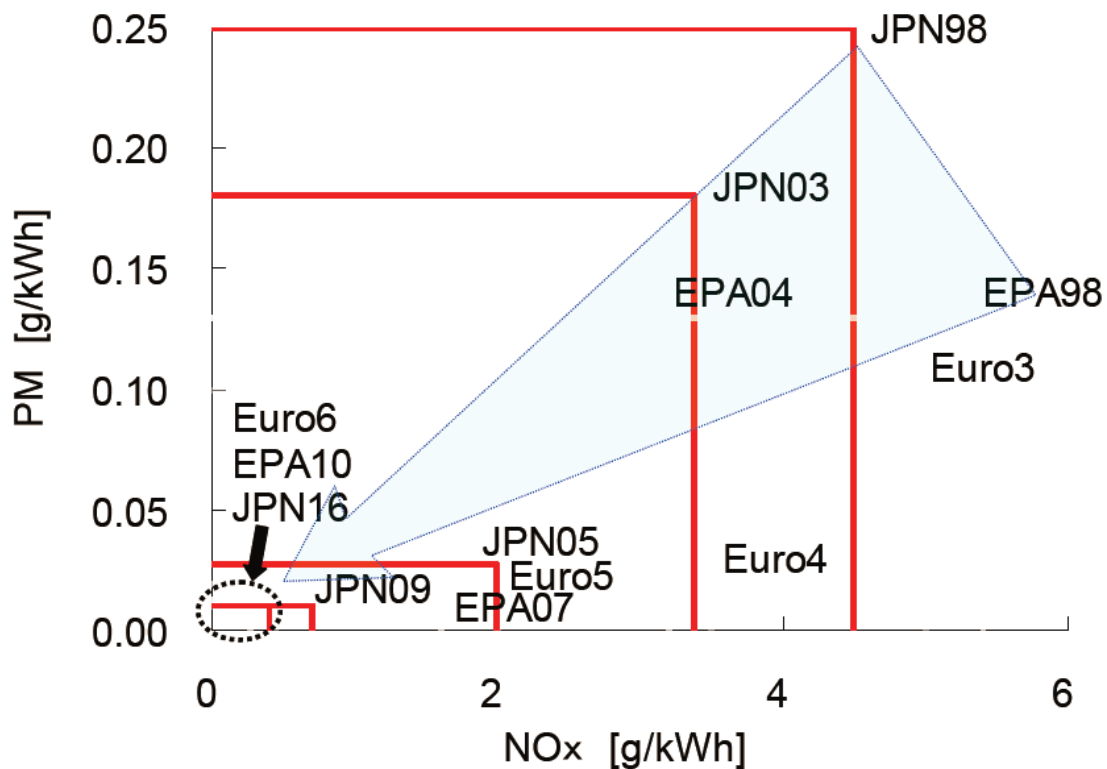


Fig. 1.1 Regulation of PM and NO_x Emission of Diesel Engines.

Besides, the issue of greenhouse gases contributing to global warming has gotten a lot of global attention. Therefore, in the next decades, the automotive sector should be particularly concerned with reducing carbon dioxide emissions as well as increasing fuel efficiency [2]. Fig. 1.1 depicts the progressive tightening of non-road diesel exhaust emission regulations in the world's major markets from the past to the future [3].

In order to achieve a fresh diesel engine, the innovative combustion concepts that are expected to be able to concurrently minimize PM and NO_x emission are offered such as Homogeneous Charge Compression Ignition (HCCI), Homogenous Charge Progressive Combustion (HCPC), Low Temperature Combustion (LTC), Premixed Charge Compression Ignition (PCCI), Reactivity Controlled Compression Ignition (RCCI) et al. These innovative combustion concepts can achieve satisfactory performance while reducing PM and NO_x emissions and limiting engine expenses.

Homogeneous Charge Compression Ignition (HCCI) was originally introduced in 1958 [4] to the concept of diesel purification in the intake port. HCCI is a type of internal combustion where the fuel and oxidizer are thoroughly combined and compressed to the point of auto-ignition. Clean combustion, high efficiencies, and low emissions are all advantages of this technique.

Homogenous Charge Progressive Combustion (HCPC) is established in a split-cycle system with out-of-cylinder intake as well as compression stages [5]. The maximum efficiency, noiseless, and smooth engine performance can be attained for a given maximum allowable pressure. The lack of pressure peaks and the accompanying decrease in reciprocating masses increase mechanical efficiency.

Low Temperature Combustion (LTC) is intended to eliminate or minimize the two furthest harmful pollutants released by diesel engines: particulate matter (PM) and nitrogen oxides (NO_x). NO_x emissions are harmful, and when they combine with other air contaminants, they cause ozone at ground level, often known as smog. PM is made up of black soot particles that are frequently drenched in unburned or partially burnt fuel [6].

Premixed Charge Compression Ignition (PCCI) is a compromise that combines CIDI (Compression Ignition Direct Injection) combustion control with HCCI exhaust gas emissions reduction, notably lower soot emissions [7]. By creating the combustible mixture such that combustion occurs over a longer time, decreasing the possibility of knocking, the heat release rate (HRR) can be maintained.

Reactivity Controlled Compression Ignition (RCCI) is known as the dual-fuel engine combustion system established at the engine research center of Wisconsin-Madison university [8]. RCCI is the updated method of HCCI (Homogeneous Charge Compression Ignition) technique which can provides greater combustion control and

has the potential to considerably reduce fuel consumption and pollutants. Lower PM and NO_x emissions, increased fuel efficiency, loss of low heat transfer, and no need for expensive after-treatment equipment are all advantages of this type of combustion. Fig. 1.2 indicates the ϕ -T map for the soot emissions as well as NO_x formation [9]. On the diagram, the normal combustion areas of Homogeneous Charge Compression Ignition (HCCI), conventional diesel combustion (CDC), HCCI, and

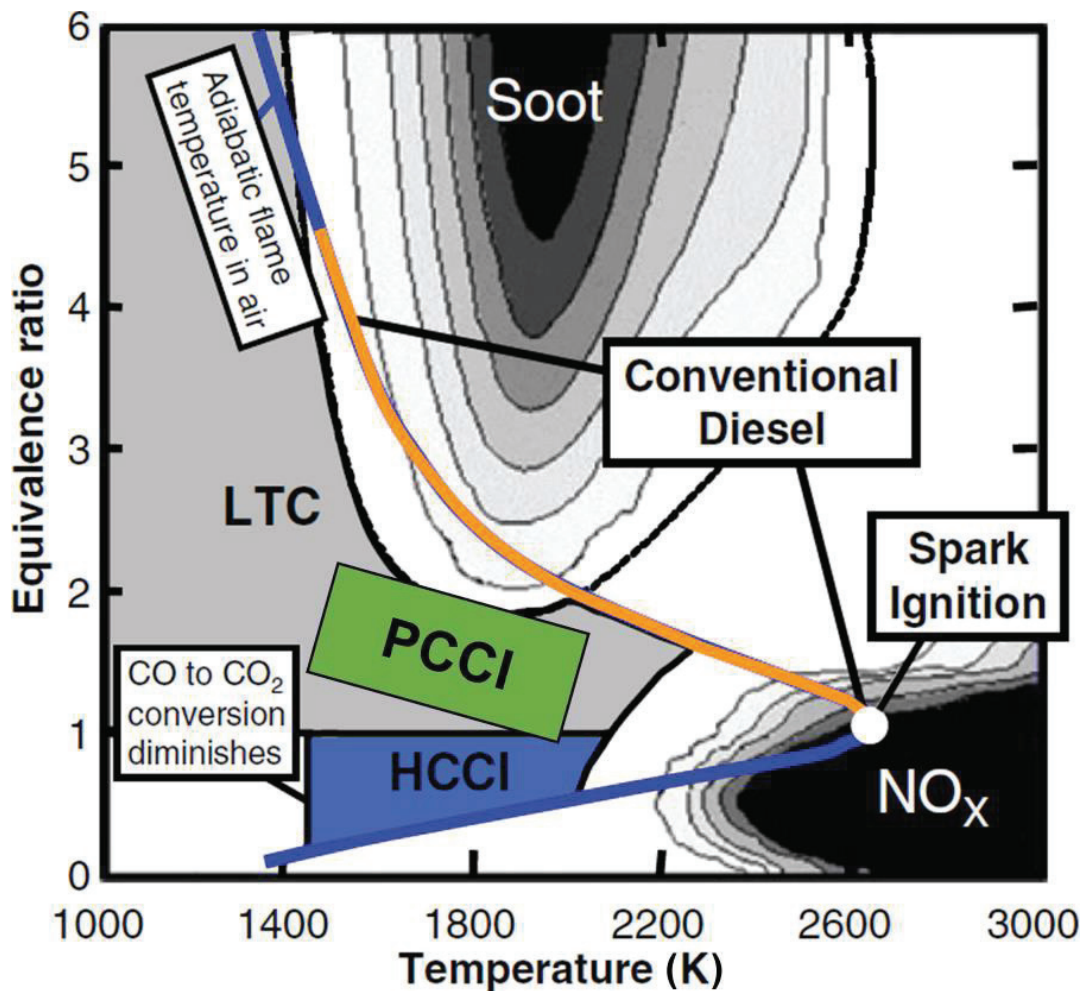


Fig. 1.2 Illustration of HCCI, CDC and PCCI regions on a ϕ -T map with soot-NO_x contour.

PCCI have been marked [10, 11]. The main objective is to keep the combustion region away from the soot and NO_x outlines, which will reduce both emissions simultaneously.

Numerous studies were undertaken in order to investigate and visualize the diesel sprays. The most used technique is to attach the fuel injector into the constant volume chamber and inject the test fuel inside the chamber at a fixed ambient condition. The

single-hole injector is broadly used in the experiments for comprehensive study and well optical arrangement. It is simpler to comprehend the impacts of specific regulating factors when only one spray plume is present since it does not interfere with any nearby spray plumes or block the optical path. The spray can be examined at room temperature and low pressure condition to investigate the behaviors of non-evaporating spray [12,13]. In addition, it can be examined at high temperature condition to evaluate the behaviors of an evaporating spray and replicate the conditions of a real engine. In order to forecast vapor penetration, mixture formation, and equivalence ratio distribution for non-reacting spray [14-21] and emission formation process for combustion spray [22, 23], a precise spray model has been developed. In engines, multi-hole injectors are employed, thus it's important to know the main difference between multi- and single-hole injectors. The varied internal flow parameters within the nozzle's sac volume and particularly at low needle lift are the primary causes of the variation in spray behavior [24, 25].

To investigate the precise physical events of multiple injections, most researchers focus on the process of interaction of the injection pulses. To decrease combustion noise, improve soot oxidation, and NOx emissions multiple injections have been broadly used [26]. The word "split injection" is used in some cases to denote the multiple injection technique where the main injection is divided into two tiny injections of the same size or divided into a tiny pre-injection followed by the main injection [27]. The combustion for the split injection is the result of the reaction of the first and second injections. The first injection control is dominated by the ambient condition and its own mixture formation process, whereas the second injection control includes the following specifications and depends on the first injection results. The combustion of the first injection significantly influences the ignition time of the second injection fuel [28].

The operating conditions for engines and fuel injection systems, diagnostic equipment, and numerical models have changed dramatically in recent years. Since the early 1970, injection pressures have increased by an order of magnitude. Inline pumps, unit injectors, and more recently common-rail injectors have been used in engines. Moreover, high-pressure fuel delivery systems, electronic controls of injection pressure have enabled split injection or multiple injections, as well as injection rate shaping [29, 30]. As a result of these changes, the physical process of atomization and vaporization of diesel fuel is becoming increasingly complicated. This has had a significant impact

on the development of spray diagnostics [31]. The liquid phase of diesel spray penetration is much lower than previously thought has resulted in a radically new concept of diesel combustion [32] which is gaining traction among diesel engine engineers. The increasing awareness of air-fuel mixture formation process in diesel sprays will undoubtedly lead to advancements in the application of diesel injection technology, such as the NO_x emissions reduction and particulate matter levels over the use of a split injection strategy.

1.2 OBJECTIVE AND APPROACHES

As stated in the preceding sections, the formation of an air-fuel mixture is extremely important to diesel combustion and emissions. A clear knowledge of the air-fuel mixing process is unquestionably essential for elucidating the mechanism of diesel combustion and emissions. The investigation of diesel spray can be used to characterize air-fuel mixing in diesel engines. However, the spray itself is a complicated flow that includes liquid breakup, atomization, interactions in aerodynamics, vaporization, and other processes. Although many researchers have been researched on the mechanisms of liquid breakup, atomization, and interactions in aerodynamics of a non-evaporating spray, and identification of the mechanisms is ongoing with the development of various diagnostics whereas our understanding of the characteristics of an evaporating spray is limited. This is due to a lack of reliable diagnostics for quantifying evaporating spray characteristics. Thus, it is crucial to establish a more accurate and reliable measurement or quantification technique that will allow researchers to study the behaviors of diesel spray evaporation.

The use of a high-pressure split-injection approach has been shown to improve atomization and allow Heavy-Duty (HD) diesel engines to produce lower levels of NO_x and particulates. The precise characterization of the spray process is a vital step toward comprehending the combustion process. Furthermore, by clarifying the mechanism of air-fuel mixture formation in split-injection diesel spray, much more will be benefited, not only in terms of recognizing a novel fuel-air mixing mechanism, but also in terms of determining what kind of spray formation method will be used in the next generation diesel engines.

The main objective of this research is to understand the behavior of the air-fuel mixture in diesel sprays injected into a diesel-like environment. The characterization of

evaporating diesel sprays with single and split injection is given special attention, providing detailed information on the temporal and spatial distributions of liquid phase and vapor phase of the spray, and correlating the characteristics of vaporization and air-fuel mixing with fuel injection systems. On the other hand, to achieve a reliable and detailed measurement of vapor concentration, the development of laser diagnostics allowing quantification of fuel distributions in a spray is also the objective of this paper. To be more specific, the following are the objectives of this research:

1. Molar absorption coefficient measurement of tracer LAS test fuel.
2. Investigate the effects of the split ratio on mixture formation, combustion, and soot characteristics of the diesel spray.
3. Analysis the effects of the dwell time for same split ratio on the mixing procedure, soot formation, and oxidation of diesel spray from a multihole injector.
4. Observe the mixture formation process and shot to shot variation of the spray on the effect of injection mass.

In this study, the tracer laser absorption scattering (LAS) method was applied to analyse the spray mixing process of the split injection diesel spray. In particular, spray behaviours such as the distribution of liquid and vapor phases, evaporation ratio, vapor penetration, and distribution of equivalence ratios were analysed. Additionally, the combustion processes were investigated using a high-speed video camera and measured using two-color pyrometry. Besides, the flame temperature and soot index distributions are discussed. Last of all, the high-speed laser absorption scattering (HS-LAS) technique for measuring quantitative information of vapor and liquid in fuel spray has been developed.

1.3 OUTLINE

The dissertation is organized in the following way to present this work: Chapter 1 is the introduction of former work on the multiple injection technique, mixture formation characteristics, direct injection diesel spray combustion techniques and the optical diagnostic systems for spray and combustion. The experimental equipment described in chapter 2 includes the high-temperature, high-pressure constant volume chamber, the injection rate measuring system, and the fuel injection system. Furthermore, the principle of Laser Absorption Scattering (LAS) technique, the optical

configuration of the LAS as well as the HS-LAS are presented in this chapter. Chapter 3 illuminates the vapor phase absorption spectrum of 1-methylnaphtalene and tracer fuel. The correlation between absorbance and concentration was investigated in this study. The molar absorptivity was calculated based on different ambient temperature and pressure. Chapter 4 clarifies the effects of split ratio and dwell time of diesel spray injection on mixture formation and combustion process. A laser absorption-scattering technique was adopted to examine the formation of mixtures with regarding to the equivalence ratio. A high-speed video camera was used to observe natural flame luminosity, and a two-color pyrometer system was employed to evaluate the temperature and soot concentrations in the flame. The temperature of the flame and distribution of soot concentrations expressed by the KL factor have been discussed, where K is the coefficient of absorption and L is the geometric stiffness including its spray flame along the optical detection axis. Chapter 5 irradiates the high-speed laser absorption scattering (HS-LAS) imaging of evaporating diesel spray and mixture formation process. The injection amounts were set as 2.5 and 5.0 mg/hole to observe the effect of the injection mass on the diesel spray characteristics and mixture formation process by using this technique. Finally, in Chapter 6, general conclusions on the mixture formation and combustion processes of the diesel spray with the split injection strategy and their temporal development / shot to shot variations are given.

1.4 REVIEW OF PREVIOUS WORKS

1.4.1 Characterization of Diesel Spray

In practically every aspect of human life, atomization processing has been used. Atomization processing is particularly important to internal combustion engines (ICE) for enhancing thermal efficiency and ensuring a clean combustion process. Spray characteristics have been shown in the study [33] which have a substantial influence on the combustion of ICE.

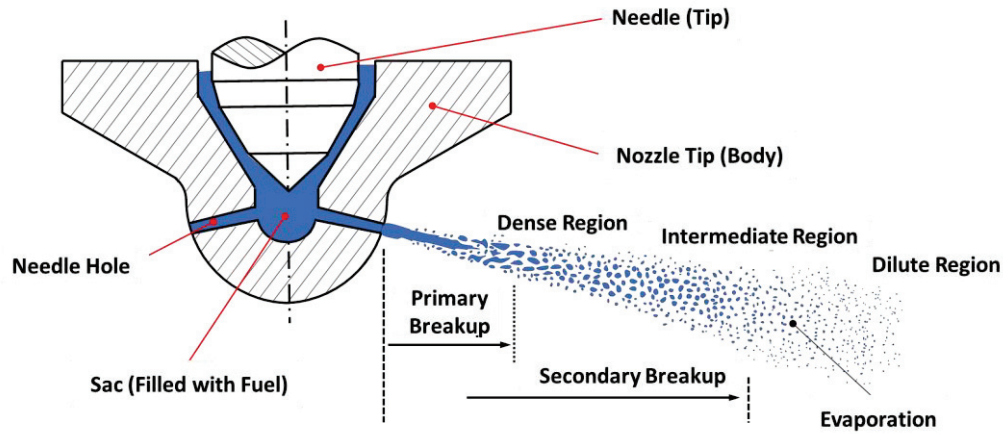


Fig. 1.3 Diagram of the development of the diesel spray.

Better diesel atomization can not only reduce the ignition delay but also the soot produced by diesel combustion [34]. Fig. 1.3 illustrates a schematic diagram of the development of the diesel spray [34].

Air entrainment is extensively studied because it frequently contributes to the secondary break-up process, which is typically caused by aerodynamic forces. In 1961, Ricou and Spalding presented an air entrainment coefficient for the "porous-wall technique," which involves injecting a turbulent gaseous jet into air at constant pressure. Using the hot wire anemometer, Ha et al. [35] investigated the gas flow characteristics around the spray as well as the temporal history. They found that ambient air enters mainly upstream of the spray, whereas air only passes away at the tip of the spray. Cossali et al. [36,37] used Laser Doppler Velocimetry (LDV) to study air entrainment into the transient Diesel spray. One of their findings was that during the main injection, the air entrainment rate is constant. However, they discussed the correlations between ambient gas density, gas entrained rate, and temperature as well as the surrounding air flow characteristics. The development of the Particle Image Velocimetry (PIV) system in recent decades has encouraged further research into mixture formation process. It is widely accepted that the surrounding gas flow can be separated into three sections on the basis of flow property using the PIV technique [38-[41]: the gas is initially spread apart with the spray head (region 1: head vortex zone), then it is re-circulated along on the head side (region 2: gas recirculation zone), and finally it is entrained into the next spray zone (near quasi static zone).

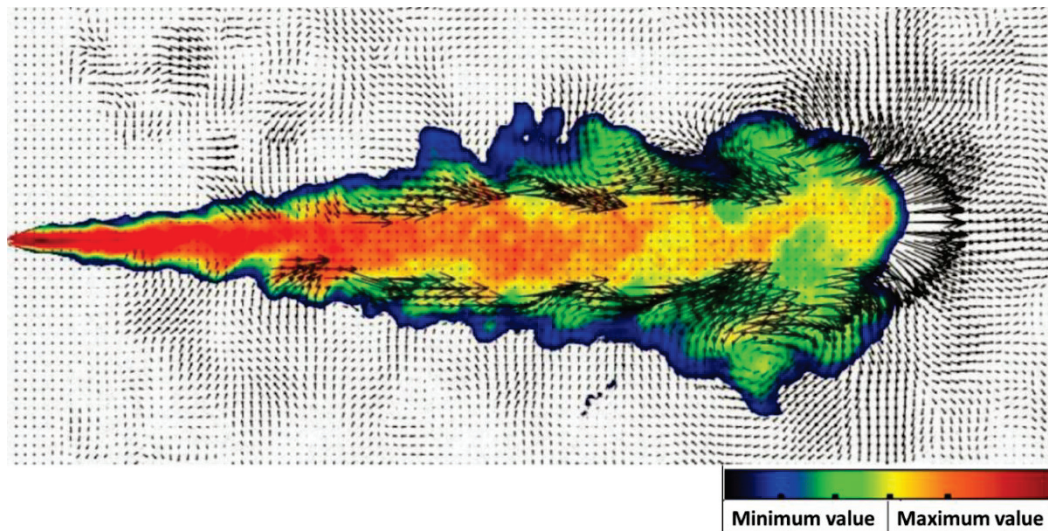


Fig. 1.4 Air entrainment and fuel concentration image of Diesel-like gas spray.

Fuel concentration in color scale and flow velocity in black vectors.

Bruneaux et al. [42] used Laser Induced Fluorescence (LIF) and Particle Image Velocimetry (PIV) techniques at the same time to investigate the correlation between fuel concentration and air entrainment inside the spray. In contrast to the previous researcher's findings, they discovered air entrainment in the re-circulation area, as displayed in Fig 1.4.

As liquid droplets and vapor coexist simultaneously in evaporating diesel spray, whereas the quantitative estimation becomes relatively challenging. Various diagnostic methods have been developed during the past few decades to establish such estimations. Two earlier optical diagnostic methods are shadowgraph and Schlieren imaging; these were mainly used to examine the qualitative information of the evaporating spray structure [43-45]. Holography is one of the exceptional methods to record the three-dimensional data of fuel spray by using the diffraction of laser light. It has demonstrated the ability to provide temperature distributions, velocity, droplet size and vapor concentration inside a fuel spray [46, 47]. But due to noise interference it can only provide estimations of low atmospheric vapor concentration and in moderate ambient density/temperature. Raman spectroscopy technique is applied for a line-imaging or single-point measurement of fuel-air ratio inside the combustion chamber [48-50]. Nevertheless, Raman scattering is such a weak process, it must be carefully considered in terms of signal-to-noise ratio. In addition, it takes a long time to investigate the entire spray zone with Raman spectroscopy.

Planar Laser Rayleigh Scattering (PLRS) is widely employed at low gas densities to get quantitative data on the vapor phase equivalency ratio [51,52]. Specially, strong scattering from liquid droplets must be suppressed in PLRS vapor estimations of an evaporating fuel spray. In other words, PLRS should not be used to estimate fuel vapor concentration when there are droplets present. It is important to highlight the Laser Induced Exciplex Fluorescence (LIEF) technology because it is frequently used to assess concentrations in both the liquid and vapor phases at the same time [53-56].

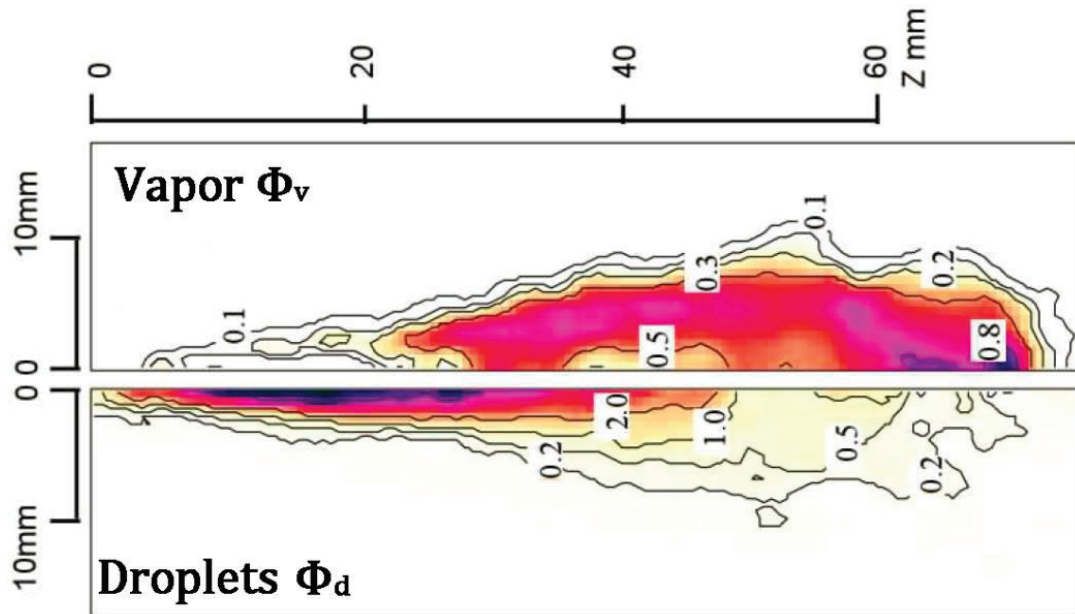


Fig. 1.5 Equivalence ratios of droplets and vapor obtain by LAS technique.

However, there are a number of issues with this measurement, including fluorescence suppression by air and cross-talk between exciplex (liquid) and monomer (vapor) excitation because of overlapping emission spectra. In addition, it's challenging to apply LIEF quantitatively to evaporating sprays with a high pressure, high-temperature ambient, because when the temperature surpasses 500K, the fluorescence is highly dependent on the temperature [55].

To determine the equivalency ratio distributions of the liquid and vapor phases of a spray that resembled Diesel, Zhang [57] used the Laser Absorption Scattering (LAS) method, as presented in Fig 1.5. According to the results, the high equivalence ratio of the liquid phase predominates upstream, while the large equivalence ratio vapor area, where auto-ignition is conceivable, is located close to the spray tip. The spray behaviours of non-evaporating and evaporating spray were investigated using multihole injectors with a single injection [58,59]. When compared to the non-evaporating spray

situation, the rise in ambient temperature results in the expansion of the evaporating spray's tail and a wider spray near the nozzle. The tail of the spray no longer resembles a clear cone shape. As the injection pressure and nozzle-hole diameter increase, this behaviour becomes more obvious. The spray head of the evaporating spray enlarges and assumes a mushroom-like appearance during the early stage of injection. The spray from the micro-hole injector can be twisted to generate a bigger spray head under extremely high injection pressure and evaporation.

1.4.2 Characterization of Diesel Combustion

The combustion of a diesel engine usually produces soot particles because of the incomplete oxidation. Meanwhile, the high temperature during combustion will cause NOx levels to rise. This has a negative effect on the environment and human health.

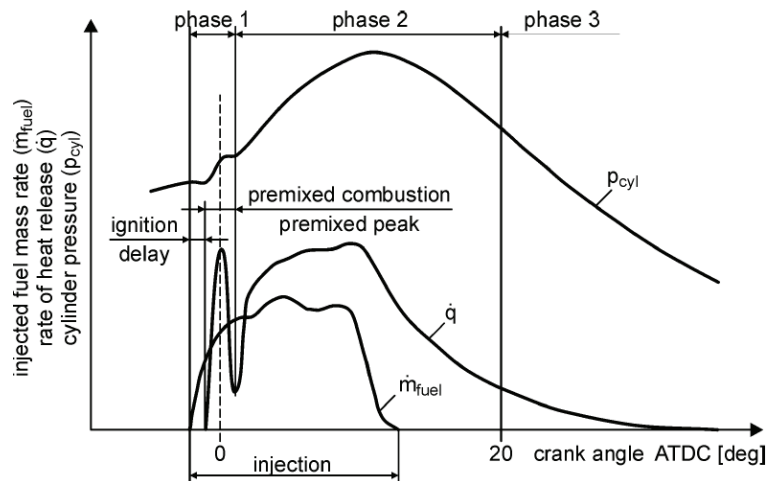


Fig. 1.6 Phases of the conventional diesel combustion process.

For diesel engines, a more efficient and cleaner combustion process is essential. The fuel properties, air-fuel mixing, evaporation, and ignition all play a significant role in controlling the combustion process throughout the diesel combustion mode. The in-cylinder gas pressure and temperature at top dead center (TDC), which range from 4 to 12 MPa and 1000 to 2000 K correspondingly, are both significantly higher in diesel engines than in gasoline engines due to the compression ratio [60]. The combustion process in a diesel engine is divided into three distinct phases, as illustrated in Fig. 1.6, and will be considered in detail further below.

The start of injection as well as the termination of premixed combustion mark the beginning of the first stage. Before top dead center, the fuel is injected via a multi-hole

injector into the combustion chamber at a high injection pressure; the injection duration is dependent on the fuel mass. When the liquid fuel begins to inject into the combustion chamber, it entrains the hot air, which results in the fuel-air mixture and vaporization. The air-fuel mixture is sufficient, and the heat release increases quickly when the ambient temperature reaches the auto-ignition point (greater than 750 K). Typically, this occurrence is referred to as the premixed peak. The first creation of NO_x is mostly caused by the high temperatures in the combustion chamber, while the intense pressure produces more noise. Temperatures of roughly 2000 K must be reached in order to break the triple bond of N₂-molecules and allow for the creation of NO_x [61].

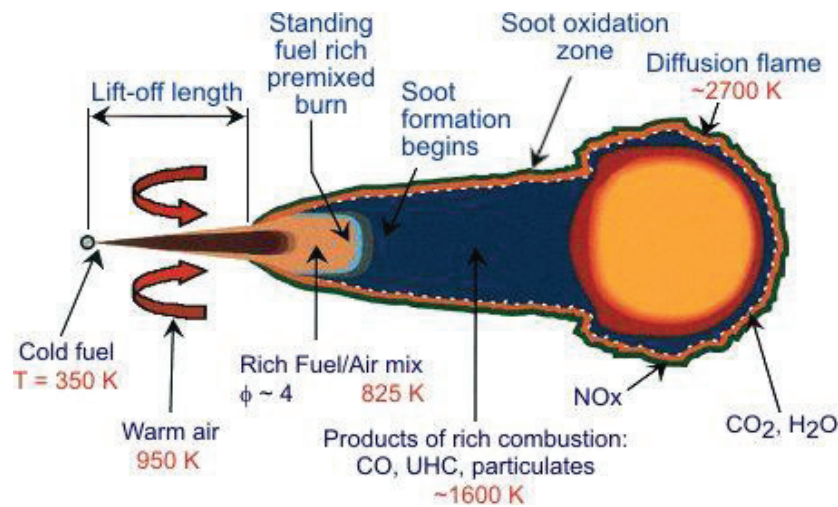


Fig. 1.7 Schematic diagram of diffusion flame and production of NO_x and soot.

The temperature of the spray internal range reached about 1600K-1700K during the stage of premixed combustion. The air-fuel mixture inside the spray is continuously processed at this stage. Finally, available O₂ in this area is consumed by the oxidation of the fuel. After that, the part of the combustion products diffuses from inside to outside of the spray. This type of combustion happens in a very thin reaction region outside the spray, which is called as diffusion flame, as shown in Fig. 1.7. Therefore, this combustion is known as diffusion combustion, as shown in phases 2 and 3 in Fig. 1.6. This stage is limited by entrained air and the mixing of the combustion products, where the reaction is slower than the premixed combustion stage. In stage 2, the fuel droplets and the entrained hot air are mixed and evaporated. The heat transferred from the oxidation reaction and the diffusion flame maintains the temperature of the internal area at a value up to 1600-1700 K [62]. It is well known that the combination of low oxygen levels and high temperature are perfect conditions for soot formation, which

results in a large mass of soot inside the flame. Since the high temperature of the spray outside region, the soot that enters the diffusion flame is burned. It is possible to produce a significant amount of NO_x at the diffusion flame's outer edge because of the availability of oxygen there.

Again, the diffusion combustion can be divided into two-stage as shown in Fig. 1.6. During stage 2, The remaining un-combustion part of the oxidized fuel and most of the soot enter the final oxidation stage. However, the sufficient decrease of oxygen and the decrease in air temperature throughout the expansion stroke, which make the chemical reactions to slow down. A sufficient decrease of soot is only possible if the ambient temperatures larger than 1600 K. Many researchers spent their lot of time and effort researching the combustion characteristics of diesel engines in order to reduce soot and NO_x emissions.

Cung et al. [63] examined the effect of micro-hole nozzle on diesel spray and combustion characteristics; the results demonstrated that when nozzle diameter was reduced to 50 micrometer or less, liquid length was condensed to a "minimum" level. Additionally, the smaller nozzle diameter improved fuel jet atomization, air entrainment and the elevated flame's position shifted toward the nozzle tip. Smaller nozzle hole diameters greatly reduced the local equivalency ratio along the spray centerline, but at the jet border, where the lifted flames steadied, the air-fuel ratio unchanged (lean).

Duraisamy et al. [64] analyzed the dual fuel Premixed Charge Compression Ignition (RCCI) combustion in an automotive diesel engine. The results showed that increasing mass fraction of methanol prolonged the ignition delay and reduced the in-cylinder pressure. At a premixed mass fraction of 80%, the maximum brake thermal efficiency of both Methanol/Diesel and Methanol/PODE (Polyoxymethylene Dimethyl Ethers) is about 31% which is 3.5% higher than conventional diesel combustion. Brake-specific oxides of nitrogen and soot emissions are significantly reduced for both dual fuel RCCI combustion with increased methanol mass fraction. However, the emissions of brake-specific hydrocarbons and carbon monoxide are slightly increased.

Hasegawa et al. [65] investigated the Homogeneous Charge Compression Ignition (HCCI) combustion in direct injection Diesel Engine. The Common Rail injection system was employed for the split injection strategy. The first injection was

used as the initial injection for the fuel expansion, as well as to advance the fuel change to lower hydrocarbons (low-temperature reactions), while the second injection was employed as an ignition trigger for all the fuel. The results demonstrated that the shadowgraph method did not detect luminous flame. The shadowgraph images revealed that the fluctuation caused by the low-temperature reaction. In addition, numerous ignition points appeared in the combustion chamber. This combustion produced low NO_x and smoke levels in both the first and second injections.

Kato et al. Unexpected End of Formula [66] investigated the spray characteristics and combustion improvement of DI diesel engines with high-pressure (250MPa) fuel injection. The test noticed that under suitable injection timing for low NO_x emission, black smoke and particulate emissions decreased significantly. A more than eighty percentage reduction in particulate emission was achieved at the same NO_x as with a traditional jerk pump, according to emission examination data under 220 MPa injection pressure.

In Fig. 1.8, Kosaka et al. [67] offer a precise model of the soot production as well as oxidation process. It was investigated that formaldehyde and a few other intermediate species occur downstream of the rich air-fuel mixture as a sign of low-temperature burning. Young soot has developed in the inner cloud at the spray tip following the premixed combustion. A significant amount of soot mass occurs in the inner partial oxidation area during the diffusive combustion, and most of them will be burned when transported to the outer region. The head vortex motion, in particular, is what encourages soot oxidation

Minato et al. [68] investigated the premixed of diesel combustion with ultra-high-pressure injection. They observed that reducing the amount of mixing time required for lean mixture creation by enhancing turbulent mixing rate by combining micro-hole nozzles with ultra-high-pressure injection is very effective. Momentum exchange and quick vaporization also lead to quick air-fuel mixing and a decrease in wall wetting, where CO and HC emissions were also decreased.

Pierpont et al. [69] investigated the effects of the nozzle geometry on direct injection diesel engine performance and injection pressure. They discovered that findings with a 75 percent load revealed the anticipated flattening and panic of the trade-off curve with greater injection pressure. However, to keep the same NO_x level when

moving from 90 to 160 MPa, injection timing had to be delayed, which led to a 1% to 2% rise in BSFC (Brake Specific Fuel Consumption).

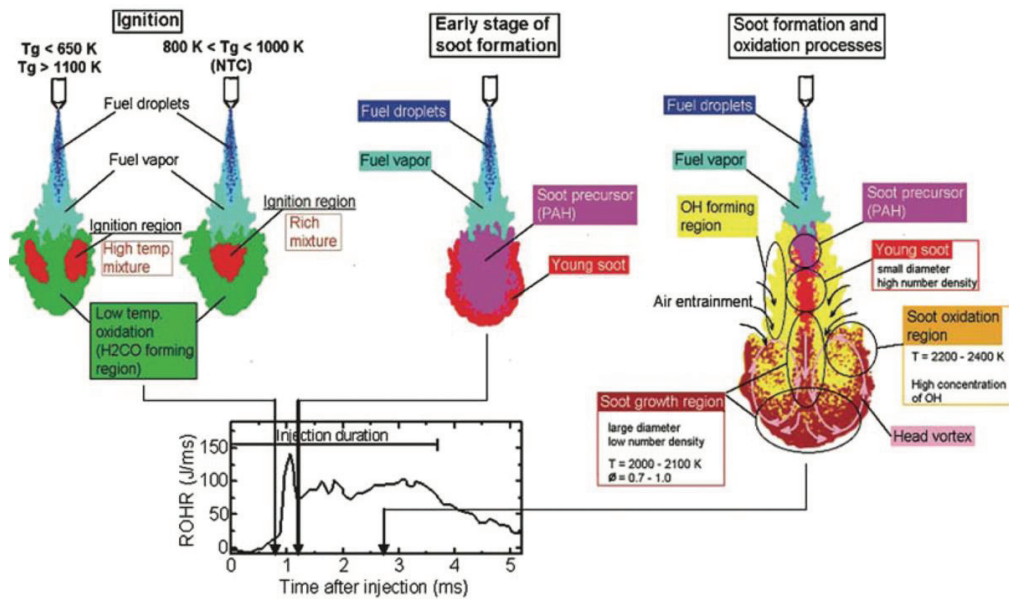


Fig. 1.8 Conceptual model of ignition, soot spray flame formation, and oxidation processes in a diesel spray flame.

Shundoh et al. [70] examined how high-pressure fuel injection affects injection settings and swirl on diesel combustion. The results show that the combination of relatively smaller nozzle hole diameter, more than 150 MPa injection pressure, and quiescent combustion technique offers better performance and emission.

1.4.3 Multiple Injection

Multiple injection techniques have been investigated and utilised extensively in traditional diesel engines in recent decades owing to their advantages such as lower emissions and improved engine efficiency [71-76]. The formation of diesel spray mixtures is crucial, as it directly determines the efficiency of the engine and exhaust formation process. Currently, fuel quantity distribution and injection timing can be monitored in a versatile manner owing to the electronically controlled high-pressure common-rail technique. The continuous development of common-rail injection technology has highlighted the importance of appropriate fuel spray control. Common-rail injection technology provides greater flexibility in multiple injections, where the dwell time and number of injections can be controlled [77]. The illustration of multiple

injection events is shown in Fig. 1.9, while the multiple injection pulses could be adjusted varying with the various real engine needs.

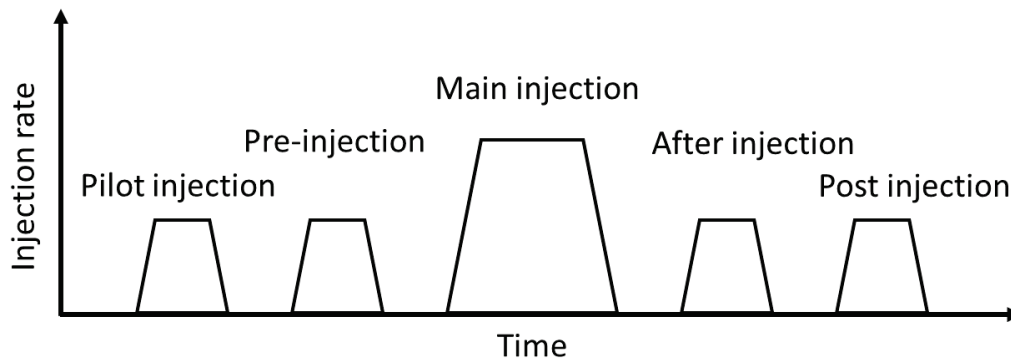


Fig. 1.9 the multiple injection.

A conventional injection event consists of a single and continuous fuel supply to the combustion chamber. With a multiple injection, the fuel is divided into various closed quantities, which can be equal in mass (split approach) or vary in mass (early-pilot-post-late approaches). The split injections often divide the target mass uniformly among different pulses, which is the fundamental difference between the later approaches. In contrast, multiple injections with a main, each pulse of a various quantity, trying to match the same injected target mass as a single injection event, to avoid increasing fuel consumption. The distance between the pulses is generally referred to as the dwell time (DT). It is important to point out that the actual dwell time is the separation between mass flow rate pulses and not the signal command, to consider the hydraulic delay of the start and end of injection [78]. The number of pulses is limited between the capacity of the injection system and combustion duration. However, with the development of diesel technology, new injection systems can precisely inject up to eight different times per cycle [79]. More pulses offer more flexibility and air-fuel mixing and control over the heat release, which if properly turned, can allow for better engine performance [80].

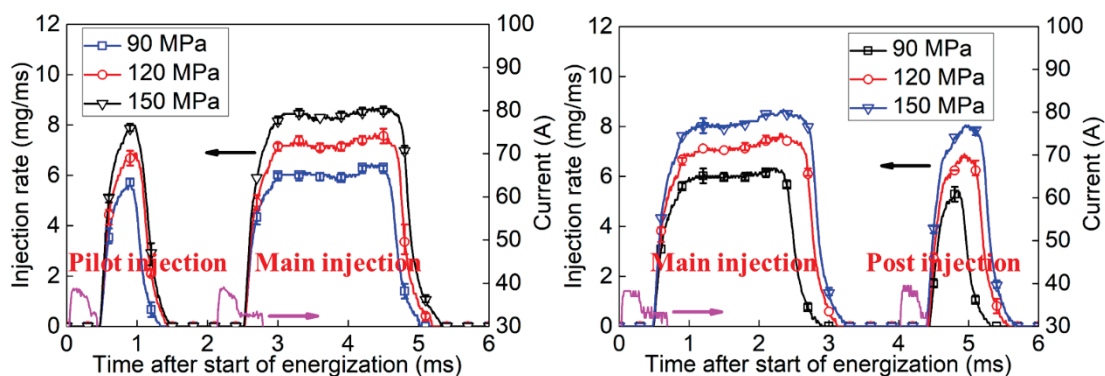


Fig. 1.10 Injection rate for the pilot-main and main-post strategy.

Wu et al. [81] investigated the characteristics of split injection by using the pilot-main as well as main-post injection strategy. The injection rate is presented in Fig. 1.10. The development of spray tip and tail penetration, as well as the spray angles were the main discussion of this study.

There are several ways to reduce noise and NO_x emissions before the main injection, including the use of small pilot injections. To increase the mixing between areas depleted in oxygen by combustion with areas that still have plenty of oxygen, small injection quantities can be added after the main injection. In contrast, very late post-injections no longer contribute to torque but instead heat up the exhaust, which could be useful for heating up or regenerating catalysts. Finally, separating the main injection into two or more events slows combustion and reduces combustion noise - at the risk of increased soot formation. To investigate actual physical phenomena associated with multiple injections, most researchers refer to the procedure of injection pulse interaction. Multiple injections have been performed to reduce combustion noise, soot oxidation, and reduce NO_x emissions. Bruneaux and Maligne [82] and Pickett et al. [83,84] experimentally investigated the characteristics of non-reacting split injections. Both Bruneaux and Maligne [82] and Skeen et al. [84] demonstrated that the second injection vapor phase reaches a 'slipstream', thereby enabling it to penetrate more quickly than the first injection. The combustion of split injection strategies is a result of interactions between the first and second injections. To enhance the diesel engine efficiency, combustion, and reduce soot emission processes, a pre-injection system is needed [85]. Harfatmanesh et al. [86] and De Kim et al. [87] reported that the second injection of fuel spray into a burning hot gas resulted in double-injection high soot emissions and fuel-rich combustions. However, the use of the double injection method with shorter injection duration decreases soot emissions [88]. Furthermore, when the dwell time between two injections is short and the second fuel mass is large, the tip of the second spray will be in contact with the first spray [89]. Bruneaux discovered that the interaction between two injection pulses is more robust when a single-hole injector is used for a shorter dwell time; consequently, the mixing rate at the second spray head will be higher [82].

1.4.4 Optical Diagnostic Techniques for Spray and Combustion

Optical diagnostic techniques are frequently used to investigate the nature of diesel sprays and combustion, as shown in Table 1.1. Some optical diagnostic approaches will be briefly discussed in this section.

(1) Mie Scattering

Mie scattering is used to get the information of liquid fuel distribution. The scattering of particles and light is the principle of this technique. The scattering intensity of this kind of scattering is proportional to the second power of the frequency, and the scattering is stronger in the forward direction of the light than in the backward direction [90]. Nevertheless, compared to other newly established optical diagnostic procedures, the results of the droplet diameter and concentration analysis from Mie scattering brightness are not very precise [91]. The geometric optics limit for large particles is reached by Mie scattering, which has no maximum size limit [91].

(2) Schlieren and Shadowgraph

Schlieren and Shadowgraph are very common optical observation method in experiments. The basic principle of these method is to use the refractive index gradient of light in the measured flow field to be proportional to the airflow density of the flow field [93]. Therefore, schlieren and shadowgraph have an advantage over the Mie scattering / DBI approach in that they can detect both vapor and liquid phase. However, the vapor concentration of the evaporating spray could not be obtained by them. Schlieren and Shadowgraph are mostly used to analyze the shock wave and spray structure. Fig. 1.11 shows the diagram of a Z-type schlieren experimental setup.

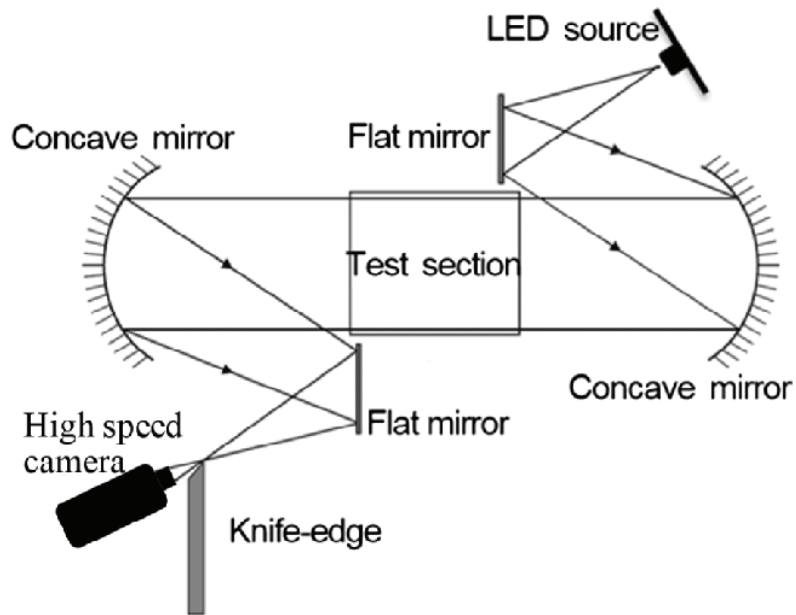


Fig. 1.11 Schematic diagram of schlieren.

(3) Laser Rayleigh Scattering (LRS)

Since the scattered light brightness is proportional to the density distribution of gas molecules, LRS is used to assess vapor phase concentration.

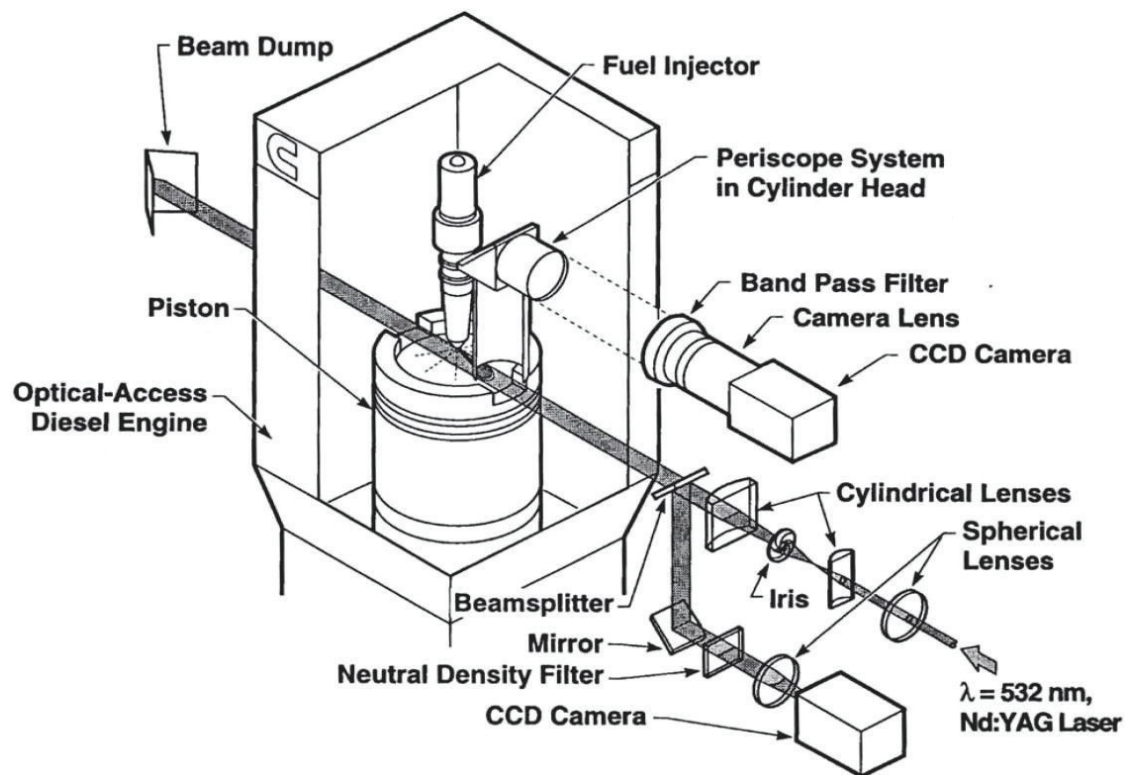


Fig. 1.12 Schematic of the optical setup for LRS measurements.

Additionally, due to the cross section of larger scattering, LRS can be used to detect vapor concentration when the gas density is low. However, using LRS technique, it is challenging to remove noise that results from Mie scattering. The energy of Mie scattering is 10 to 20 orders of magnitude higher than that of Rayleigh scattering, hence it makes no difference if Mie scattering occurs when using the LRS technique. Consequently, the LRS method must be used in a virtually particle-free environment. Espey et al. [94] applied planar LRS technique effectively to obtain the quantitative measurement of vapor concentration. Fig. 1.12 shows the experimental layout of LRS measurement.

(4) Spontaneous Raman Scattering (SRS)

SRS is a technique for analyzing the concentration of gaseous species and estimating the air/fuel ratio.

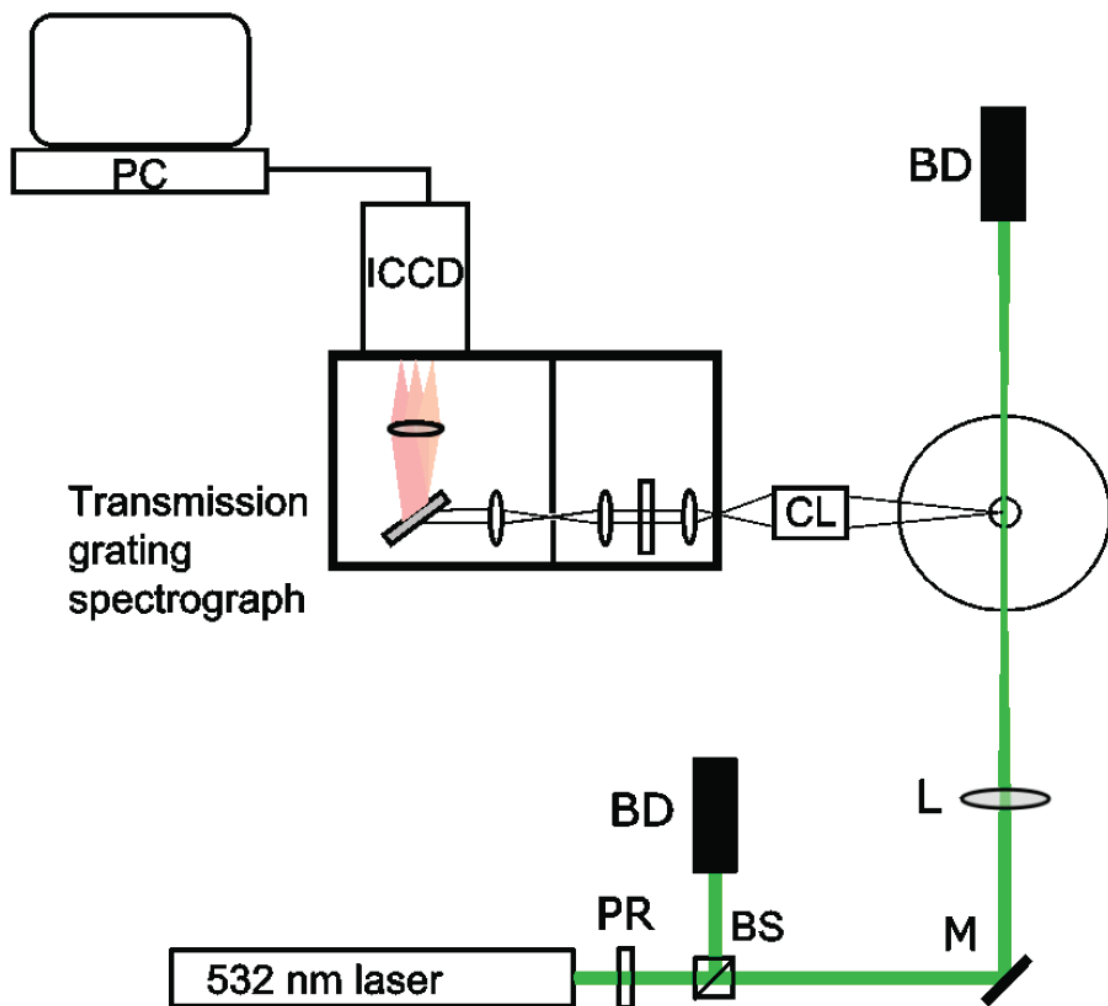


Fig. 1.13 Schematic of the Raman set up.

According to research by Johnston [95] into the pre-combustion fuel/air dispersion in a stratification charge engine, fuel injection causes a significant change in the air/fuel ratio distribution. By using SRS, Sawersyn et al. [96] studied the spatial distributions of various species. The gaseous species molar fraction was investigated by Miles and Hinze [97]. SRS was also utilized by Raising [98] to detect the thermodynamic instability in rapid mixing and combustion. Fig. 1.13 illustrates the Raman scattering experimental setup [98].

(5) Laser Induced Fluorescence (LIF)

Including sprays and combustion systems in fluid mechanics, LIF is a highly sensitive laser imaging method for measuring species concentration, mixture formation, and temperature distributions [99,100]. Its utilization of the electronic absorption and emission process theory of a particular species expelled by an incident laser source; a particular species of interest's mole fraction and fluorescent light's brightness are associated [101]. Even though this approach provides more intense fluorescent lighting, it is impressionable to the ambient pressure and temperature. Fig. 1.14 show the schematic diagram of LIF setup.

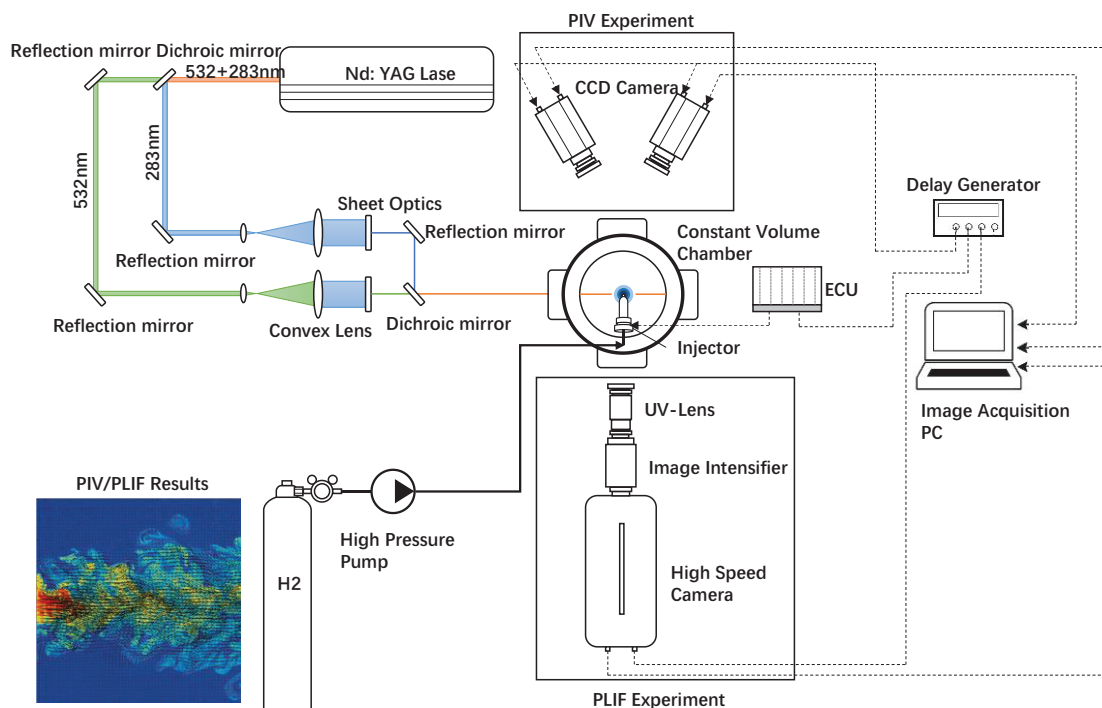


Fig. 1.14 Schematic diagram of PIV/LIF.

(6) Laser Induced Exciplex Fluorescence (LIEF)

LIEF technique was established [102-104] for the quantitative measurement of vapor and liquid phases of the evaporating spray simultaneously. The benefit of the LIF-technique is the unique separation of 2-D measurements of the vapor and liquid phases in spray and combustion processes, which attracted considerable attention from other researchers [105]. Using LIEF, Senda et al. [106-108] investigated the impinging spray's vapor concentration and offered some basic concepts for the evolution of impinging spray. Bruneaux [109] examined the structures of vapor and liquid phase concentrations using LIEF. Additionally, Bruneaux [110] investigated the mixture formation in high-pressure diesel jets using LIEF, Fig. 1.15 depicts the LIEF experimental setup. The results reveal that increasing the injection pressure causes a constant air entrainment rate, and that the nozzle hole diameter has a substantial effect on the global mixing rate. Bruneaux [111] investigated the combustion behaviors of wall-impingement and free diesel jets using LIEF. Comparing LIEF to LIF, the benefit is that imaging of the vapor phase is possible without interference from the liquid phase [112]. However, due to the limitation of quenching by oxygen in the LIEF technique, ambient conditions and careful consideration of the fuel type is essential.

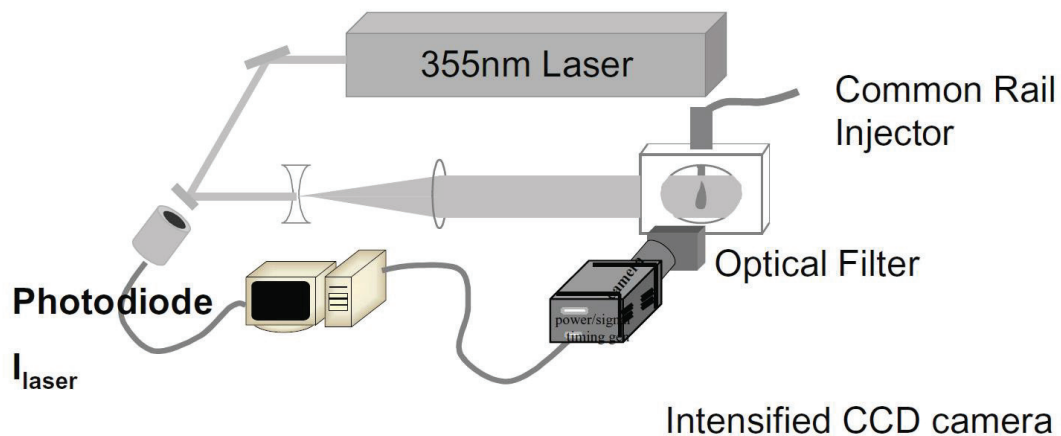


Fig. 1.15 Experimental setup for LIEF visualizations.

(7) Laser Absorption Scattering (LAS)

LAS is a Nobel laser diagnostic technique that uses for the UV and Vis light to measure the concentration of liquid as well as vapor phases in a mixture. Chraplyvy [113] proposed this technique first, using $3.39 \mu\text{m}$ and $0.6328 \mu\text{m}$ to determine liquid and vapor scattering, separately. Suzuki et al. [114] conducted diesel spray evaporation experiments and concluded that this new technique could generate 3D measurements

of liquid droplet density and fuel vapor phase. Initially, α -Methylnaphthalene was used as test fuel. Modifications were made as time passed. The details of the LAS principle are covered in Chapter 2.

Table1.1 Summary of optical techniques for in-cylinder measurement

Technique	Applications	Advantages	Limitations
Mie Scattering	Liquid fuel Distribution	Simple setup	Sensitive to large droplets
Schlieren and Shadowgraph	Observation of overall spray	Simple setup	Sensitive to both liquid and vapor phases
LRS	Density measurement Vapor concentration	Strong signal Simple setup 2-D imaging	Interference from Mie and spurious Scattering limited to gaseous fuel
SRS	A/F ratio Residual gas Fraction Multi-species detection	Multi-point detection Most accurate A/F readings Unaffected by windows fouling	Weak signal
LIF	Fuel concentration	Strong red shifted Signal 2-D image of fuel	Quenching at high pressures difficult to calibrate
FARLIF	A/F ratio	Direct A/F measurements 2-D imaging	Careful calibration required high pressure operation
LIEF	Fuel vaporization & atomization	2-D imaging Simultaneous detection of vapor and liquid	Quenching by oxygen
LAS	Fuel atomization and vaporization	Quantitative concentration measurements Droplet size information	Poor spatial resolution

CHAPTER 2 EXPERIMENTAL APPERATUS AND MEASURING METHODS

2.1 HIGH-PRESSURE AND HIGH-TEMPERATURE CONSTANT VOLUME CHAMBER

To make sure that the system reaches the expected experimental conditions, the constant volume chamber can provide a steady ambient temperature and pressure for the experiment. Fig. 2.1 illustrates the structure diagram of a constant volume chamber. The chamber has a cylindrical shape, and the cylinder - shaped constant volume chamber is closer to the structure of the engine cylinder, which theoretically brings the airflow movement during the diesel injection process more in line with reality. Four quartz windows are uniformly distributed around the main body and are secured by the window cover. The diameter of the observation window is approximately 100 mm. Light can pass directly through any two opposite glass windows to achieve the spray visualization. Furthermore, light can enter the chamber through the side of the observation window and be captured by a CCD (charge-coupled device) or HSV (high-speed video) camera. The heater is in the center of the constant volume chamber and can reach temperatures of 1000 K and pressures of 6 MPa. Additionally, gas inlet/outlet, heater terminals, and thermocouple cables can be found between any two adjacent windows.

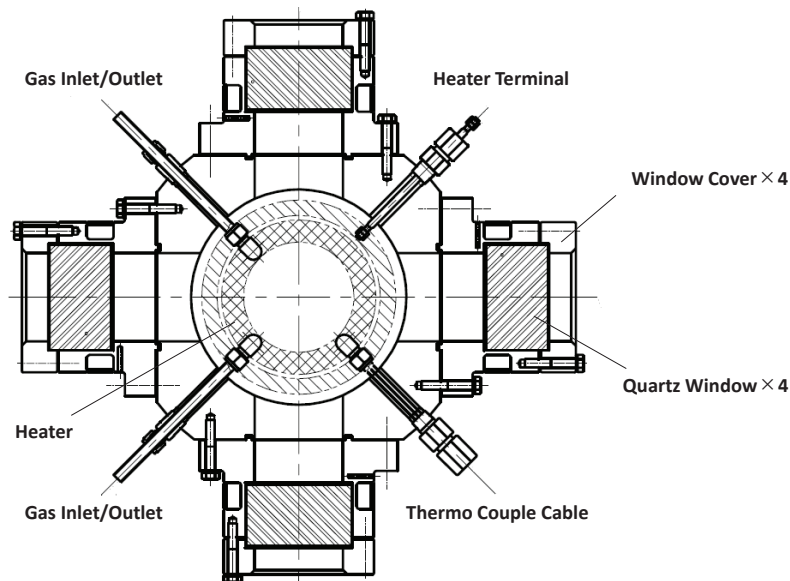


Fig. 2.1 Schematic of the chamber body (top view).

2.2 FUEL INJECTION SYSTEM

The fuel injection system is divided into two parts: the fuel supply system and the injector. IRS (Injector Refresh Service) Corporation manufactured the high-pressure fuel supply system used in the experiment, which was customized and could provide a rail pressure of up to 200MPa. The system has two kinds of fuel circuits, one for diesel and the other for tracer fuel, which is used specifically in the HS-LAS/LAS experiment.

Table 2.1 Specification of The Injector

Injector type [-]	Piezo type
Number of holes [-]	7
Diameter of hole exit: d_{out} [mm]	0.123
Hole length: l [mm]	0.8
K-factor [-]	2.7
Spray included angle: θ [deg.]	155

The injectors, as shown in Fig. 2.2, are specially designed for the Cross-ministerial Strategic Innovation Promotion (SIP) Program and provided by the Denso Corporation. In the nozzle tip of the multi-hole injector, there are seven holes. The injector was Piezo type, as shown in Table.2.1, with a hole exiting diameter of 0.123 mm and a hole length of 0.8 mm. It could be mentioned that the holes type is merging with a K-factor of 2.7. Eq.2.1 gives the definition of the K-factor. However, an angle of 77.5° exists between the injector's hole as well as injector axes. To put it another way, the spray included angle is 155° .

$$K = \frac{100(d_{in}-d_{out})}{l} \quad (2.1)$$

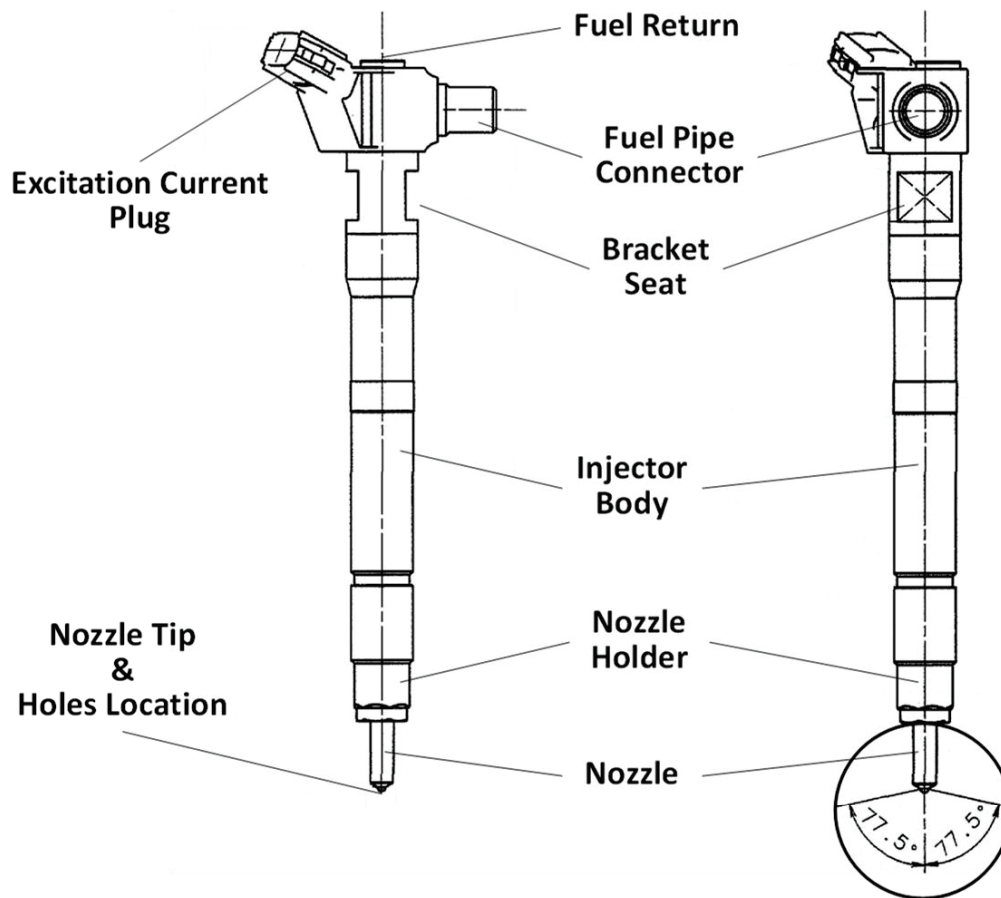


Fig. 2.2 Injectors used in the experiment.

2.3 INJECTION RATE MEASUREMENT SYSTEM

The fuel injection measurement system is FJ-6000 Series made by Ono Sokki Co.; Ltd. Fig. 2.3 depicts the system's composition. It has a high accuracy in measuring fuel injection quantity (within 0.5 percent of reading) and a large measuring range (0-300 mm³/str)[115]. The measurement system is based on Zeuch's method [116], which is illustrated in Fig. 2.4.

The detection cavity was full of test fuel before the fuel injection started. Meanwhile, the cavity volume V as well as the pressure P inside the cavity remain constant. When fuel with a volume of V is injected inside the cavity, the pressure P rises due to the constant volume, as shown in the Fig. 2.4. Eq. (2.2) shows the relationship between P and V .

$$\Delta P = k \frac{\Delta V}{V} \tag{2.2}$$

where k represents the fuel's bulk modulus.

$$\frac{dV}{dt} = \frac{V}{k} \frac{dP}{dt} \quad (2.3)$$

By taking the derivation of Eq. (2.2) with respect to time, the direct relationship between injection rate $\frac{dV}{dt}$ as well as pressure variation rate $\frac{dP}{dt}$ can be obtained as shown in Eq. (2.3). This means the injection rate can be measured by employing a pressure sensor with high pressure frequency and accuracy.

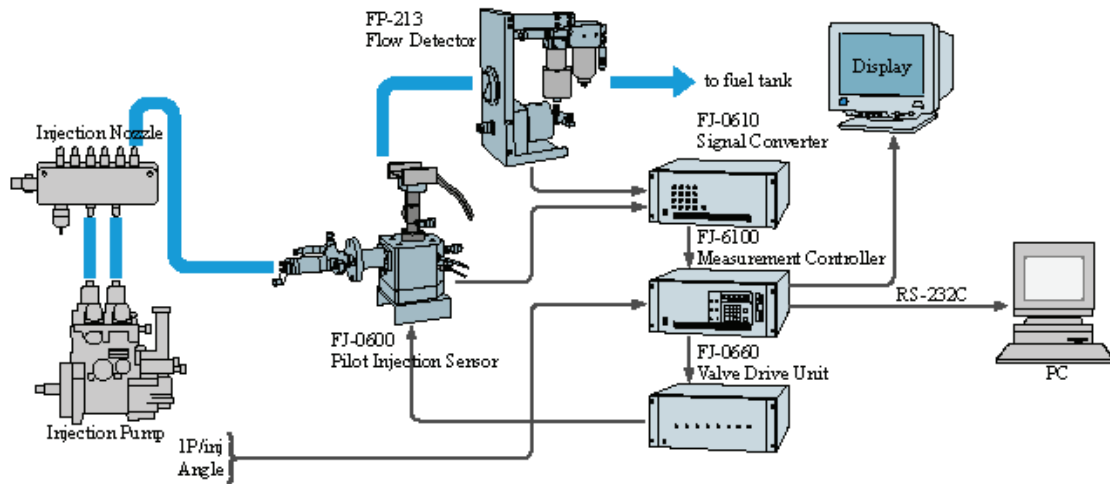


Fig. 2.3 Composition of injection rate measurement system.

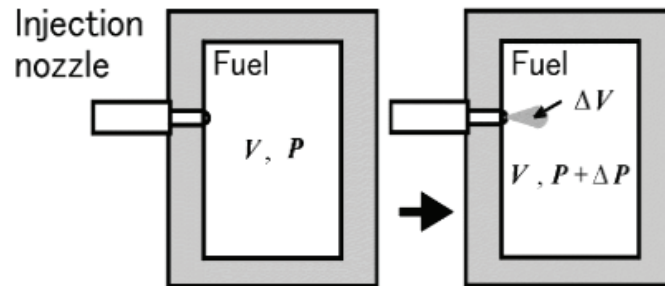


Fig. 2.4 Measurement principle of Zeuch method.

2.4 TRACER LAS TECHNIQUE FOR MIXTURE CONCENTRATION MEASUREMENT

2.4.1 Principle of Tracer Laser Absorption Scattering (LAS) Technique

The Laser Absorption Scattering (LAS) technique is used to visualize the vapor phase and measure the mixture concentration in the evaporating experiment. In LAS technique two different wavelengths of light are used: visible light is used to detect liquid phase Optical Thickness (OT) at 532 nm scattering wavelengths and ultraviolet light (UV) is used to detect combined liquid and vapor phases OT at 266 nm absorption wavelengths[117-122].

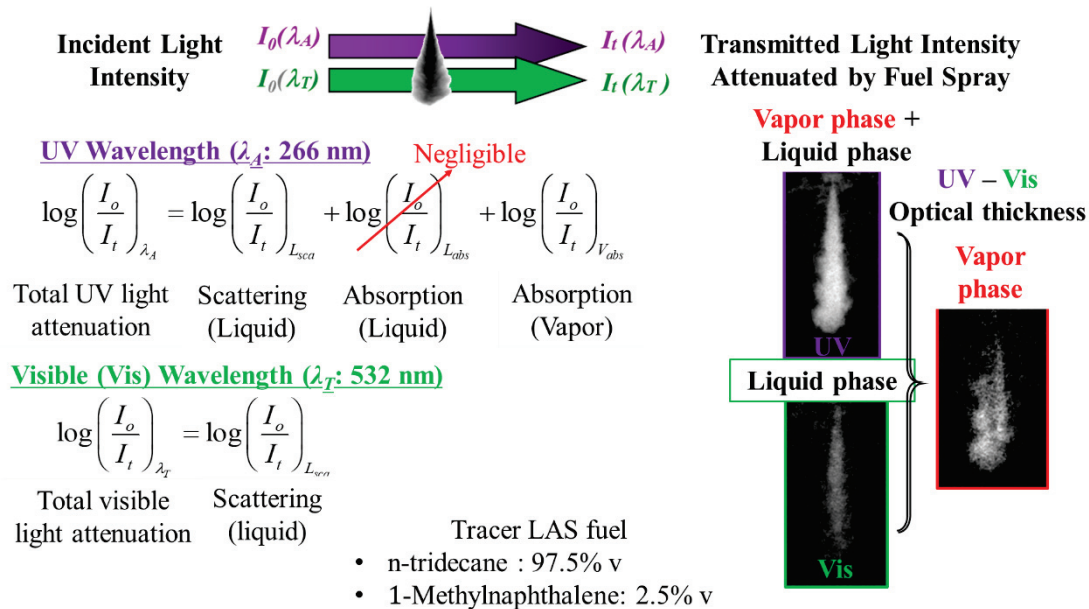


Fig. 2.5 Principle of LAS technique.

The beam of two incident light passes through the spray as shown in Fig. 2.5. The transmitted light intensities are reduced by the effect of attenuation. In the ultraviolet (UV) image, the intensity is attenuated by liquid absorption, liquid scattering, as well as vapor absorption; in the visible (Vis.) image, the extinction is only caused by droplet scattering. Thus, the vapor phase optical thickness can be found by subtracting the visible phase optical thickness from the UV phase optical thickness. The transmittance for absorption $\log(I_0/I_t)_{\lambda_A}$ and that for scattering $\log(I_0/I_t)_{\lambda_T}$ for each light wave are defined as follows:

$$\log \left(\frac{I_0}{I_t} \right)_{\lambda_A} = \log \left(\frac{I_0}{I_t} \right)_{L_{sca}} + \log \left(\frac{I_0}{I_t} \right)_{L_{abs}} + \log \left(\frac{I_0}{I_t} \right)_{V_{abs}} \quad (2.4)$$

$$\log \left(\frac{I_0}{I_t} \right)_{\lambda_T} = \log \left(\frac{I_0}{I_t} \right)_{L_{sca}} \quad (2.5)$$

where $\log(I_0/I_t)_{L_{sca}}$, $\log(I_0/I_t)_{L_{abs}}$, and $\log(I_0/I_t)_{V_{abs}}$ in Eq. (2.4) represent attenuation by liquid scattering, liquid absorption, and vapor absorption, respectively. Nevertheless, the liquid absorption term $\log(I_0/I_t)_{L_{abs}}$ in Eq. (2.4) is negligible [57]. Consequently, Eq. (2.4) can be expressed as follows:

$$\log \left(\frac{I_0}{I_t} \right)_{\lambda_A} = \log \left(\frac{I_0}{I_t} \right)_{L_{sca}} + \log \left(\frac{I_0}{I_t} \right)_{V_{abs}} \quad (2.6)$$

The terms $\log \left(\frac{I_0}{I_t} \right)_{\lambda_A}$ and $\log \left(\frac{I_0}{I_t} \right)_{L_{sca}}$ are generated from the spray and background images, respectively.

However, to estimate the spatial distribution of liquid and vapor concentration of the spray, the onion peeling method is used to the liquid and vapor phases optical thickness for the case of axisymmetric spray [123]. The radial cross section of the spray is divided into many concentric rings in the processing model. When each ring's width is extremely narrow, the concentrations within the ring can be termed homogeneous. The concentration of vapor phase fuel in each ring can be calculated through the Lambert-Beer's law by Eq. (2.7). For liquid concentration, it is presumed that liquid droplets in the spray have a homogeneous Sauter Mean Diameter (SMD). Based on droplet optical thickness and light scattering theory, the concentration of the liquid can be determined as shown in Eq. (2.8). The SMD is calculated by summing the liquid droplet optical thickness in the whole extinction image of the spray as shown in Eq. (2.9). In Fig. 2.6, the analytical procedure is simply displayed.

$$C_v = \frac{1}{\varepsilon(\lambda_A)L} \left[\text{Log} \left(\frac{I_0}{I_t} \right)_{\lambda_A} - R \text{Log} \left(\frac{I_0}{I_t} \right)_{\lambda_T} \right] \quad (2.7)$$

$$C_L = 2.303 \frac{2}{3L} \rho_f \frac{SMD}{R_k Q_{ext}} \left[\text{Log} \left(\frac{I_0}{I_t} \right)_{\lambda_T} \right] \quad (2.8)$$

$$SMD = \frac{SMD0.63R_kQ_{ext}M_f}{\rho_f \sum \text{Log} \left(\frac{I_0}{I_t} \right)_{\lambda_T} \Delta S} \quad (2.9)$$

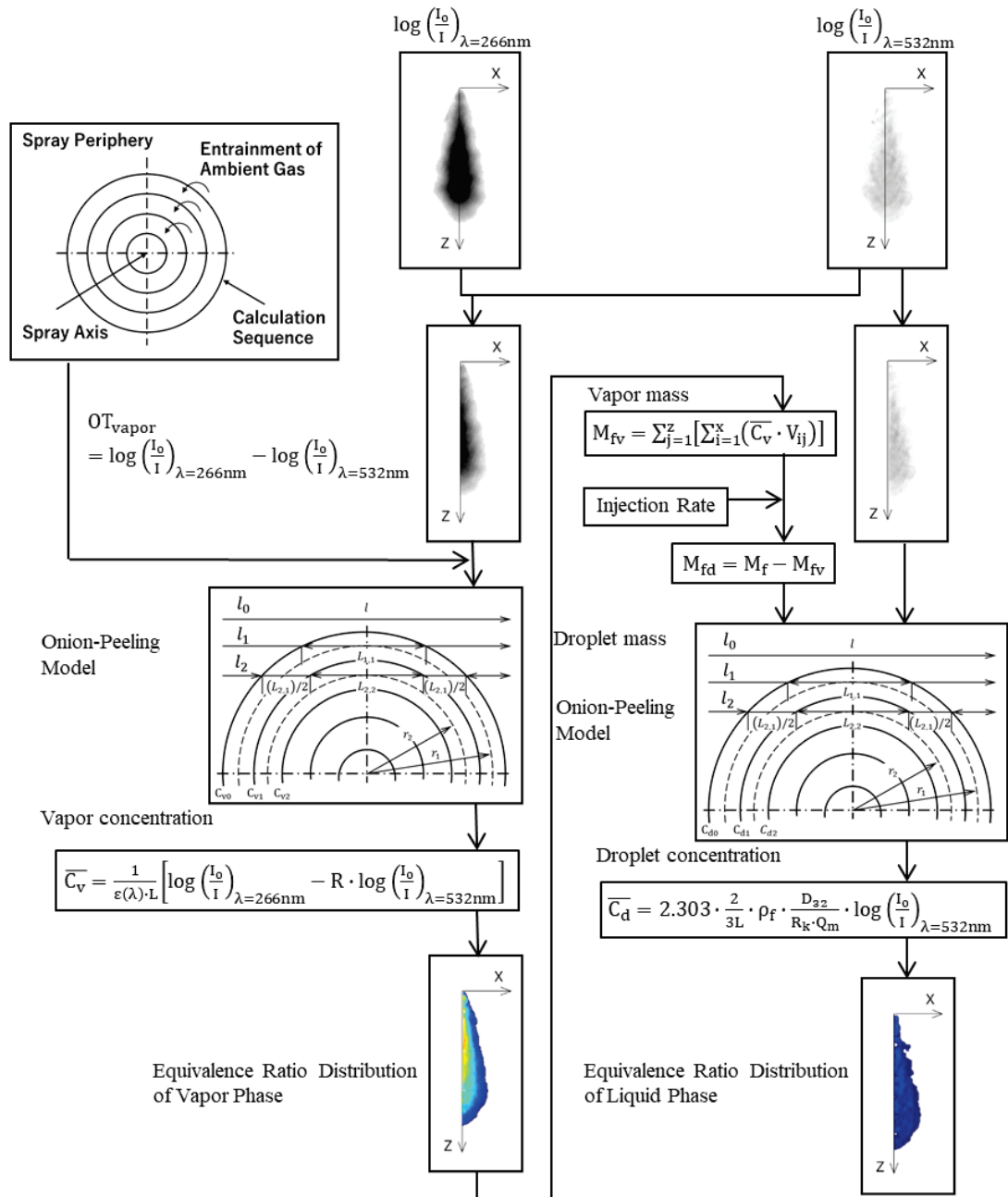


Fig. 2.6 Axisymmetric fuel spray image processing flow chart.

It is significant to note that the onion peeling method can be used again to calculate the volume-based fuel concentration, the distribution of mixture temperature, overall amount of air entrainment and equivalence ratio. A mass concentration of ambient gas entrainment is calculated via the ideal gas equation. Therefore, the average equivalence ratios of vapor and liquid phase could be estimated by applying Eq. (2.10) and (2.11), respectively.

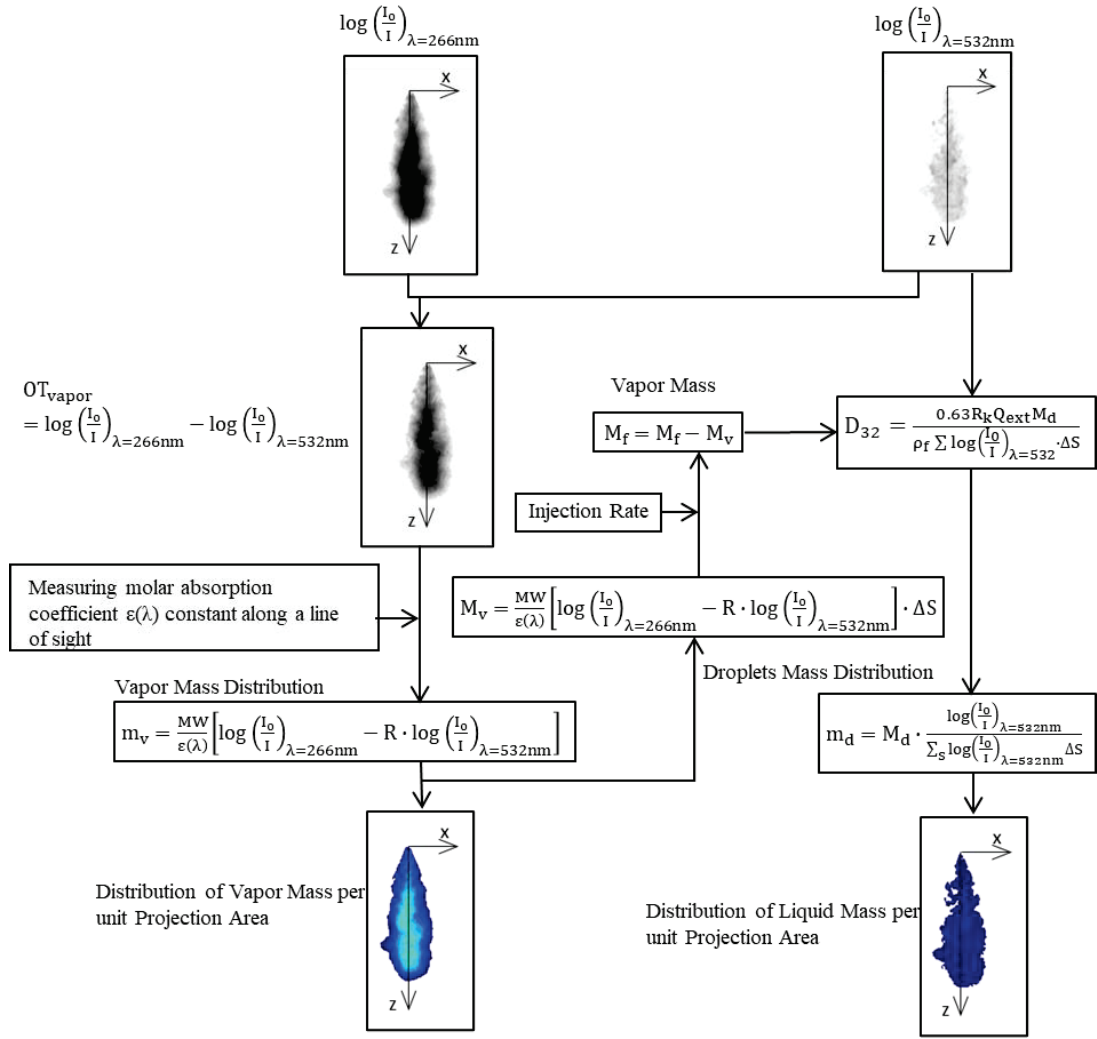


Fig. 2.7 Non-axisymmetric fuel spray image processing flow chart.

$$\phi_V = \frac{AF_{STOICH}}{AF_V} = \frac{AF_{STOICH}}{\left(\frac{c_a}{c_v}\right)} \quad (2.10)$$

$$\phi_L = \frac{AF_{STOICH}}{AF_L} = \frac{AF_{STOICH}}{\left(1 - \frac{c_L}{\rho_f}\right) \left(\frac{c_a}{c_L}\right)} \quad (2.11)$$

In fact, in a Diesel engine, the spray is always non-axisymmetric. When the LAS method is used to examine a non-axisymmetric spray pattern, the onion-peeling method is not available. Therefore, [124] modified the LAS method to analyze the non-axisymmetric spray concentrations. Figure 2.7 depicts the diagram for the non-axisymmetric analyzing process.

2.4.2 Optical Arrangement for LAS System

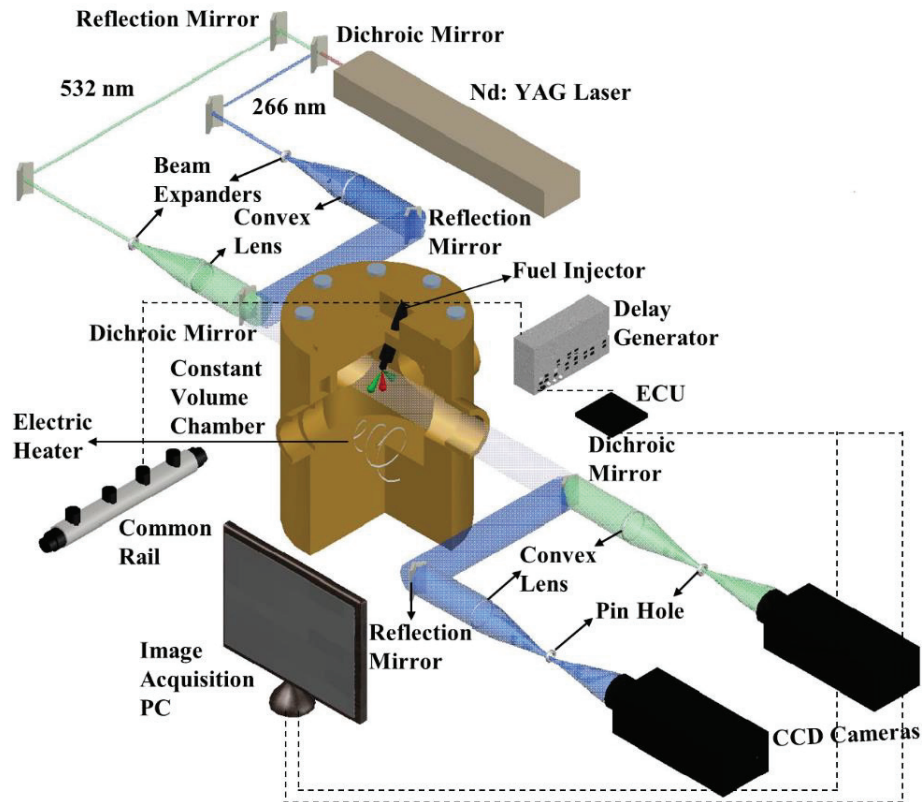


Fig. 2.8 Laser Absorption Scattering (LAS) schemes with optical system and constant volume chamber.

Fig. 2.8 shows the experimental setup for the LAS technique. A constant volume spray chamber (CVSC) including four optically visible windows was used to conduct the experiment, where two 100-mm-diameter quartz windows were allocated for visualisation. The injector was placed at the top of the chamber with spray including angle. Moreover, a common-rail system was used to achieve the required injection pressure which was operated by the high-pressure pump. Since the experiment involved spray evaporation and combustion, the insulator was glued on the inside chamber walls. Further, the electric heater was positioned in the middle of the lower part of the spray chamber. The required ambient temperature was correspondingly controlled through the 20A heating system. For the optical system, a pulsed Nd: YAG (LOTIS TII LS-2137N) laser and two charge-coupe device (CCD) cameras (ANDOR iKon-M Series) were used. The Nd: YAG laser generated an ultraviolet (UV) beam of wavelength 266 nm and a visible (Vis) beam of wavelength 512 nm. Initially, a dichroic mirror separated the two laser beams, which were then extended by two beam extenders, similar to the visible windows of the spray chamber. Subsequently, the two laser beams merged and

entered the spray through the chamber. Finally, two attenuated waves were separated by a dichroic mirror and then captured by the two CCD cameras. To reduce noise during image processing, a 500 ms interval was set between the background image and the spray image for every injection case. The laser and cameras were triggered using two separate delay generators: LabSmith LC880 and Stanford Research Systems Model DG645.

2.4.3 Tracer LAS Fuel Selection

The LAS technique cannot be utilized with diesel fuel because it has a very low UV light absorption value [125-127]. Therefore, the selected fuel must meet the following requirements:

1. Comparable physical characteristics to Diesel fuel.
2. UV light is well absorbed, whereas visible light is not.
3. Lambert-beer's law is satisfied by UV absorption, and molar absorptivity is less temperature dependent.

Japanese Industrial Standard No. 2 (JIS#2) diesel fuel and candidate test fuels' physical characteristics are shown in Table 2.2. The candidate fuels are chosen in accordance with requirement 1.

The fuel n-Pentadecane appears to be the most appropriate for replacement of diesel fuel. Nevertheless, under the high-pressure conditions, for example diesel injection pressure of a diesel engine, this fuel has a lower freezing point [128,129]. Also, n-Tetradecane, and n-Hexadecane both freeze at room temperature. Therefore, these three fuels are inappropriate for the test fuel.

When n-Tridecane and 1-Methylnaphthalene's physical characteristics are compared, the density of n-Tridecane is comparable to that of diesel fuel. So, as a temporary test fuel, n-Tridecane was selected. As illustrated in Fig. 2.9, n-Tridecane meets requirement 2 by absorbing UV light but not Visible light. 1-Methylnaphthalene and 1,3-Dimethylphthalene exhibit promising UV light absorbance, whereas n-Tridecane absorbs very little UV light. The compatibility of n-Tridecane and 1-MN is superior, and their vapor-pressure curve functions with temperature are similar [130]. Therefore, 1 - MN is acceptable for making the tracer fuel added to n-Tridecane. The tracer LAS fuel in this study contains of 2.5 % 1-MN and 97.5% n-Tridecane by the volume basis.

Table 2.2 and Fig. 2.9 illustrate the calculated physical parameters and measured absorbance spectrum of the tracer fuel based on this. The following chapter will provide an explanation of requirement 3.

Table 2.2 Physical Properties of Candidate Fuels

Substance	Formula	Boling point [⁰ C]	Density [kg/m ³]	Kinetic viscosity [mm ² /s]
1-Methyl-naphthalene	C ₁₁ H ₁₀	244.7	1016	2.58
1,3-Dimethyl naphthalene	C ₁₂ H ₁₂	262.5	1018	3.95
n-Tridecane	C ₁₃ H ₂₈	235.0	756	2.47
n-Tetradecane	C ₁₄ H ₃₀	253.7	760	3.04
n-Pentadecane	C ₁₅ H ₃₂	270.6	770	3.73
n-Hexadecane [cetane]	C ₁₆ H ₃₄	287.0	780	4.52
Tracer fuel [1-MN 2.5% +n-Tridecane 97.5 %]		235.8	767	2.48
Diesel JIS#2		~273	~830	~3.86

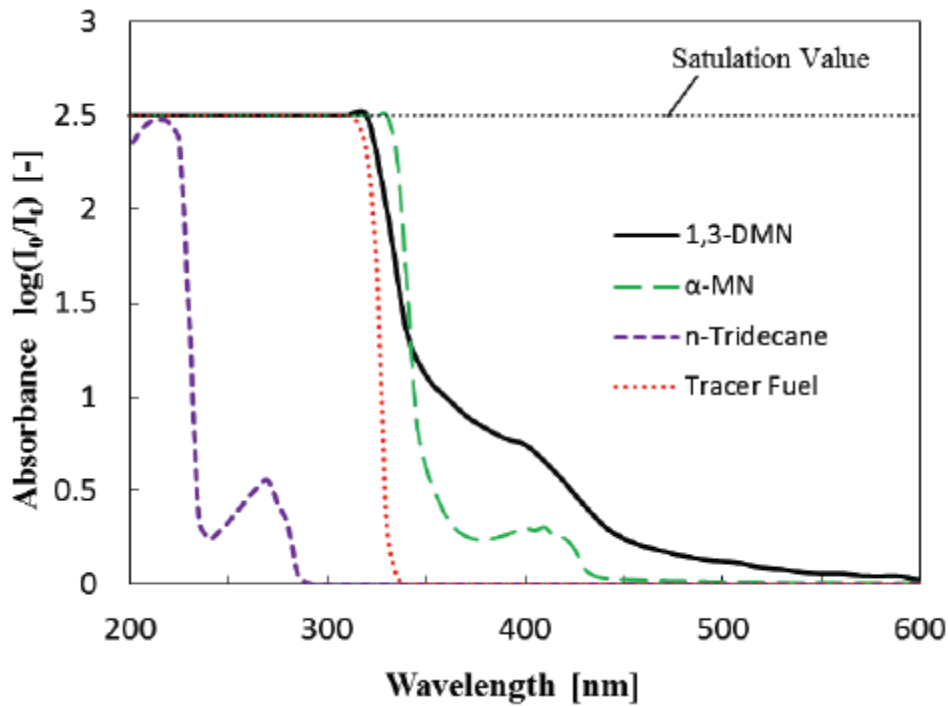


Fig. 2.9 Absorption Spectrum of Selected Fuels.

2.5 HIGH-SPEED LAS SYSTEM

2.5.1 Specification of Light Source and Image Intensifier

Table 2.3 Specification of Light Source and Image Intensifier

Device	UV	Visible
Light source	UV LED (266 nm)	CW laser (532 nm)
Power of light [W]	26.2	2
Camera	HS-video camera (B/W) Nac-Memrecam HX-3	HS-video camera color Nac-Memrecam HX-3
Frame rate fps	20000	20000
Resolution pixels	512×512	512×512
Image intensifier	UVi camera intensifier (Invisible Vision Ltd.)	

The specification of light source and image intensifier are illustrated in table 2.3. A 26.2 W UV LED and a 2 W CW laser are used as ultraviolet and visible light source. The wavelengths of ultraviolet and visible light are 266nm and 532nm, respectively. To capture the spray images, two high-speed video cameras B/W and color (NAC-

MEMRECAM HX-3) are selected. The frame rate and resolution of both cameras are 20000 frames per second (fps) and 512×512 pixels, respectively. To obtain the UV image, a UVi image intensifier (made by Invisible Vision Ltd.) is fastened in front of the B/W camera. To obtain the UV image, a UVi image intensifier (made by Invisible Vision Ltd.) is attached in front of the B/W camera.

2.5.2 Optical Arrangement for HS-LAS System

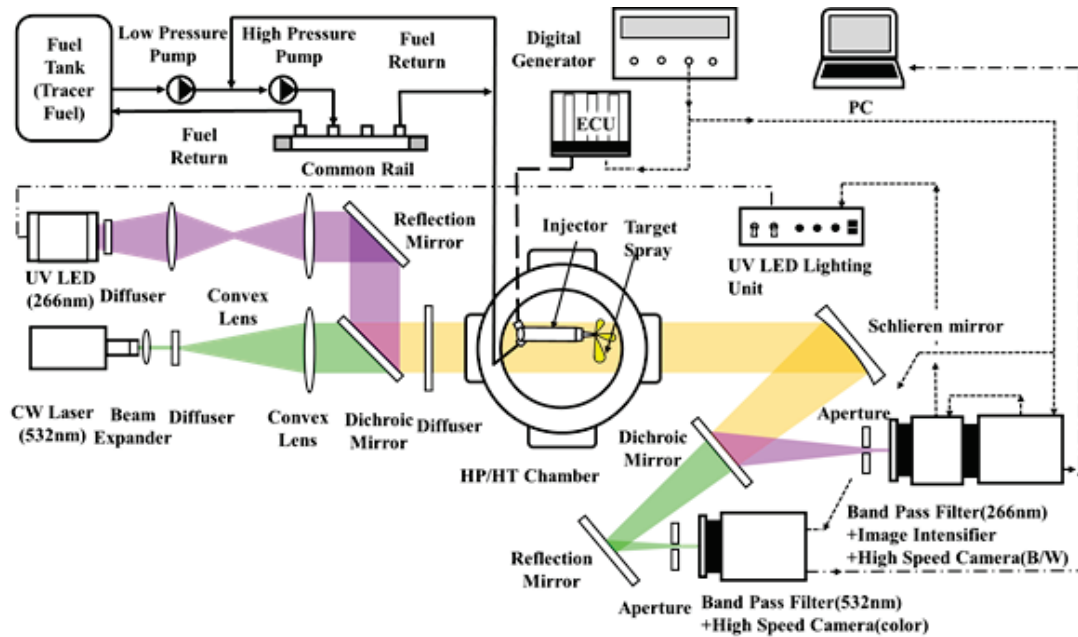
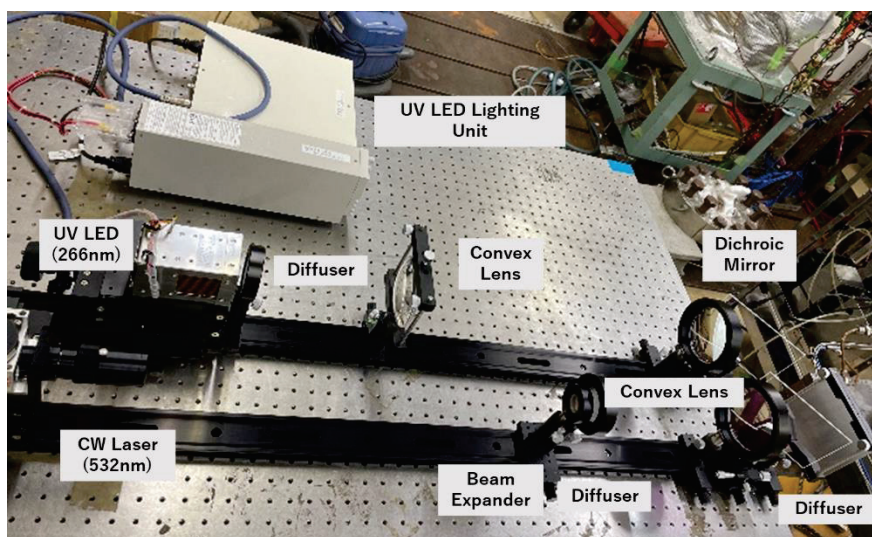
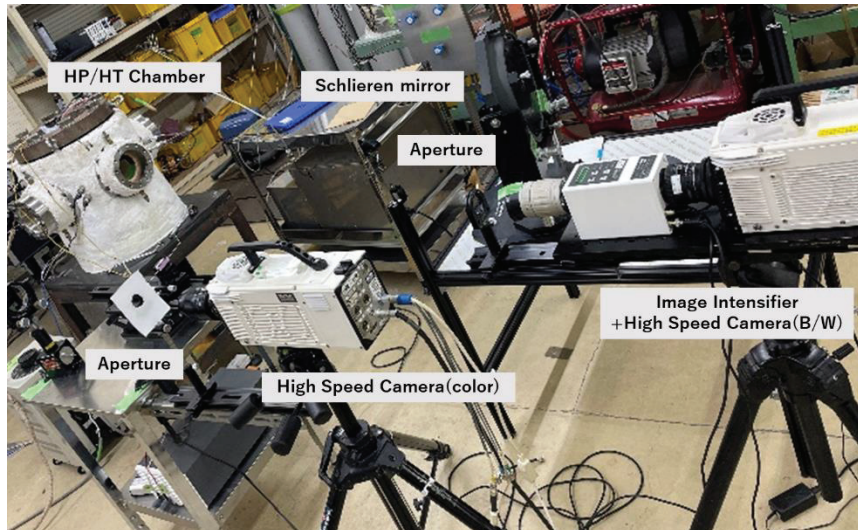


Fig. 2.10 High-Speed Laser Absorption Scattering (HS-LAS) schemes with optical system and constant volume chamber.



(a) Light sources



(b) Chamber and high-speed video cameras

Fig. 2.11 Photographs of High-Speed Laser Absorption Scattering (HS-LAS) optical system.

A schematic of the optical arrangement of the high-speed laser absorption scattering (HS-LAS) imaging system and the spray injection system is shown in Fig. 2.10. To carry out the experiment, a high-pressure, high temperature constant volume chamber was used. The chamber was cylindrical in shape with four optical windows, where two quartz windows of 100-mm-diameter were selected for spray visualisation. The injector was positioned on the top of the chamber. Moreover, to obtain the required injection pressure, a common rail system was used. Since the experiment was performed at evaporation condition, in the center of the lower part of the spray chamber an electric heater was positioned. Further, the insulator was stuck to the inner walls of the chamber. The necessary ambient temperature was controlled accordingly via the 20 A heating system. In order to monitor temperature at various locations in the spray chamber, three thermocouples were used. Since ultraviolet and visible light were used for the current study, the visible light was expanded to about $\phi 100\text{mm}$ diameter by a visible beam expander and passed through the convex lens whereas the ultraviolet light was passed through $\phi 50\text{mm}$ and $\phi 100\text{ mm}$ diameter convex lenses. A reflection mirror and a dichroic mirror made the two light beams coaxial and directed them to the beam diffuser to offer a homogeneous spray image background and passed through the fuel spray injected into a test chamber. After attenuated due to absorption and/or scattering of the fuel vapor and droplets, the light beams were reflected by the schlieren mirror. Then, the pair of beams was separated by another dichroic and a reflection mirror

directing the two beams into the respective high-speed video camera. The photographs of High-Speed Laser Absorption Scattering (HS-LAS) optical system is shown in Fig. 2.11. Fig. 2.11(a) indicates the light source side whereas Fig. 2.11(b) indicates the chamber and cameras sides.

2.5.3 Multi-Hole Injector Adaptor and Image Processing Area

A multihole injector adaptor was designed to carry out this experiment such that most of the spray plume can be visible which is shown in Fig. 2.12. The adaptor was connected to the upper part of the spray chamber. The injector was mounted to the adaptor such that at least one of the spray plumes could be perpendicular to the merged light beam. However, because of the actual viewpoint and blurriness of the window at high ambient pressure and temperature, the nozzle tip's location couldn't be seen clearly. Therefore, the first 7 mm downstream of the nozzle tip was eliminated from the original image during image processing to provide a synthetic and clean appearance of the data, as seen in Fig. 2.13. The Vis and UV images were then synchronized, ensemble averaging was applied to six image sequences recorded at each experimental condition. Finally, the line-of-sight images were deconvoluted using the onion-peeling method.

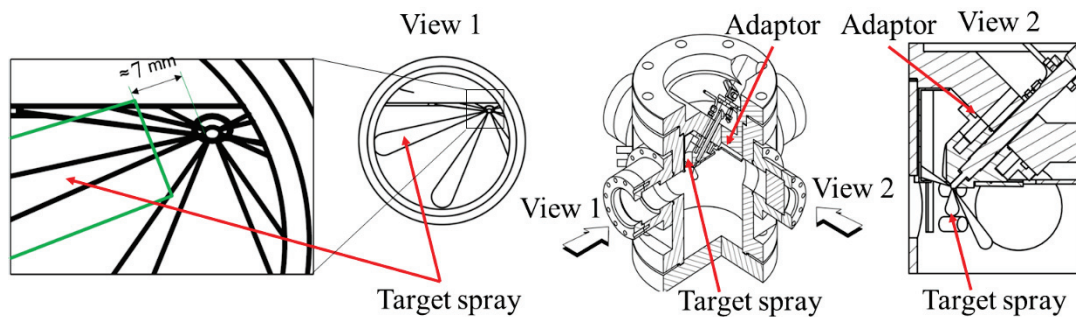


Fig. 2.12 Multi-hole injector adaptor and its image processing area.

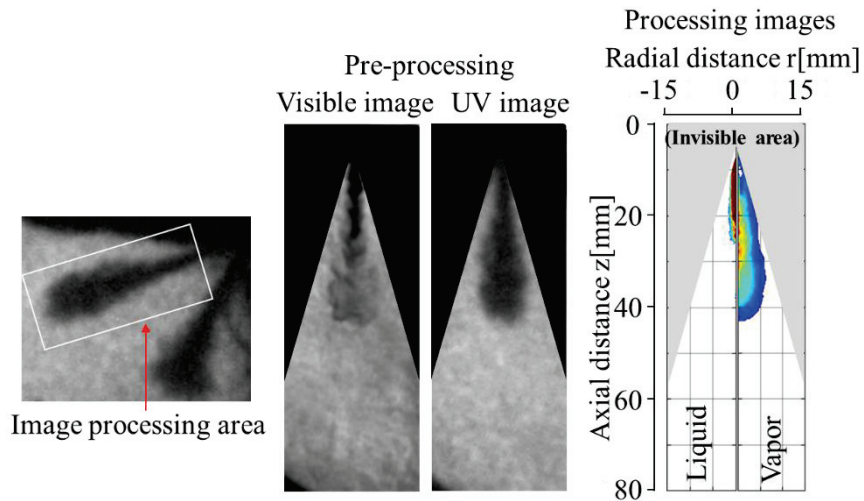


Fig. 2.13 Image processing sequence.

To obtain the vapor penetration and examine the mixture formation of the first and second injection of the split injection, it is desperately needed the separation of both injections. For the separate results of the first injection and second injection in accordance to optical thickness, the vapor penetration profiles of the first and second injection were separated. Fig. 2.14 depicts the separation procedure.

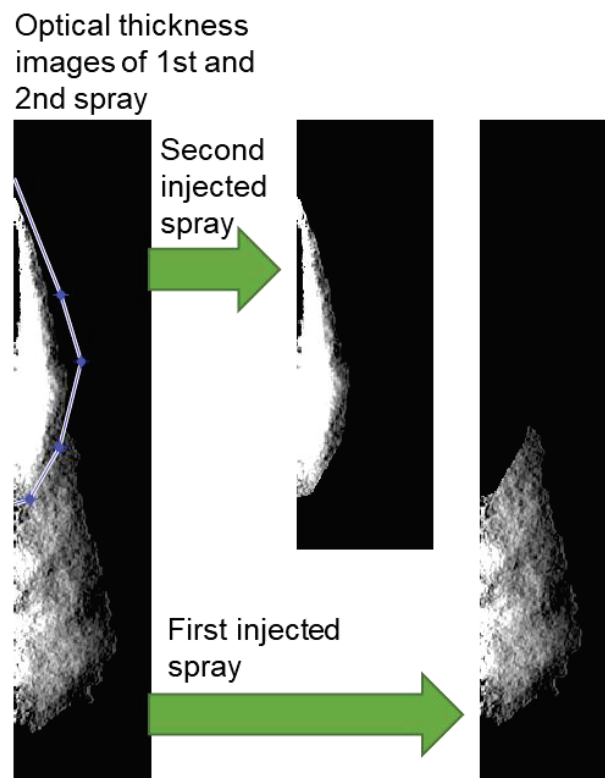


Fig. 2.14 Separation of the first and second injection from the optical thickness image.

2.6 MOLAR ABSORPTION COEFFICIENT MEASUREMENT

2.6.1 Principle of Molar Absorption Coefficient

When the light intensity attenuated by a certain substance is S_i , the light intensity before attenuation is R_i , and the light intensity due to dark current is D_i , the absorbance A_i is as follows.

$$A_i = -\log \left(\frac{S_i - D_i}{R_i - D_i} \right) \quad (2.12)$$

The absorbance of a substance increases proportionally with the concentration of the substance according to Lambert-Beer's law. Therefore, the horizontal axis is the molar concentration of the sample C_V [mol / m³], and the vertical axis is the slope when the absorbance A_i is taken. The value ϵ [L / mol · cm] when divided by L [cm] is the molar absorbance coefficient. In this study, the test fuel used was a tracer fuel obtained by mixing 1-MN2.5% as a tracer for absorbing ultraviolet light with Tridecane 97.5%, which simulated the physical properties of diesel fuel, diluted with Ethanol. Since the molar absorption coefficient of the test fuel at a wavelength of 266 nm is required to quantify the air-fuel mixture by the two-wavelength laser absorption and scattering method, the absorbance at a wavelength of 266 nm is measured in this study.

2.6.2 Problems with Conventional Absorbance Measurement

There were two problems with conventional absorbance measurement. The problems are shown below.

(1) Accurate injection of test fuel

The injection port is a simple valve, and the fuel vapor diffused into the outside air during the test fuel injection with the micro syringe, so the correct amount of fuel could not be injected. The needle was as long as 200 mm, and the test fuel inside the needle evaporated by a different amount for each measurement, which affected the variation in the measured values. If a known amount of fuel could not be injected, the exact molar absorption coefficient cannot be calculated, so this problem needs to be solved in the first place.

(2) Absorbance data acquisition method

It was not possible to measure the absorbance data in chronological order, and only the maximum value of the change in absorbance over time was extracted. Therefore, the phenomenon that the absorbance decreases over time could not be taken into consideration. Therefore, in chronological order, it is necessary to measure the absorbance data.

2.6.3 Improvement of Problem

(1) Accurate injection of test fuel

As shown in Fig. 2.15, by changing the injection port from the conventional valve to the one for gas chromatograph using a rubber stopper, it became possible to prevent the test fuel from diffusing into the outside air. By attaching the intake pipe directly to the inlet, it is no longer necessary to lengthen the needle of the micro syringe more than necessary, and it has become possible to shorten the needle length from 200 mm to 50 mm. Furthermore, the fuel dilution rate was able to reduce the effect of dead volume inside the needle by increasing from 5-fold to 8-fold dilution.



Fig. 2.15 Conventional(left) and new(right) injection port.

(2) Absorbance data acquisition method

In this study, we decided to measure the absorbance over time. This made it possible to consider the temporal changes in absorbance, which had been a problem from previous studies.

2.6.4 Experimental Setup

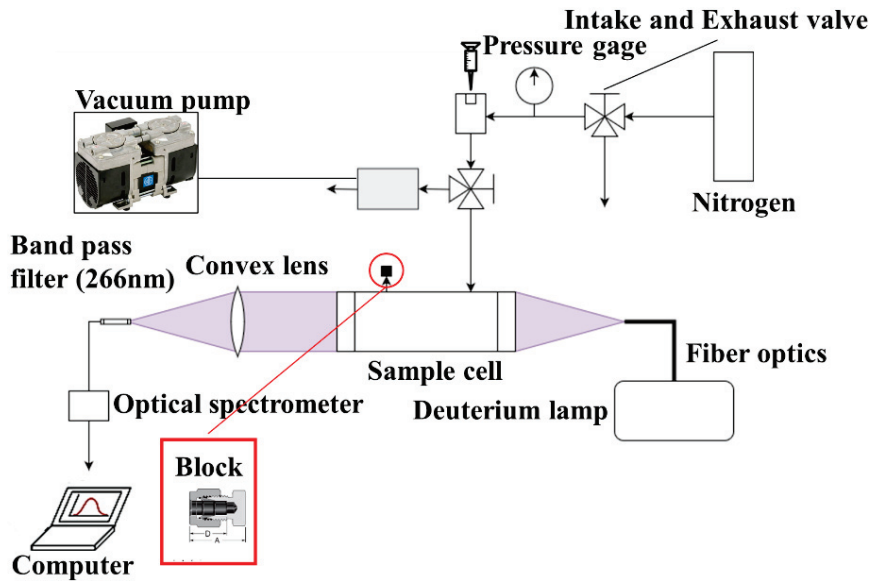


Fig. 2.16 Experimental set up for measurement molar absorption coefficient.

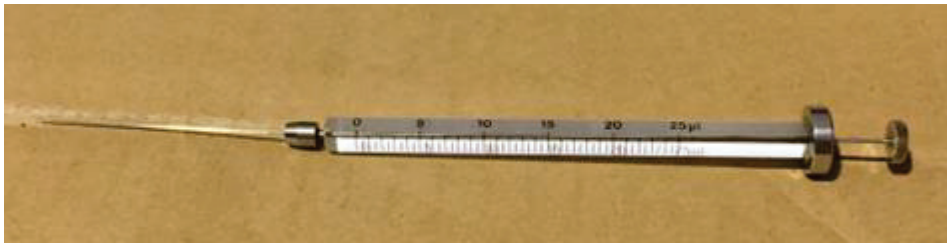


Fig. 2.17 Micro syringe for fuel injection.

The experimental setup of molar absorption coefficient is shown in Fig. 2.16. A 25 W deuterium lamp irradiates a high-temperature high-pressure cell with light in the wavelength range of 190 to 410 [nm]. A cantal wire was around the cell. The heater is wound and the temperature inside the cell can be raised to 650 degrees. In addition, the withstand voltage is designed to be 5 MPa, so it is possible to reproduce the experimental conditions simulating the actual machine environment. Test fuel is injected using the micro syringe shown in Fig. 2.17. If the test fuel has a high absorbance, saturation will occur with a small injection, so dilute it at an appropriate ratio with ethanol. Test the ultraviolet light transmitted through the fuel vapor is attenuated by the fuel vapor absorption and sent to the spectroscope through the detector, and the spectral distribution is sent to the computer.

2.6.5 Operation Procedure

1. The temperature inside the cell is raised to the target temperature by the heater, and nitrogen gas is sucked into the target pressure.
2. Start the light source and measure the light intensity R_i in the absence of the test fuel vapor. Adjust the band pass filter (266 nm) so that this light intensity is about 55000 units. It currently makes precise optical path measurements difficult. Check to make sure there are no factors (dirt on the observation window or residue in the cell).
3. After preventing the light from the light source from entering the detector, measure the light intensity D_i due to the dark current.
4. Open the exhaust valve once to release the pressure inside the cell. Then, inject the test fuel of the known concentration with a micro syringe and send it into the cell with nitrogen gas. At the same time, raise the pressure inside the cell to the target pressure.
 4. Measure the light intensity S_i of the transmitted light attenuated by the test fuel vapor in the test cell for 30 second after the end of intake. From this value, the absorbance is calculated on computer software and the time-series change of the absorbance at a wavelength of 266 nm is obtained.

2.7 TWO-COLOR PYROMETRY FOR FLAME TEMPERATURE AND SOOT CONCENTRATION MEASUREMENT

2.7.1 Experimental Setup

The combustion experiment was performed in the same chamber used for the evaporating spray experiment, as illustrated in Fig. 2.18. Photographs of the combustion flames were captured using a high-speed color camera (Hx-3, NAC Image Technology Inc.). With a resolution of 512×512 pixels and an exposure time of $1.2 \mu\text{s}$, the camera's frame

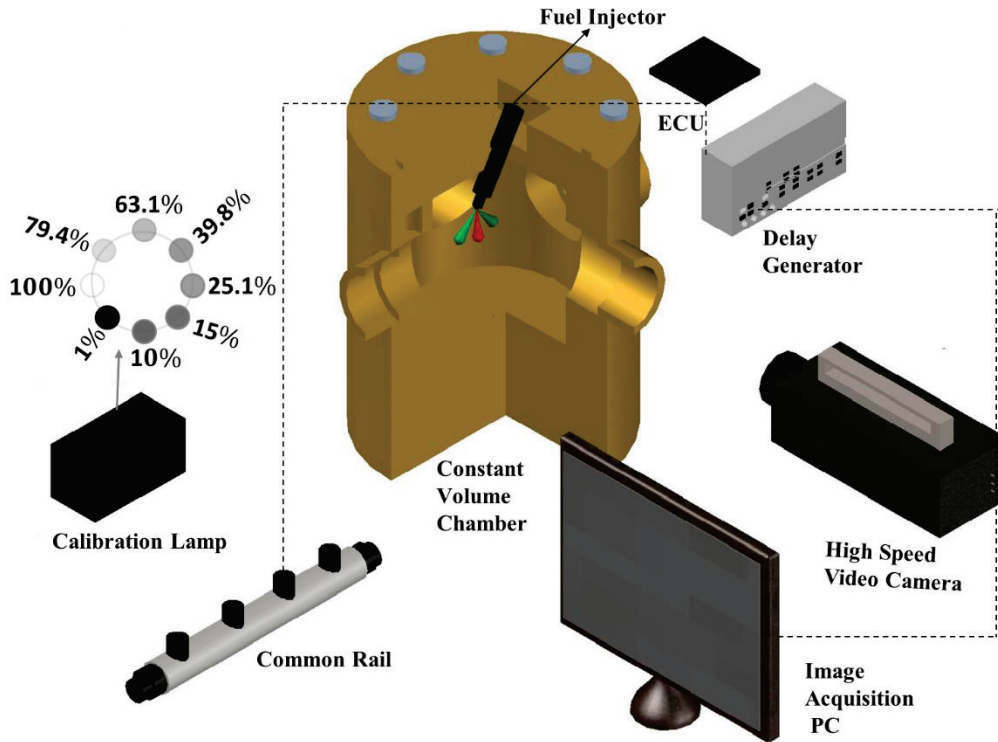


Fig. 2.18 Experimental setup for combustion.

rate was 30,000 frames per second. Using The Hottel and Broughton two-color method was applied by using Thermias software (Model SP-646) to calculate the soot concentration (expressed by the KL factor) and the flame temperature. Thermias is the thermal image analysis software which is characterized by obtaining the thermal image by the Two-color Method. Thermias can use both images of the color camera and monochrome camera. In the case of the color camera, it uses two-color combinations between the red and green color data. A detailed description of this method is provided in [131]. Furthermore, optical filters and a regular light illuminant were used to calibrate the method. Unlike non-blackbody emission conditions and Wien's formula, soot can be calculated for a single-wavelength action. The blackbody temperatures of the two different wavelengths can be determined using calibration data. In addition, the KL factor and soot temperature can be measured.

2.7.2 Principle of Two-Color Pyrometry

The monochromatic light emitting power of the black body $N(\lambda, T)$, which depends on the effective wavelength and the black body temperature, can be expressed according to Wien's equation as follows:

$$N(\lambda, T) = C_1 \lambda^{-5} \exp(-C_2 / \lambda T_a) \quad (2.13)$$

Where λ represent the wavelength, T_a is the black body's temperature and C_1, C_2 are the first and the second Plank's constants, respectively.

Under the non-blackbody emission conditions, the emission power is express as:

$$N(\lambda, T) = \varepsilon_\lambda C_1 \lambda^{-5} \exp(-C_2/\lambda T_a) \quad (2.14)$$

Where T represent the non-blackbody's temperature; ε_λ is the monochromatic light emissivity of the non-blackbody.

Hottel and Broughton's empirical correlations are used to estimate the soot particle ε_λ by the following equation [132]:

$$\varepsilon_\lambda = 1 - e^{(-KL/\lambda^a)} \quad (2.15)$$

Combining Eqs (2.13), (2.14) and (2.15) results in,

$$KL = -\lambda^a \ln \left[1 - \exp \left(-\frac{C_2}{\lambda} \cdot \left(\frac{1}{T_a} - \frac{1}{T} \right) \right) \right] \quad (2.16)$$

The KL value which is proportional to the summed soot concentration can be avoided, if two distinct wavelengths λ_1 and λ_2 are measured simultaneously:

$$\left[1 - \exp \left(-\frac{C_2}{\lambda} \cdot \left(\frac{1}{T_{a1}} - \frac{1}{T} \right) \right) \right]^{\lambda_1^a} = \left[1 - \exp \left(-\frac{C_2}{\lambda} \cdot \left(\frac{1}{T_{a2}} - \frac{1}{T} \right) \right) \right]^{\lambda_2^a} \quad (2.17)$$

Using calibration data, the black body temperatures T_{a1} as well as T_{a2} at two distinct wavelengths λ_1 as well as λ_2 , the KL value and the actual temperature can be calculated.

2.7.3 Calibration Method

After passing through the natural-density (ND) filter with transmittance of τ_i , the monochromatic light emitting power can be stated as,

$$N(\lambda, T) = \tau_i \varepsilon_\lambda C_1 \lambda^{-5} \exp(-C_2/\lambda T) \quad (2.18)$$

Eqs. (2.13) and Eq. (2.18) together provide the following result:

$$\frac{1}{T} - \frac{1}{T_a} = \frac{\lambda}{C_2} \cdot \ln(\tau_i \cdot \varepsilon_\lambda) \quad (2.19)$$

A thermos detector will be used to measure the temperature T, and the Eq. (2.19) will be sued to determined T_a if the transmittance is 1. For the calibration the empirical correlation $\varepsilon_\lambda = a_0 + a_a \lambda + a_2 T + a_3 \lambda T$ can be applied. The light intensity I that recognized by the camera sensor can be described as:

$$1 = a \varepsilon_\lambda C_1 \lambda^{-5} \exp \left(-\frac{C_2}{\lambda T} \right) + b \quad (2.20)$$

Where a as well as b are constants related to the camera sensor. Using the logarithm on both sides of Eq. (2.20), we obtain the following result:

$$\ln(1 - b) = -C_2/\lambda T + \ln(a \varepsilon_\lambda C_1 \lambda^{-5}) \quad (2.21)$$

This equation states that when the illuminant occurs, the connection between $\ln(1-b)$ and $1/T$ follows linearity. The term $-C_2/\lambda$ is the slope of the equation, in reverse, the following could be used to describe this system's effective wavelength:

$$\lambda_{effective} = -C_2/Slope \quad (2.22)$$

The intensity of the red, green, and blue bands could be measured in this experiment using a high-speed video color camera. Three useful wavelengths of the color camera (HX-3, Nac Image Technology Inc.) might be obtained:

$$\lambda_{red} = 577.38 \text{ nm}, \lambda_{green} = 541.12 \text{ nm}, \lambda_{blue} = 517.82 \text{ nm}$$

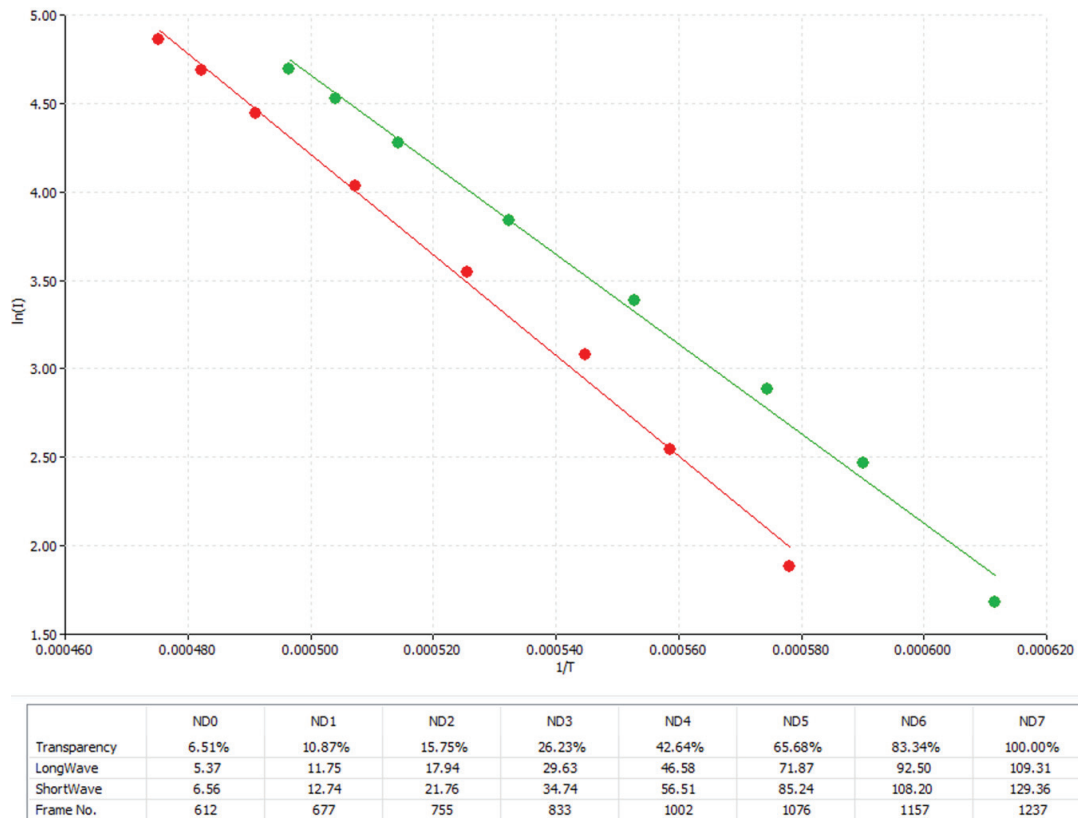


Fig. 2.19 Calibration graph sample.

Since only a small amount of spectrum overlap exists between the red and green channels' spectral responses, only these two channels are chosen for our two-color calculation [133]. When the light source is a standard illuminant, as illustrated in the left portion of Fig. 2.18, ε_λ will take on the value 1, and T will be substituted by T_a . After the camera captured eight different types of light intensity that were attenuated by eight different types of neutral-density filters, the data were calculated using Eq. (2.22). Afterward, a calibration line like Fig. 2.19 will be formed. In Fig. 2.19, the black body's temperature is shown along the vertical axis, and the camera sensor's real

intensity is shown along the horizontal axis. The camera sensor's actual intensity is represented by the expression $\ln(1-b)$, where b is a constant.

CHAPTER 3 MOLAR ABSORPTION COEFFICIENT OF TRACER LAS TEST FUEL

3.1 INTRODUCTION

In a direct-injection diesel engine, the spray characteristics have a large effect on the combustion and exhaust characteristics. The temperature dependence of the absorbance

of the tracer fuel used in the dual-wavelength laser absorption and scattering method. The absorbance was measured in this section to acquire the molar absorption coefficient that was used to calculate the concentration of the air-fuel mixture using the tracer LAS method. Here, the effect of atmospheric temperature and pressure on absorbance was investigated.

3.2 EXPERIMENTAL CONDITIONS

Table 3.1 represents the experimental conditions. Fig. 3.1 shows the frequency distribution of the air-fuel mixture temperature in the spray at an atmospheric temperature of 800K and the injection amount $Q = 5\text{mg}$, and Fig. 4.5 shows the temperature distribution of the air-fuel mixture in the spray. It can be seen that the temperature inside the spray varies from around 600K to 800K. In this study, the absorbance was measured in the range of 600-800K in order to verify the temperature dependence of the molar absorption coefficient that satisfies the temperature range that the air-fuel mixture in the spray can take. The test fuel is a tracer fuel diluted 8-fold with ethanol as a solvent and 1-MN diluted 321-fold with ethanol. Fuel is injected from the injection port using a micro syringe, and fuel vapor is sent into the measurement cell by inhaling nitrogen gas.

Table 3.1 Experimental Condition for Measurement of Molar Absorption Coefficient

Test fuel	Ethanol: Tracer fuel=7 :1	Ethanol: 1-MN=320 :1
Fuel injection amount	2, 4, 6, 8	4
Ambient pressure [MPa]	2.5, 3.0, 3.5, 4.0, 4.8	
Ambient Temperature [K]	550, 600, 650, 700, 750, 800	
Ambient gas	Nitrogen	

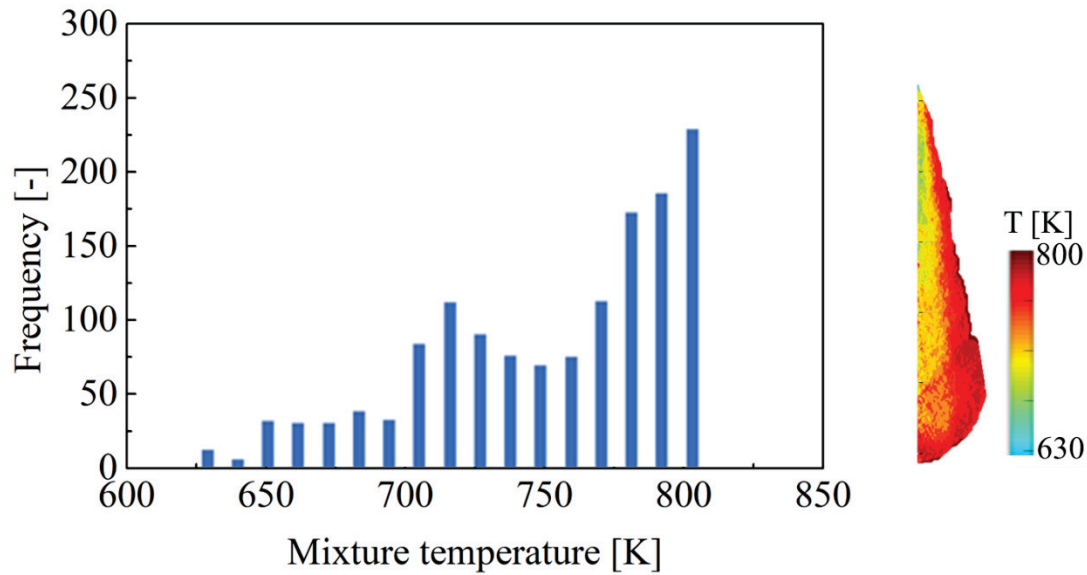
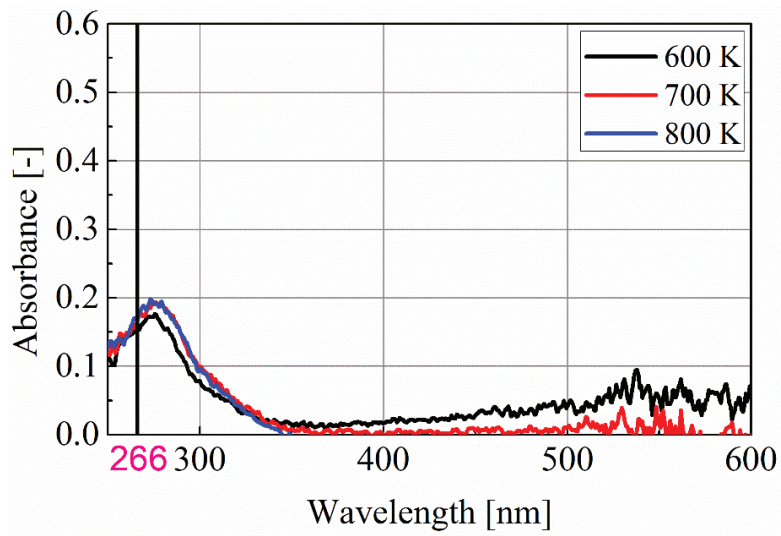


Fig. 3.1 Mixture temperature frequency distribution and mixture temperature inside the spray. ($T_a=800\text{K}$, $P_a=100$, $P_{inj}=5.0$ mg, 1.60 ms ASOI).

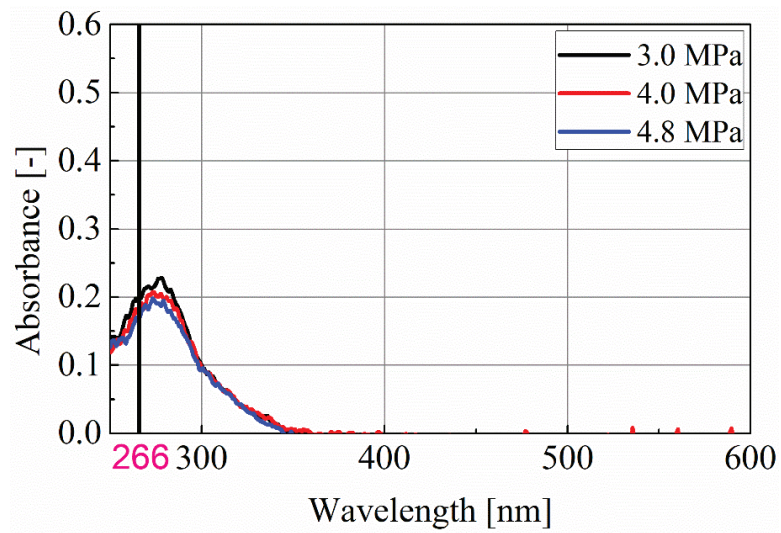
3.3 RESULTS AND DISCUSSION

3.3.1 Absorption Spectrum

Fig. 3.2 shows the absorption spectra of 1-MN for the different ambient temperature and different ambient pressure. For this absorption spectrum experiment the 1-MN was diluted 321-fold with ethanol and $4\mu\text{L}$ fuel was injected to the injection port by micro syringe. It can be observed that the 1-MN have absorbance at a wavelength of 266 nm. Fig. 3.2 (a) shows that for the high temperature case, the absorbance peak is greater, and the absorbance spread is narrower, while Fig. 3.2 (b) shows a low absorbance peak for the high-pressure case. Fig. 3.3 shows the absorption spectra of tracer fuel for the different ambient temperature and different ambient pressure. For this absorption spectrum experiment the tracer fuel was diluted 8-fold with ethanol and $4\mu\text{L}$ fuel was injected to the injection port by micro syringe. The absorption spectra near the wavelength of 266 nm are in similar value for the different temperature, and the absorbance peak is little higher for 700 k temperature case compared to other temperature cases. On the other hand, the absorption spectra around the wavelength of 266 nm are not agree with different pressure. For the low temperature case the absorption spectra peak is higher and absorbance spread is broader that other ambient pressure cases.

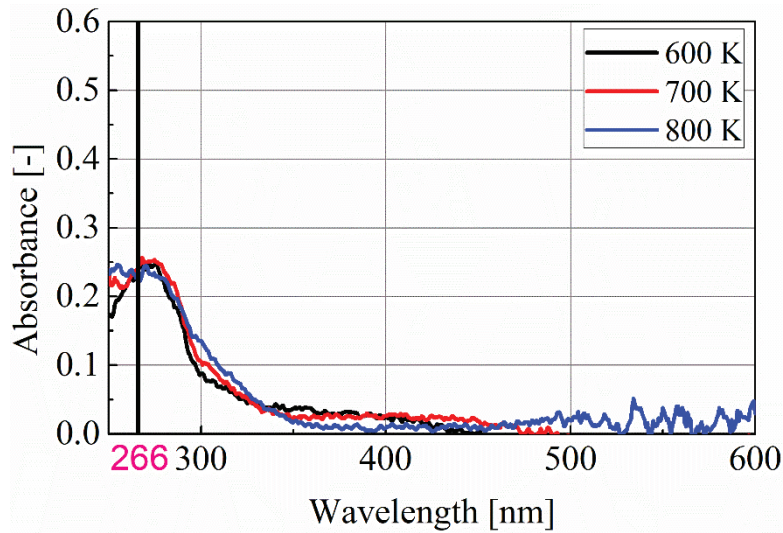


(a) Pressure $P_a = 4.8$ MPa

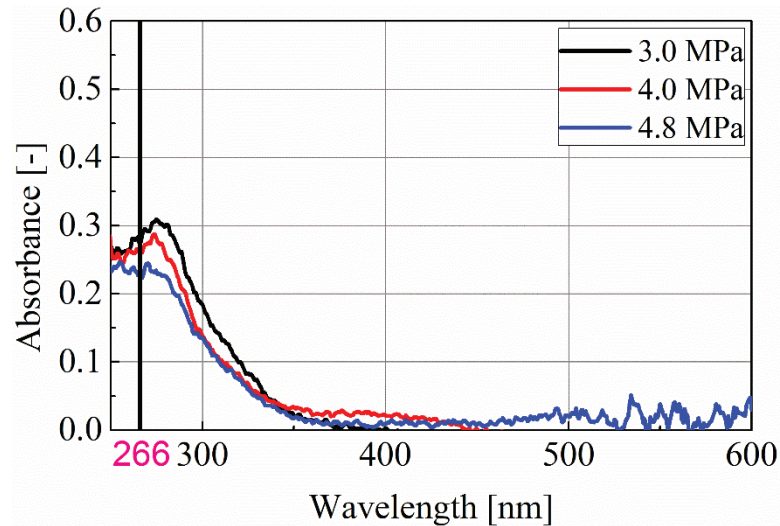


(b) Temperature $T_a = 800$ K

Fig. 3.2 Absorption spectrum on 1-MN (a) Different temperature, (b) Different pressure ($Q=4\mu\text{L}$).



(a) Pressure $P_a = 4.8$ MPa



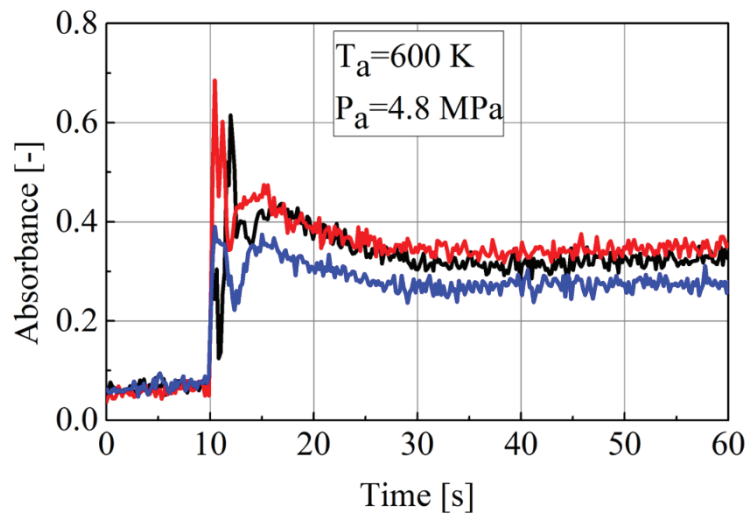
(b) Temperature $T_a = 800$ K

Fig. 3.3 Absorption spectrum on tracer fuel (a) Different temperature, (b) Different pressure ($Q=4\mu\text{L}$).

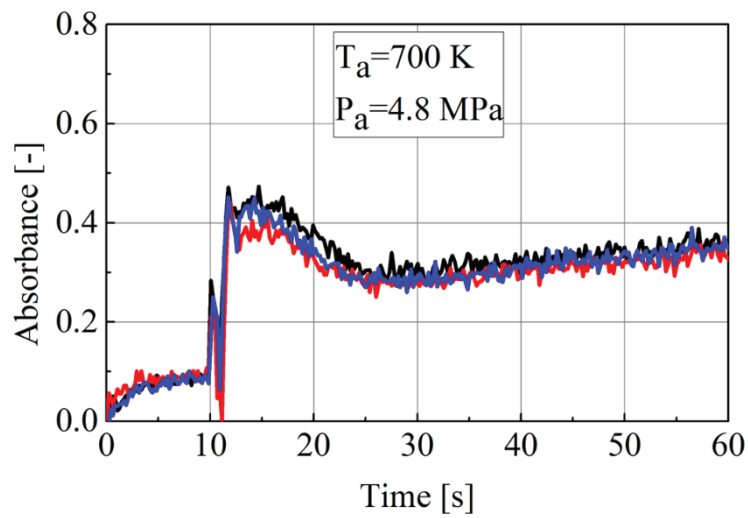
3.3.2 Temporal Variation of 266 nm Absorbance

Figs. 3.4 and 3.5 show the time-series measurement results of the absorbance for the 266nm wavelength when the atmospheric temperature is 600-800K and atmospheric pressure is 3.0-4.8 MPa whereas the fuel injection amount is $6 \mu\text{l}$. Injection of the test fuel and the start of time actuation of the spectrometer were same. After 10 seconds, the injected test fuel was sent into the cell with nitrogen gas by opening the intake valve. At the same time, raise the pressure inside the cell to the target pressure. Since the absorbance is not stable for about 20 seconds after fuel injection because uneven mixing of the injected fuel and the intake nitrogen gas occurs. From the Fig. 3.4 it can be

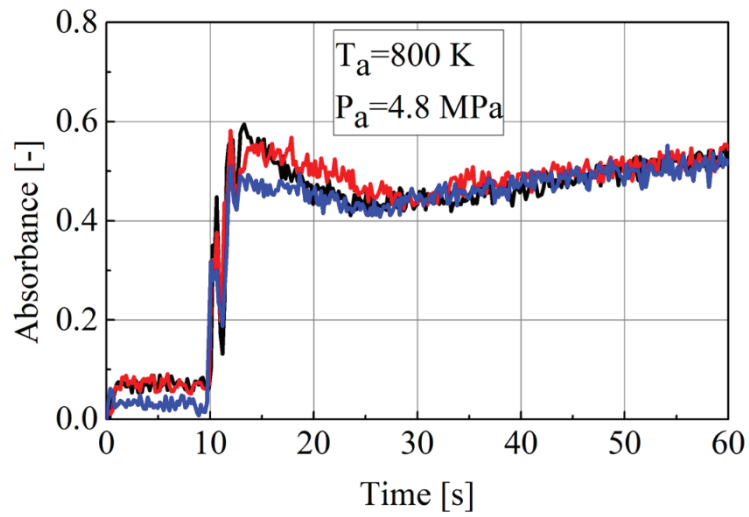
observed that for the low temperature case the absorbance is decrease after the peak value, on the other hand for 700 and 800K temperature cases the absorbance is decrease first then increase with time elapse. For the same temperature condition, the absorbance increasing rate is higher for the higher-pressure case which is shown in the Fig. 3.5. It can also be seen that the absorbance increases/decreases at a constant rate. It is considered that this is because thermal decomposition occurs in the tracer fuel.



(a)

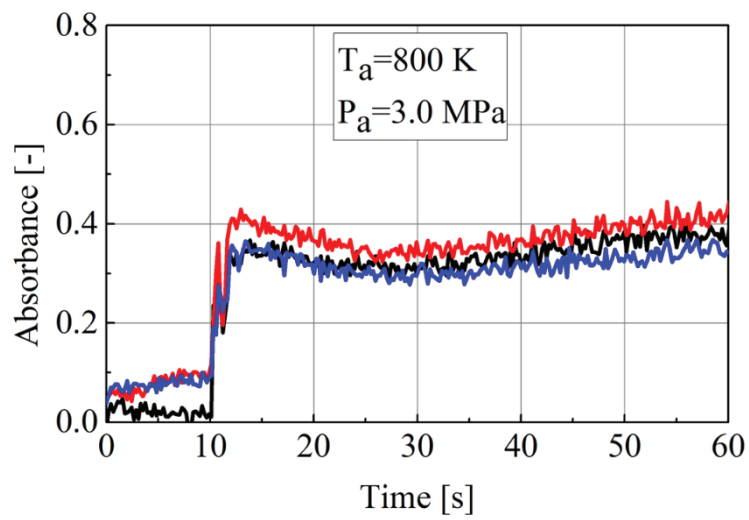


(b)

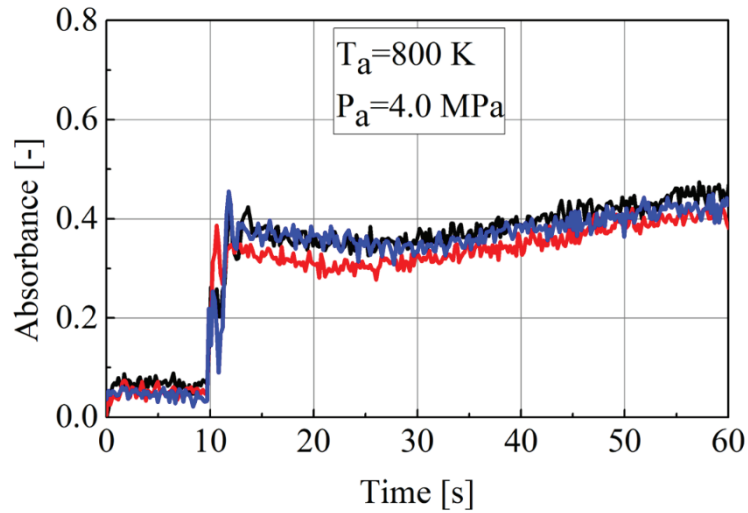


(c)

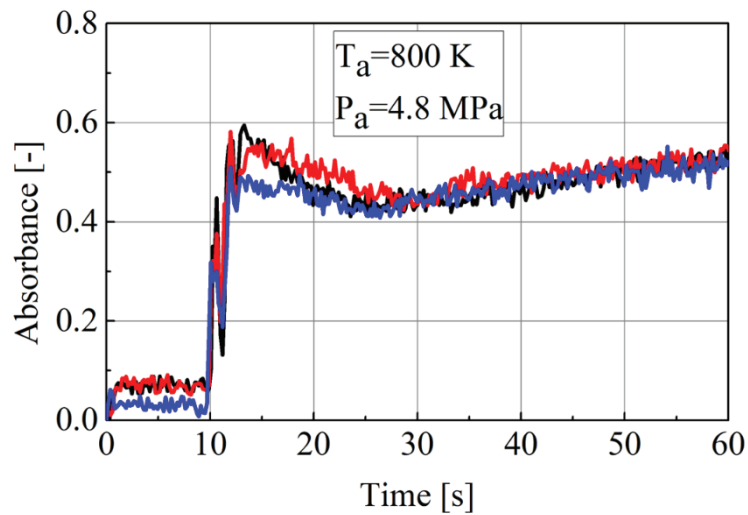
Fig. 3.4 Temporal change in absorbance of 266 nm wavelength for different ambient temperature ($Q=6\mu\text{L}$, $P_a=4.8\text{MPa}$).



(a)



(b)



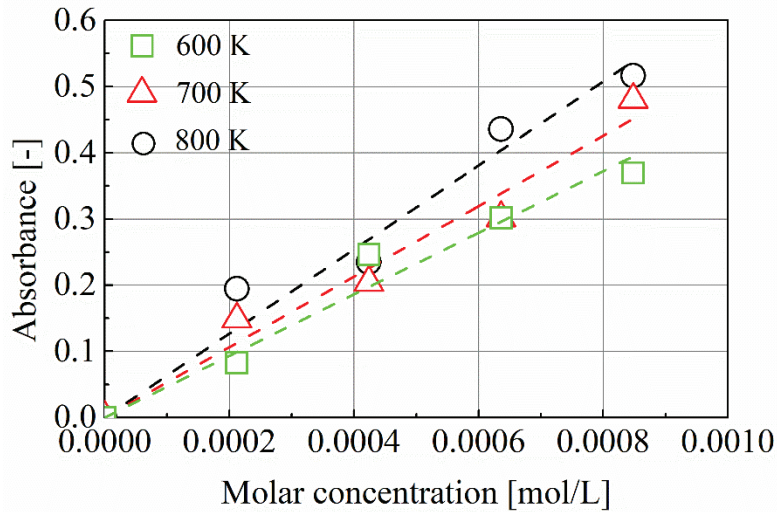
(c)

Fig. 3.5 Temporal change in absorbance of 266 nm wavelength for different ambient pressure ($Q=6\mu\text{L}$, $T_a=800\text{ K}$).

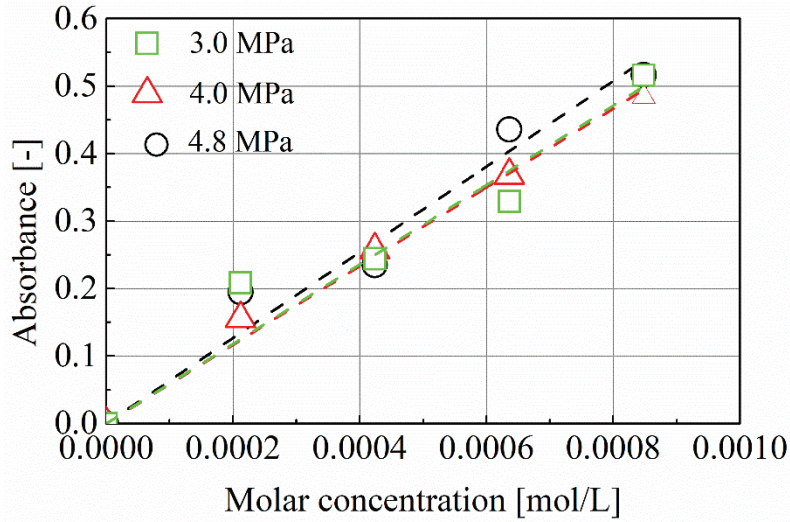
However, the value 20 seconds after intake valve is used as the representative absorbance value. Basically, in the tracer LAS and HS-LAS method, the measurement is performed within a few msec after injection, so it is considered that the influence of the change in absorbance due to thermal decomposition is small during the measurement. Therefore, in this measurement, as shown in Fig. 3.4 and 3.5, the part where the absorbance increased/decreased at a constant rate was linearly approximated, and the absorbance at 0 sec of fuel injection was obtained and used as the absorbance before the occurrence of thermal decomposition.

3.3.3 Correlation Between the Absorbance and the Concentration

When the measured absorbance increases, the light intensity of the transmitted light decreases and the S / N ratio decreases, so it is possible that the correlation between the absorbance and the concentration shifts. Fig. 3.6 shows the relationship between the measured absorbance and the molar concentration when the fuel injection amount is increased under typical conditions. It can be confirmed that the absorbance has linearity with respect to the molar concentration up to the typical conditions. It can also be seen that the measurement error is relatively small. In addition, the measurement error increases due to the increase in the S / N ratio. The better correlation can be seen for the 700 K temperature case compared to low and high temperature cases. On the other hand, there is an interesting phenomenon that can be seen in Fig. 3.6 (b). The best fitting line of the 3.0 and 4.0 MPa cases are almost similar. Overall, Fig. 3.7 demonstrates a positive linear connection between molar concentration and absorbance, which is in accordance with Lambert-equation Beer's law and satisfies the test fuel property's condition (3).



(a) Pressure $P_a = 4.8$ MPa



(b) Temperature $T_a=800\text{ K}$

Fig. 3.6 Absorbance with varied molar concentration (a) Different temperature with pressure $P_a=4.8\text{ MPa}$ (b) Different pressure with temperature $T_a=800\text{ K}$.

3.3.4 Molar Absorption Coefficient on the Effect of Atmospheric Temperature and Pressure

Fig. 3.7 shows the molar absorption coefficient at 266 nm of tracer fuel vapor in the atmospheric temperature range of 600-800K. According to the Beer's law, $A=\epsilon bc$, where A represents the absorbance, $b=10\text{ cm}$ represents the path length of the used cell, c is the molar concentration and ϵ is the molar absorption coefficient. As a result, the slopes of the absorbance versus concentration curve shown in Fig. 3.6 can be used to determine the molar absorption coefficient. From the Fig. 3.7 the molar absorptivity is found to have a low temperature dependence. However, for the 4.8 MPa condition, when the atmospheric temperature reaches 800K, the absorbance tends to increase compared to the range of 550K-750K. The mixture temperature inside the spray can be estimated using bulk temperature in an analyzing technique [134]. As a result, the molar absorption is defined as function of temperature Eq. (3.1)

$$\epsilon(T_{mix}) = 10^{(0.00059 \cdot T_{mix}) + 1.67} \quad (3.1)$$

Liquid absorption is neglected, as specified in the principle of the LAS technique, since it is much weaker than the scattering. Fig. 3.8 shows the molar absorption coefficient at 266 nm of tracer fuel vapor in the atmospheric pressure range of 2.5-4.8 MPa. From Fig. 3.8, it can be found that the molar absorptivity is found to have a small pressure dependency. At atmospheric pressure 2.5, every temperature condition shows the

similar value except for the 550K temperature condition. However, compared to the range of 550K-750K atmospheric temperature conditions, the molar absorption coefficient increases at 4.8 MPa atmospheric pressure and 800K atmospheric temperature.

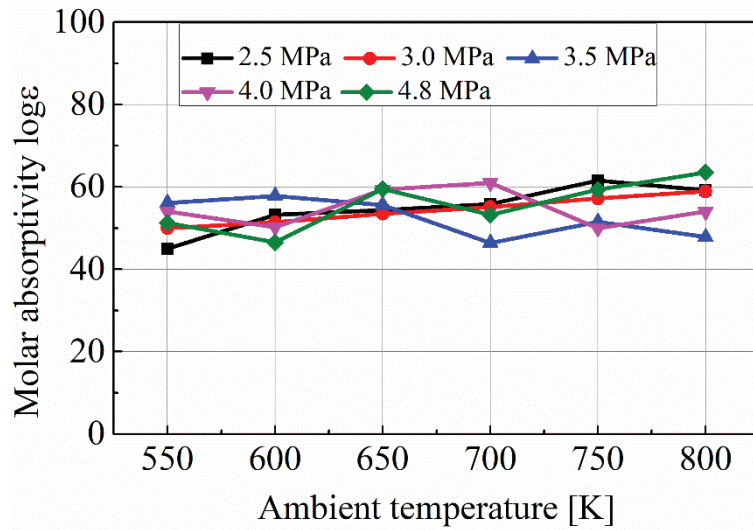


Fig. 3.7 Molar absorption coefficient dependence on ambient temperature (Tracer fuel).

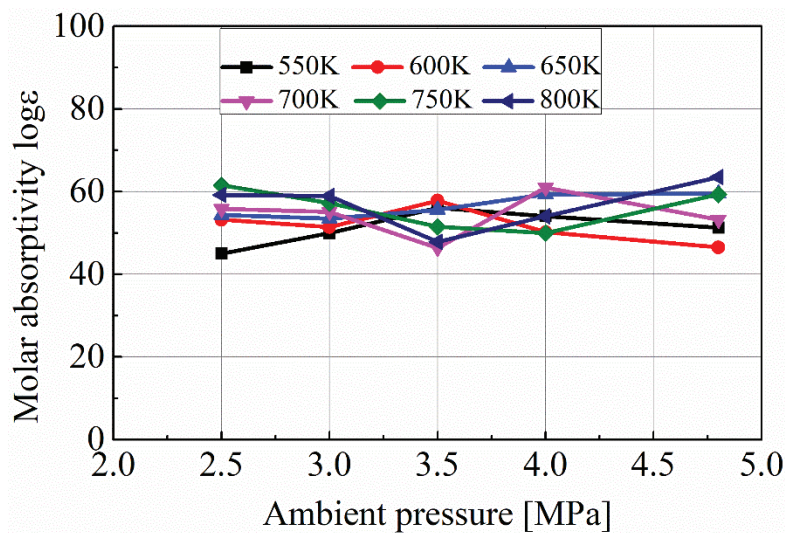


Fig. 3.8 Molar absorption coefficient dependence on ambient pressure (Tracer fuel).

Fig. 3.9 shows the molar absorption coefficient of 1-MN at each atmospheric temperature calculated from the absorbance measured for the tracer fuel and the molar absorption coefficient obtained in previous studies. In this study, the absorbance was obtained from the time-series measurement data in consideration of the effect of thermal

decomposition, so the molar absorption coefficient is higher than in previous studies. Since the order of the values of the tracer fuel and the 1-MN molar absorption coefficient are different. Except for 700K temperature, the correction line touches almost all of the molar absorption values at the various temperatures. This indicates that the 1-MN molar absorption coefficient has negligible temperature dependence. For 1-MN, the temperature dependence is consistent with the temperature dependence of the tracer fuel. From this, it can be confirmed that the absorbance of the tracer fuel is due to the absorbance of 1-MN.

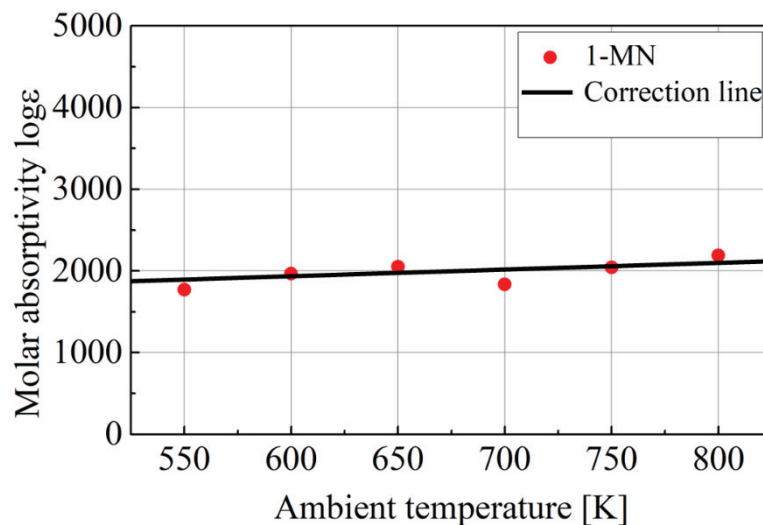


Fig. 3.9 Molar absorption coefficient dependence on ambient pressure (1-MN fuel, $P_a=4.8$ MPa).

3.4 SUMMARY

For the absorption spectrum experiment the 1-MN was diluted 321-fold and the tracer fuel was diluted 8-fold with ethanol, whereas 4 μ L fuel was injected to the injection port by micro syringe. After 10 seconds, the injected test fuel was sent into the cell with nitrogen gas by opening the intake valve. At the same time, raise the pressure inside the cell to the target pressure. Since the absorbance is not stable for about 20 seconds after fuel injection because uneven mixing of the injected fuel and the intake nitrogen gas occurs. The value 20 seconds after intake valve is used as the representative absorbance value.

The main conclusions are summarised as follows:

1. It can be seen that the 1-MN have absorbance at a wavelength of 266 nm. For the high temperature case, the absorbance peak is greater, and the absorbance spread is narrower. The absorption spectra near the wavelength of 266 nm are in similar value for the different temperature.
2. Absorbance has linearity with respect to the molar concentration up to the typical conditions. The best fitting line of the 3.0 and 4.0 MPa cases are almost similar.
3. The molar absorptivity is found to have a low temperature dependence. For the 4.8 MPa condition, when the atmospheric temperature reaches 800K, the absorbance tends to increase compared to the range of 550K-750K.

CHAPTER 4 SPLIT INJECTION ON MIXTURE FORMATION AND COMBUSTION

4.1 INTRODUCTION

Diesel engines are used in agricultural, power, shipping, transportation sectors and as prime movers in the heavy equipment due to their overall superior performance and reliability. In compression ignition engines, both the fuel spray and fuel mixture are crucial as they are inextricably linked to the combustion process and engine performance. Direct fuel injection techniques provide a high degree of versatility for injection control in diesel engines, in terms of engine load state, speed, pressure, and cycle action.

Over the last few decades, the concept of homogeneous charge compression ignition has been extensively researched, along with several similar approaches such as low temperature combustion and partially premixed charge compression ignition. A huge amount of inert gas, like exhaust gas recirculation (EGR), is introduced into the engine's intake to increase the ignition delay and allow enough time for mixing. However, the inherent problem of such a concept is the instantaneous auto-ignition of multi-point, which causes a significant amount of heat release in a short period of time under high load conditions. One of the probable solutions to suppress such a rigid heat release is a fuel stratification strategy [10], which can be accomplished through multiple (or split) injection procedures. A study conducted on a modern engine has revealed the possibility of achieving high efficiency at 48% efficiency with partially premixed combustion (PPC) and multiple injections concepts [135]. Therefore, observing the mixture formation and combustion process with a long ignition delay (for example, where the combustion of the first injected spray has not yet occurred by the start of the second injection) is also important for better understanding and providing insight for future optimization.

This study aims to investigate the effects of the split ratio and dwell time on mixture formation, combustion, and soot characteristics of the diesel spray with split injection. First, the laser absorption-scattering (LAS) technique (Conventional LAS) was employed for the study and analysis of mixture formation, particularly the vapor evaporation ratio, liquid phase and vapor phase distribution, vapor mass, and

equivalence ratio. Second, a high-speed video camera monitored the combustion processes via the two-color system. Finally, the temperature of the flame and distribution of soot concentrations expressed by the KL factor have been discussed, where K is the coefficient of absorption and L is the geometric stiffness including its spray flame along the optical detection axis.

4.2 EXPERIMENTAL CONDITIONS

An overview of the experimental conditions is summarised in Table 4.1. The injection pressure was 100 MPa. A seven-hole injector with a hole diameter of 0.123 mm was connected to the top of the chamber by a special adapter. The ambient temperature, pressure, and density for the evaporation and combustion experiments were chosen as 800 K, 4.8 MPa for evaporation while 4.6 MPa for combustion, and 20.2 kg/m³, respectively.

Table 4.1 Experimental conditions

	Evaporating condition	Combustion condition
Ambient gas	N ₂	Air (O ₂ 21%, N ₂ 79%)
Pressure [MPa]	4.8	4.6
Temperature [K]	800	
Density [Kg/m ³]	20.2	
Injection pressure [MPa]	100	
Fuel	Tracer LAS Fuel	JIS#2 Diesel Fuel
Injector type	Piezo type Denso G3P	
Number of holes	7	
Nozzle diameter [mm]	0.123	
Injection amount	5 mg/ hole	
Split ratio	3:7 5:5 7:3	
Dwell time [ms]	0.12 0.32 0.54	

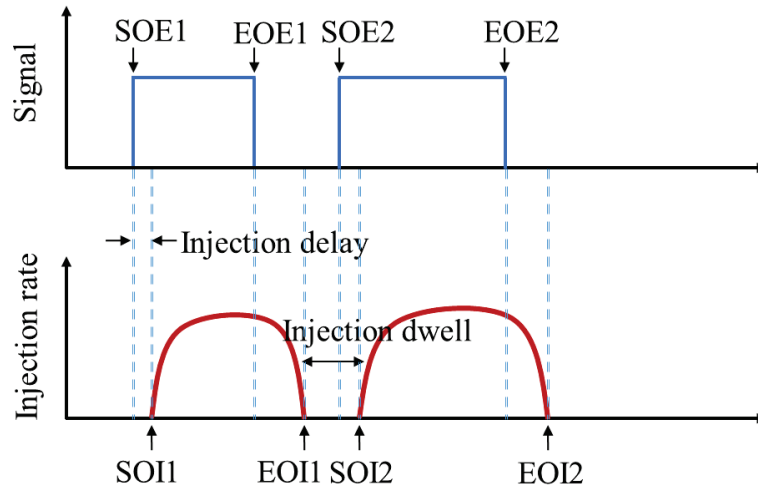


Fig. 4.1 Schematic of the relationship between injection signal and injection rate.

This ambient situation propagates the thermodynamic atmosphere close to the top dead centre (TDC) of a low-compression internal combustion engine in compression stroke, which can effectively achieve homogeneous combustion. A description of the dwell time is shown in Fig. 4.1. The dwell time that can be obtained from the injection rate measurement is the time interval between two real injections, but not between the two signal pulses. By observing the history of the real-time injection rate until the desired target values were reached, the dwell time between the two signal pulses i.e., start-of-energizing (SOE) and end-of-energizing (EOE) was controlled. The injection rate was monitored with an injection rate measurement metre (Onosokki, FJ-0700) and the result was recorded. The split ratios, i.e., 3:7; 5:5, and 7:3 were selected while the dwell time were 0.12s; 0.32s, and 0.54s. The tracer LAS fuel (97.5% of n-tridecane and 2.5% of 1-methyl-naphthalene) was selected for the evaporation condition, and JIS#2 diesel was preferred for the combustion experiment. To avoid self-ignition, nitrogen was used as the ambient gas for the evaporation experiment and ambient air (a mix of 21% of O₂ and 79% of N₂) was used as the ambient gas for the combustion condition.

4.3 EFFECT OF SPLIT RATIO

4.3.1 Injection Rate

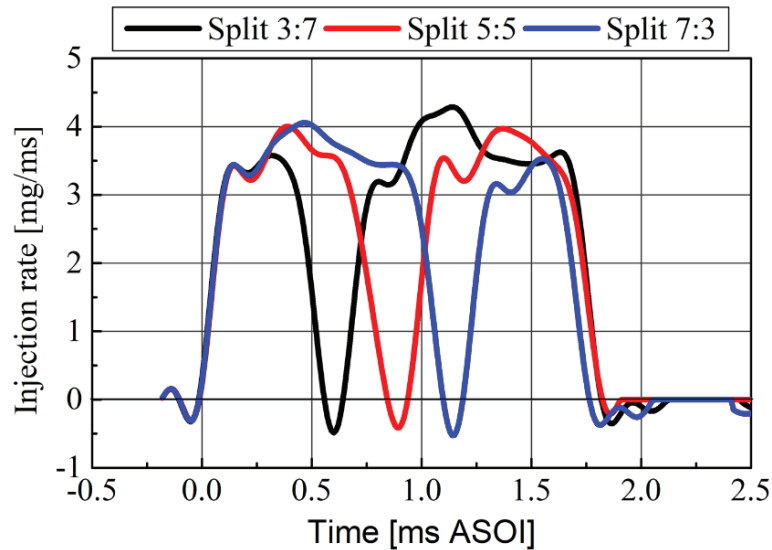


Fig. 4.2 Temporal variation of the injection rates for the 3:7, 5:5, and 7:3 split ratios.

Fig. 4.2 depicts the results of the injection rate profiles of the split injection processes that were obtained by applying the single-cylinder multiple injection rate estimation technique. The Zeuch method, detailed in [136], was applied to estimate the injection rate. As already mentioned, a seven-hole injector with a hole diameter of 0.123 mm was chosen to measure the injection rate, and the mass of fuel injected was 5.0 mg/hole. The two types of fuel i.e., tracer LAS and diesel were identical in terms of quantity. The end of injection EOI2 timings were almost the same for the three split ratios. The process of mixture formation with different split ratios has been discussed at the EOI1 timings and EOI2 timings and comprehensively compared in the next section.

4.3.2 Spray Mixture Concentration Distribution

Figs. 4.3 to 4.5 represent the equivalence ratio contours of the spray under the 3:7, 5:5, and 7:3 split ratios, respectively. The image acquisition timings are EOI1, SOI2,50%, and 100% of the EOI2 from the left side to the right side for each split ratio, to show the spray characteristics. In each set of images, the spray of the liquid phase is shown on the left and the vapor phase on the right. Further, the highest equivalence ratios for the liquid and vapor phases are 4 and 3, respectively, for all the conditions. The total quantity of air entrainment has a corresponding relationship with the spray length and

spray angle [15,16,18]. The spray angles of all the injection strategies identical owing to the same pressure and ambient conditions. However, for the 3:7 split ratio, the second injection fuel ‘caught up’ with the fuel of the first injection; thus, the shape of the spray appeared as though it is a single spray event. The first spray overlapping the second together with lower penetration did not submit enough air entrainment into the spray region. Consequently, the richer mixture areas are longer than the other injection strategies. In contrast, the lower amount of fuel in the second part of the 7:3 split ratio resulted in a lower penetration towards the spray tip of the second injection, where the air entrainment wave still improved. The lean area of the first injection resulted from a leaner mixture with an equivalence ratio on the total to provide less fuel for the second injection. Therefore, compared with the other split ratios, the 7:3 split ratio (Fig. 4.5) results in the best lean mixture formation because of the location of the second injection. A similar finding has shown improvement in emissions by avoiding fuel-rich areas through injection rate shaping [137]. A reversed-delta shape was realised by gradually decreasing the injection rate.

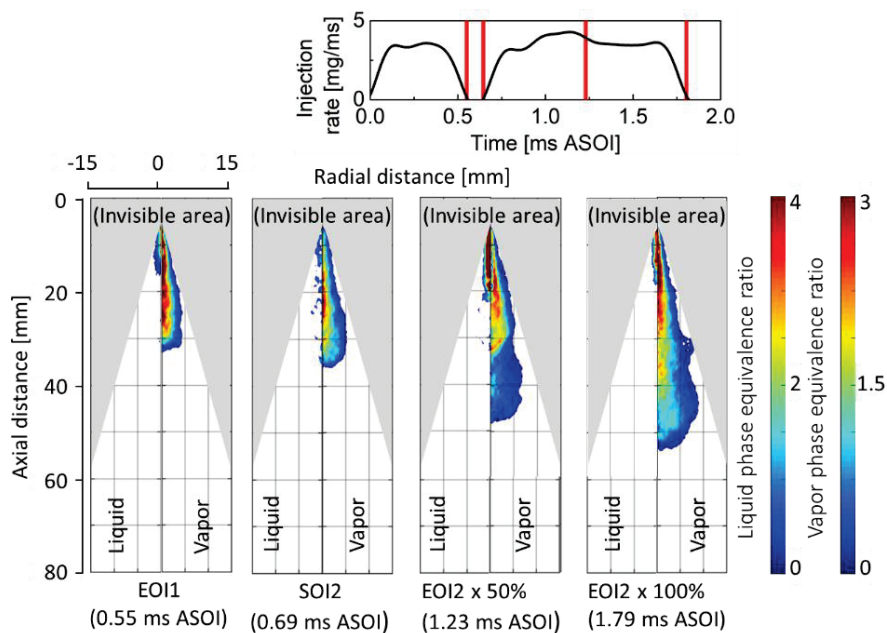


Fig. 4.3 Temporal development of liquid and vapor phase equivalence ratio distributions of spray, split ratio 3:7.

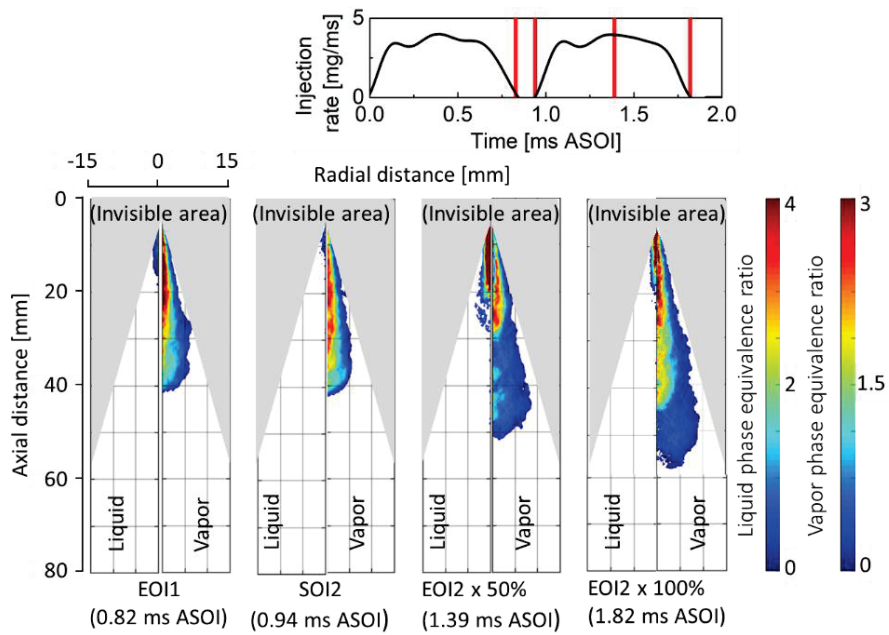


Fig. 4.4 Temporal development of the liquid and vapor phase equivalence ratio distributions of spray, split ratio 5:5.

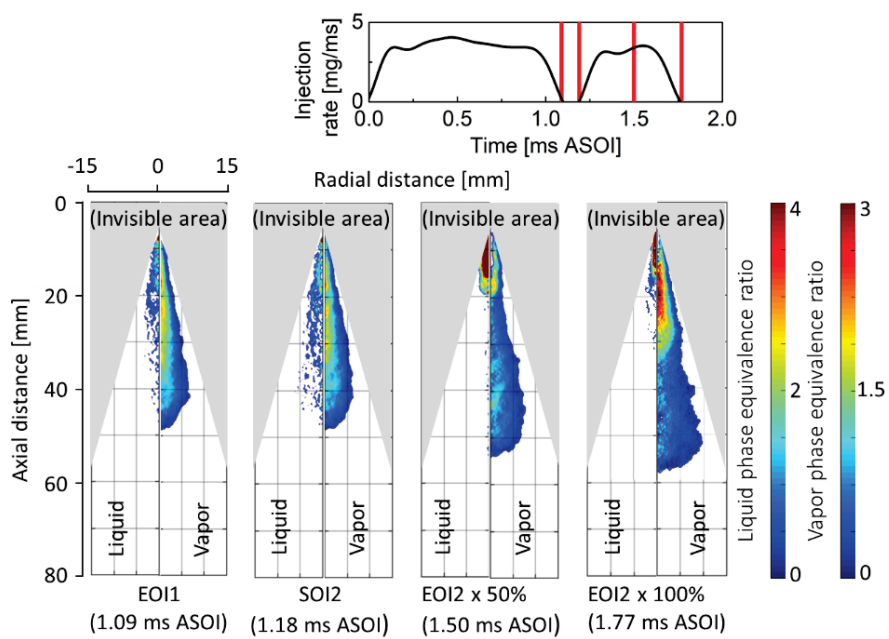


Fig. 4.5 Temporal development of the liquid and vapor phase equivalence ratio distributions of spray, 7:3 split ratio.

By applying the less ‘catch-up’ technique of the following spray, by continuously decreasing the injection rate, it is possible to achieve a highly homogeneous mixture formation.

Fig. 4.6 shows the temporal variation of the evaporation ratio for the three split ratios. The evaporation ratio was estimated using the following equation:

$$E_r(t) = \frac{V_m(t)}{T_m(t)} \quad (4.1)$$

where $E_r(t)$ is the evaporation ratio at a specific time; $V_m(t)$ and $T_m(t)$ are mass of the vapor and total injected fuel, respectively, at a specific time. The mass of vapor was measured from image processing and mass of the total injected fuel was measured by the integral of the injection rate profile.

However, for the first half injection of all the injection strategies, the evaporation ratio under the 3:7 and 5:5 split ratios was higher than that under the 7:3 split ratio. A possible cause was that the mass of the first injected fuel of these setups was lower than that of the others, implying that the smaller is the amount of fuel injection, the faster it evaporates [138]. Nevertheless, for the 5:5 split ratio, the vaporization ratio at the start of the second injection was greater than the other timing. This was because after the end of the first injection, during the dwell time, a negligible amount of fuel was injected after the start of the second injection, but the evaporation was continuous. Moreover, for the 7:3 split ratio, the evaporation ratio at 1.77 ms after the end of the second injection is somewhat greater than at the end of the first injection. This implies that the marginal injection quantity of the second injection increases the injected fuel mass velocity, which is lower than the evaporation rate [139].

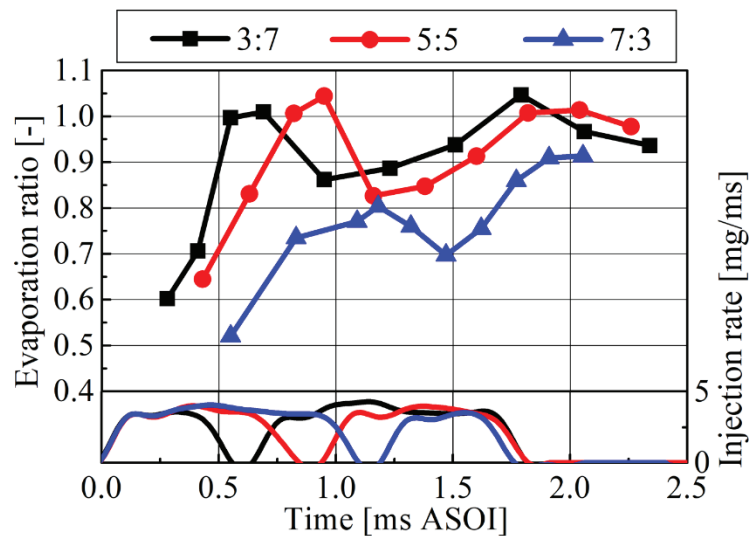
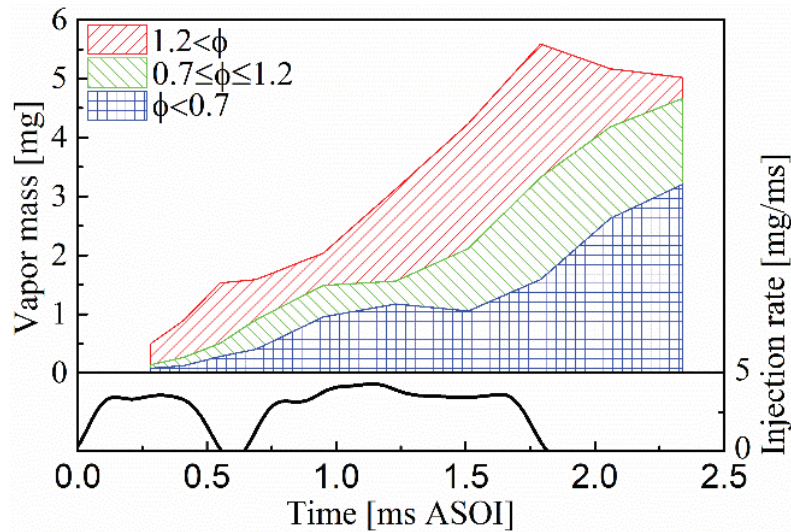


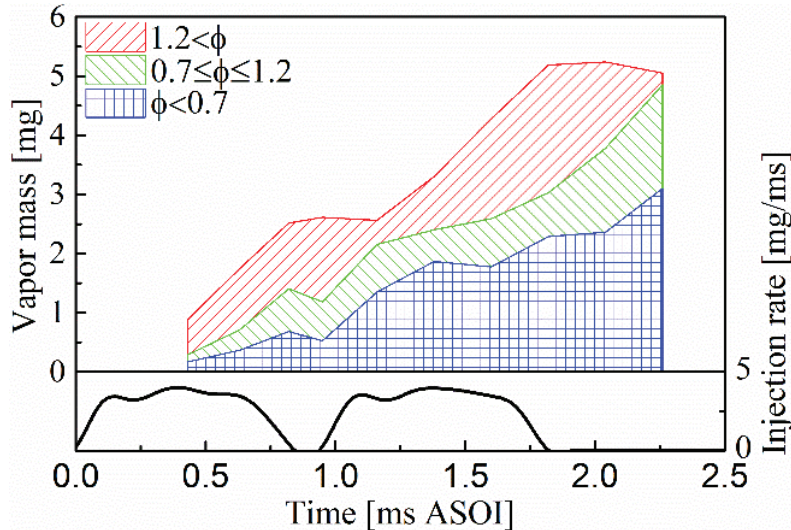
Fig. 4.6 Evaporation ratio of the spray under the 3:7, 5:5, and 7:3 split ratios.

The temporal variation in the quantities of vapor mass in the spray is depicted in Fig. 4.7. However, the quantities of the vapor mass were calculated statistically at a certain

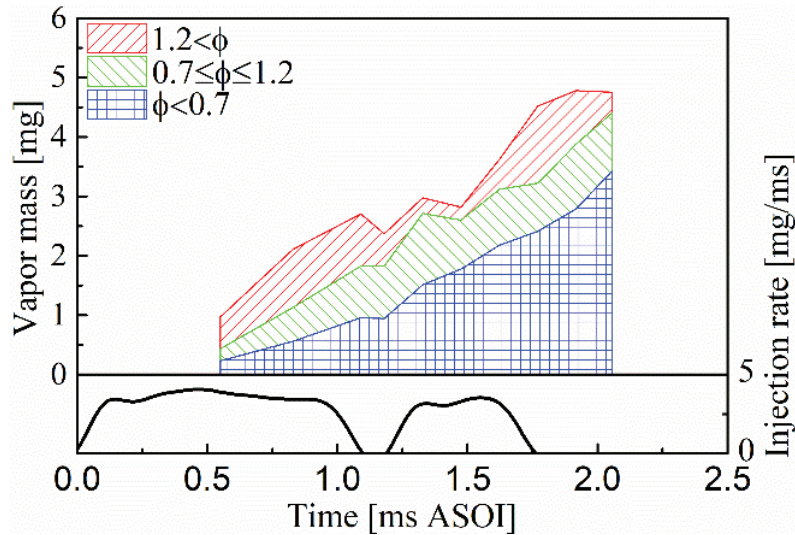
time. The start time was selected after the completion of fifty per cent of the first injection of each type of injection, as is evident from the injection rate profile shown below. Subsequently, “the stable operation limit” is defined by the domain of $0.7 \leq \phi \leq 1.2$ as a recommendation for the evaluation of “over lean” or “over rich” mixtures [140].



(a) Split ratio 3:7



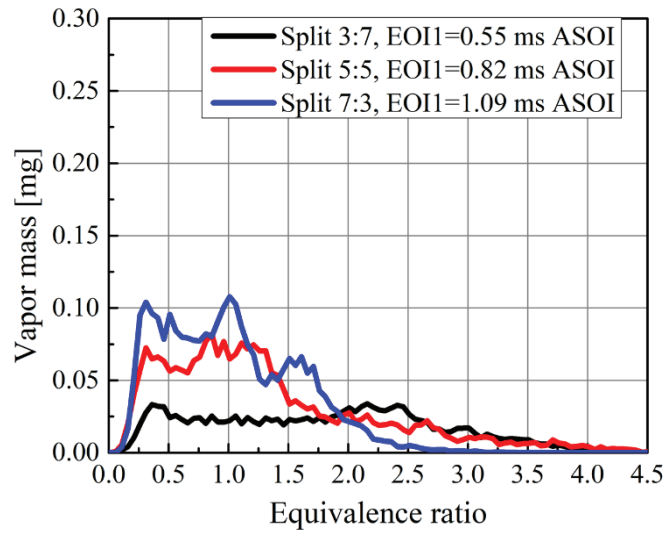
(b) split ratio 5:5



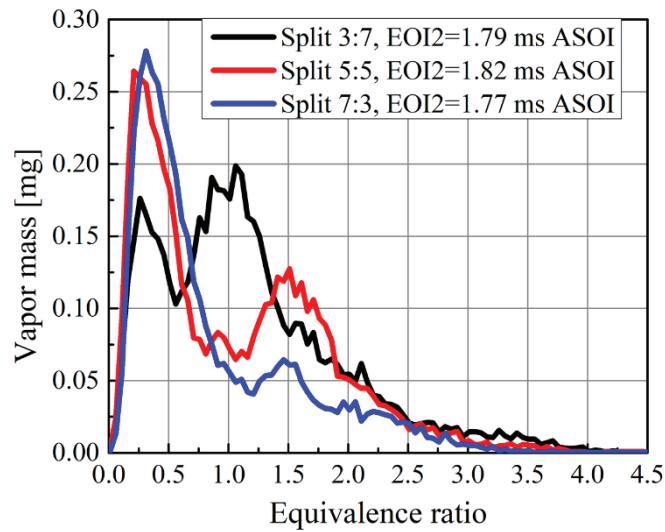
(c) Split ratio 7:3

Fig. 4.7 Temporal variations of quantities of the vapor phase in the sprays (a) split ratio 3:7, (b) split ratio 5:5, and (c) split ratio 7:3.

As shown in Fig. 4.7 (a), the equivalence ratios manifest a jagged distribution as the time elapsed. Overall, the 3:7 split ratio resulted in a wide “over rich” mixture inside the spray. The reason being that the vapor of the second spray merged with the vapor of the first spray, made the compact geometry and consequently turned into an “over rich” mixture. Moreover, the reduced injection quantity of the second injection under the 7:3 split ratio also achieved an appropriate positioning of the second injection into the boundary of the first injection by gradually increasing the “over lean” mixture and avoiding the large zone of the rich mixture. Fig. 4.8 illustrates the relationship between the vapor mass distribution and equivalence ratio for the three split ratios. However, Fig. 4.8 (a) is aligned to the EOI1 time domain, while Fig. 4.8 (b) is aligned to the EOI2 time domain, for each of the three split ratios. Although the peak value of the vapor mass of the 7:3 split ratio fluctuated after EOI1, after EOI2 it gradually moved towards the lower equivalence region due to the lower vaporisation rate, as explained in detail in Fig. 4.6. The overall mass distribution reveals that the total mass of the lean mixture and the equivalence ratio is smaller for the 7:3 split ratio. The safety of penetration could be essential for the free spray [77]. Regardless, during the injection of a fixed volume of fuel its penetration needs to be controlled, such as inside the combustion chamber of the engine. Therefore, it was necessary to look for the best split injection strategies and the 7:3 split ratio was found to be better than the others.



(a) EOI1

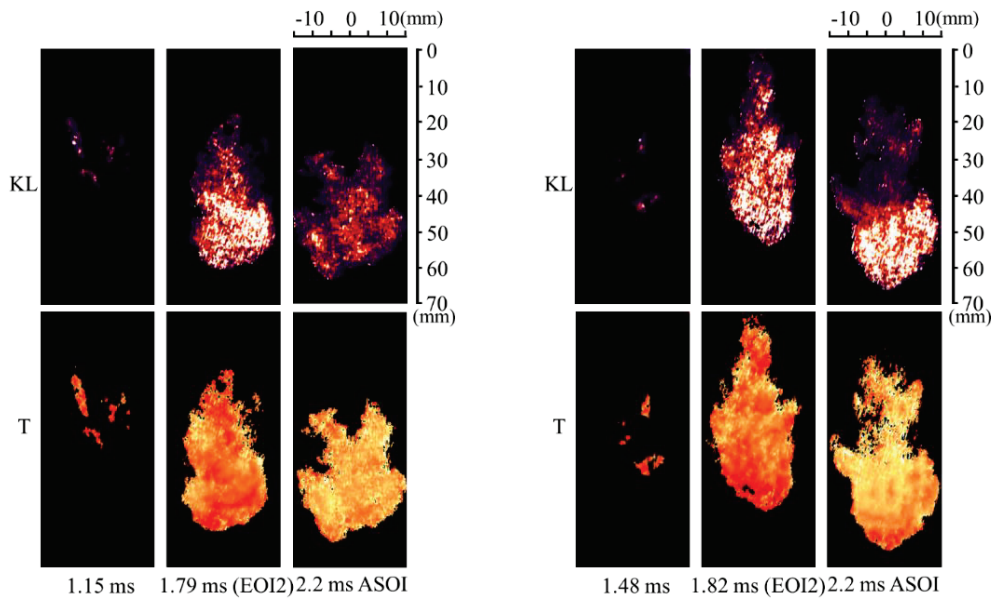


(b) EOI2

Fig. 4.8 Relationship between the vapor mass distribution and the equivalence ratio at (a) EOI1 and (b) EOI2.

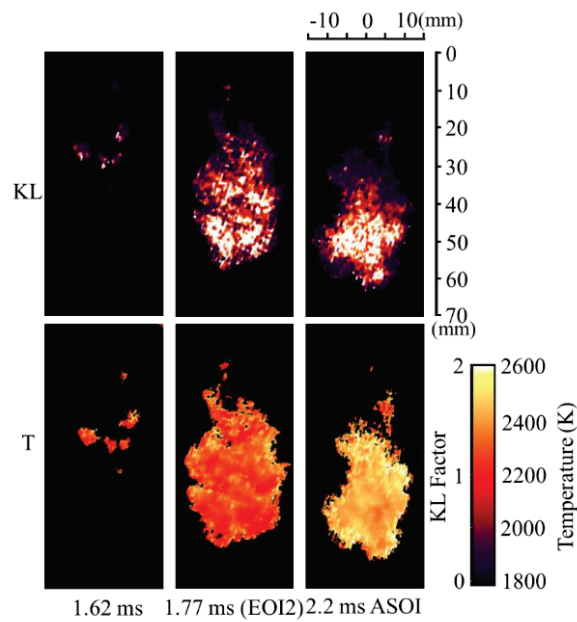
4.3.3 Spray Combustion Characteristics

The results of the combustion process for different split ratios are presented in this section. Fig. 4.9 shows the temperature distribution and the KL factor obtained using the two-color pyrometry system to evaluate images recorded by the high-speed video camera. The temperature obtained here was the temperature of the soot. Measurements were taken three times for each injection strategy.



(a) Split ratio 3:7

(b) Split ratio 5:5



(c) Split ratio 7:3

Fig. 4.9 Pseudo-color images of the KL factor and flame temperature (a) split ratio 3:7, (b) split ratio 5:5, and (c) split ratio 7:3.

The three output sets appeared for every injection strategy, but a single collection of the result was chosen for every injection strategy. In Fig. 4.9, the images in the lower row display the temperature for each injection technique while the images in the upper row display the KL factor. The timings indicated are from the start of ignition (SOI), after the end of injection, and at 2.2 ms after the start of injection (ASOI) for the 3:7, 5:5,

and 7:3 split ratios. After the EOI2 timing, Fig. 4.9 (a) and 4.9 (b) show that the spray flame soot is mainly concentrated at the tip region at EOI owing to the enormous momentum. For the temperature image, the comparatively high temperature in the lower magnitude of a sooting frame persists at 2.2 ms ASOI. For the 3:7 and 5:5 split ratios, the second injection caught up with the tip of the first injection. This resulted in the formation of a higher KL factor allocation in the flame tip region at EOI. Further, for the 7:3 split ratio, the fuel of the second injection just reaches the fuel of the first injection at EOI2. This flame image suggests that the depletion effect did not influence the preceding flame and did not lead to a higher KL factor allocation near the flame tip region, as mentioned in a previous study [146].

The integrated KL factor ASOI is reported in Fig. 6.10 for the three split ratios. The integrated KL factor of the 7:3 split ratio first increases and then progressively decreases. In contrast, the integrated KL factor of the other two split ratios fluctuate. Evidently, the integrated KL factor for the 7:3 split ratio is smaller than the others. The reason being that the appropriate ‘positioning’ of the second spray has injected into the lean region of the first spray primarily because of the considerably higher atomisation and significantly advanced air entrainment. The integrated KL factor of the 3:7 and 5:5 split ratios at the instant of 2.0 ms ASOI is higher than that of the 7:3 split ratio. The second fuel injection caught up with the first injection flame tip, which deteriorated the combustion leading to higher soot production. At that instant, the integrated KL factor of 5:5 split ratio is maximum, even more than that of the 3:7 split ratio because the amount of fuel in the first injection was comparatively higher than that of the other. Moreover, the KL factor gradient of the 7:3 split ratio from the 2.7 ms point to the last edge of the ignition is significantly higher than that observed for the other split ratios. There was no significant variation in the spray flame oxidisation speeds between the first two split ratios, which implies that the 3:7 and 5:5 split ratios rapidly decrease the soot. Therefore, the 7:3 split ratio could be considered an optimal condition due to higher absolute combustion, faster reaction speed, and relatively low soot emissions.

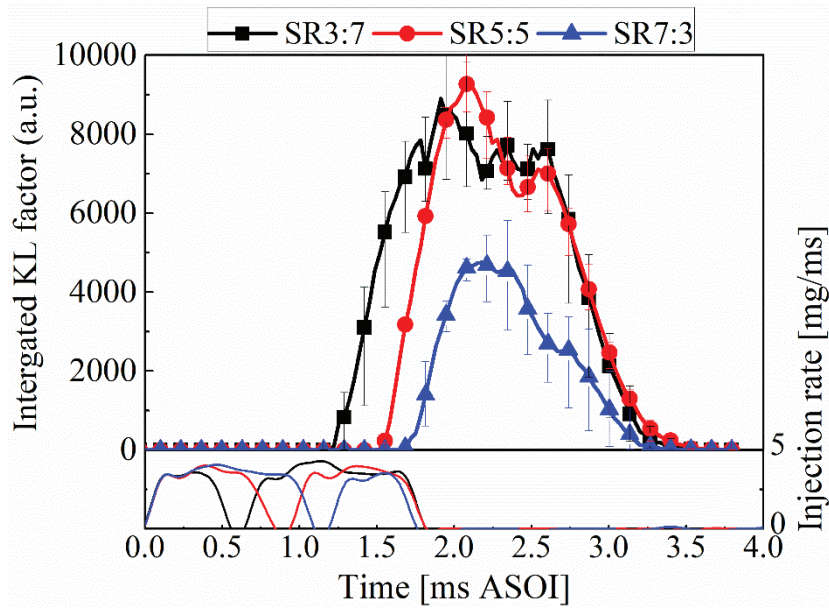
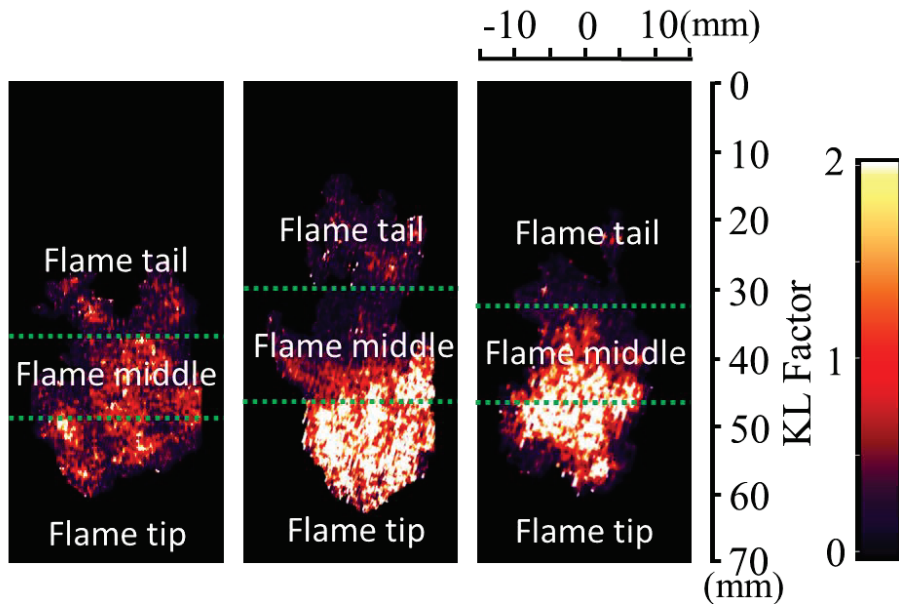


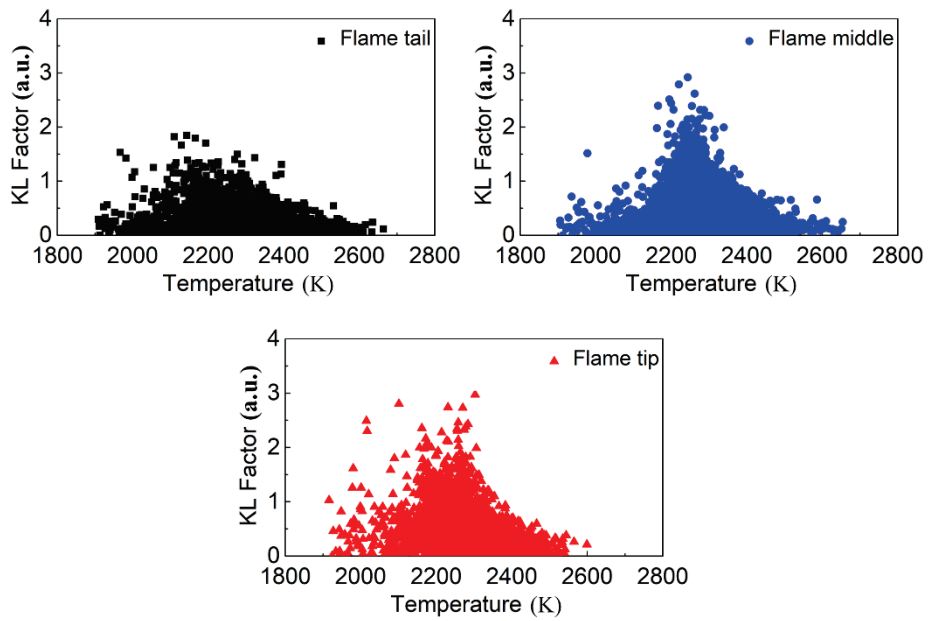
Fig. 4.10 Integrated KL factor ASOI under three split ratios 3:7, 5:5, and 7:3.

Fig. 4.11 illustrates the KL factor distribution at 2.2 ms ASOI at the three split ratios. The KL factor images are divided into three zones i.e., flame tip, flame middle, and flame tail, as shown by the green dashed lines in the images. Fig. 4.12 shows the KL factor versus flame temperature in these three regions, with an enormous number of scattered pixels of the KL values. The maximum KL factor was 2.0 for the tail and 3.0 for the middle and tip of the whole frame region. A small KL factor was detected in the flame tail region, while the high KL factor was in the flame middle and tip regions, for every injection setup, because at this instant the spray could not provide adequate fresh air to the flame tail region. Under the 7:3 split ratio, the KL factor of the tail was observed to be thin and small which indicated the ability of the 7:3 split ratio to reduce soot. The high KL factor of the flame tail region of the 7:3 split ratio was smaller than that of the other split ratios which implied that the 7:3 split ratio could produce maximum soot reduction. In contrast, for the 5:5 split ratio, at the flame middle and tip regions, the KL and high KL factors were considerably higher than those for the other split ratios. This implied that the maximum soot was generated by the 5:5 split ratio. Thus, the 7:3 split ratio has a significant effect on the soot reduction of KL against the flame temperature.

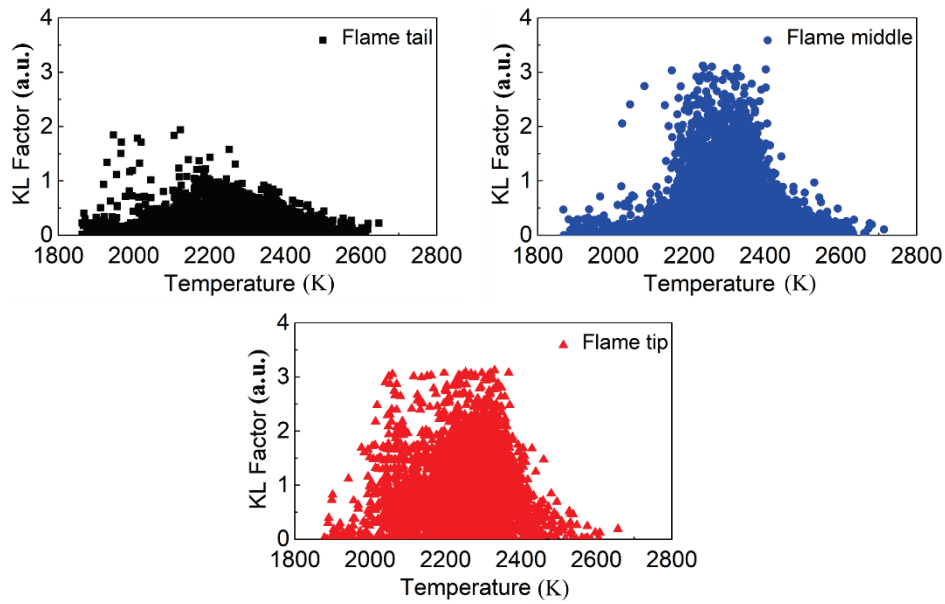


(a) Split ratio 3:7 (b) Split ratio 5:5 (c) Split ratio 7:3

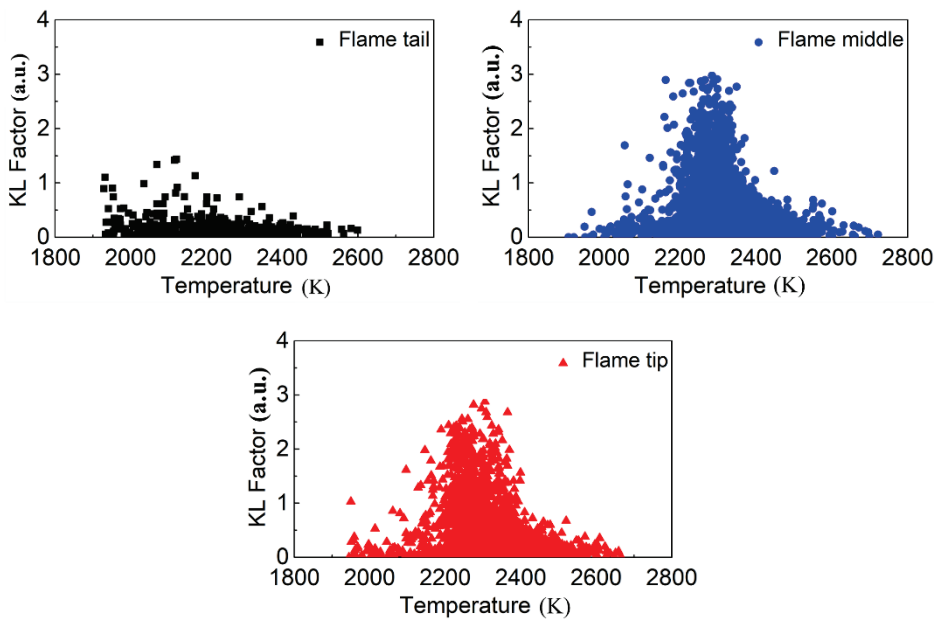
Fig. 4.11 KL factor distribution at 2.2 ms (ASOI) for (a) split ratio 3:7, (b) split ratio 5:5, and (c) split ratio 7:3.



(a) Split ratio 3:7



(b) Split ratio 5:5

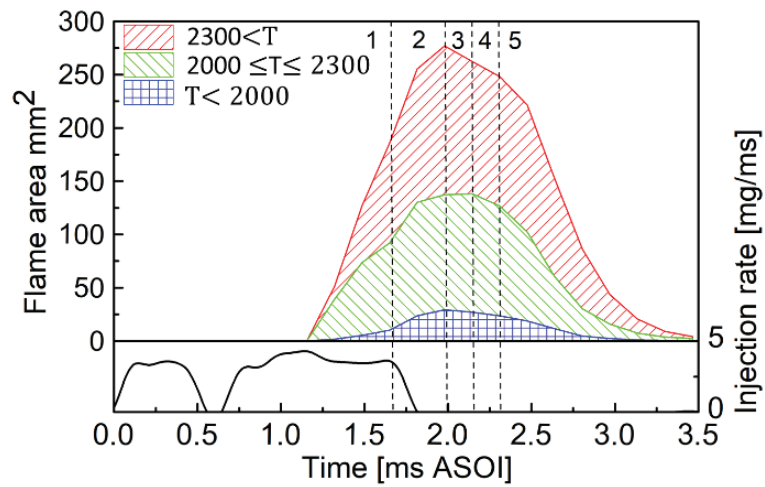


(c) Split ratio 7:3

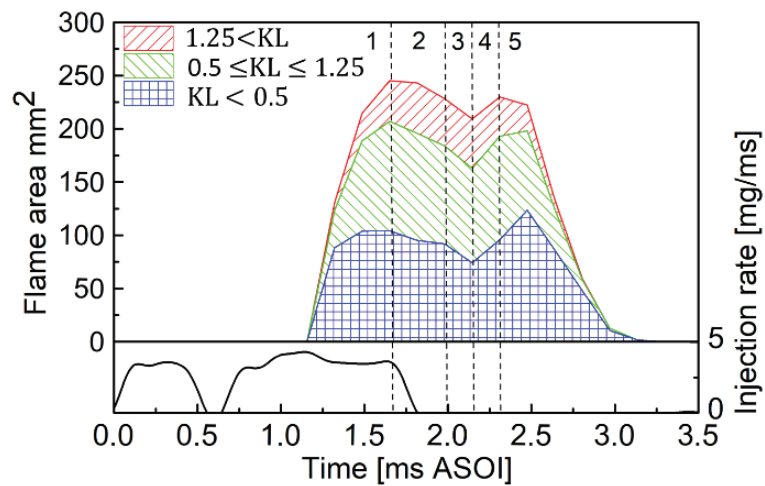
Fig. 4.12 KL factor against temperature map in the three regions i.e., flame tail, middle and tip at 2.2 ms (ASOI) for (a) split ratio 3:7, (b) split ratio 5:5, and (c) split ratio 7:3.

Figs. 4.13–4.15 show the relationship between the flame area temperature and KL factor distributions ASOI under the 3:7, 5:5, and 7:3 split ratios, respectively. This also provides an analysis of soot under the three injection strategies. The temporally resolved soot distribution could be separated into two steps, i.e., the soot formation step

and soot oxidation step [141]. The soot production could be determined by the KL value [142]; a large KL value at a particular instant corresponds to the highest soot production at that instant.

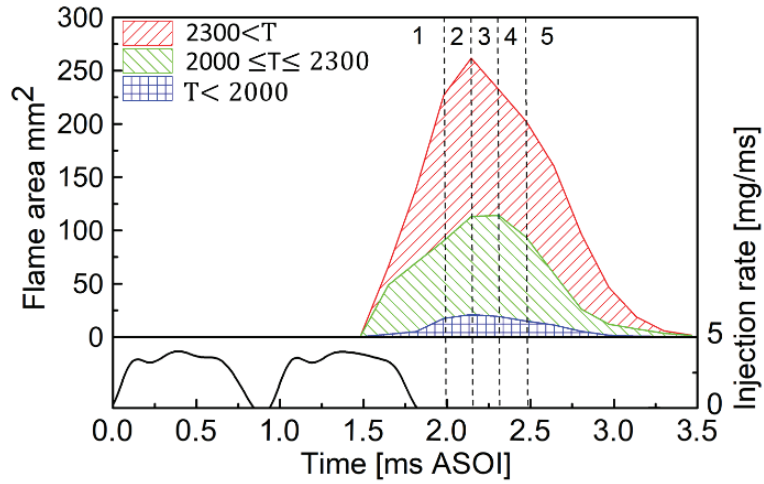


(a)

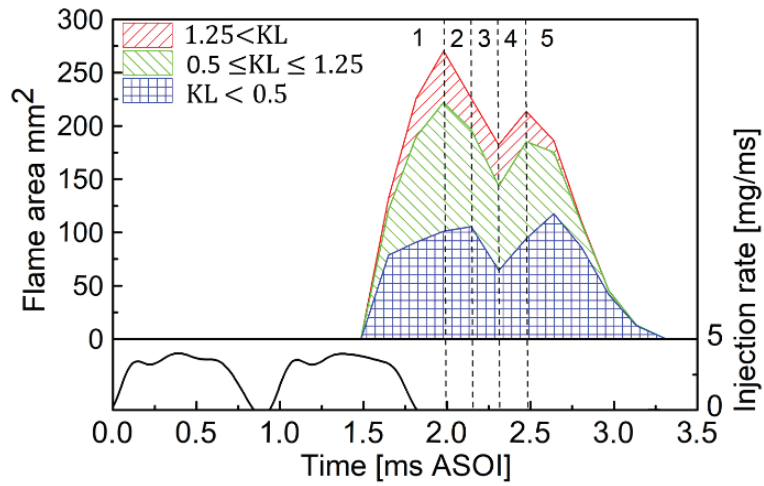


(b)

Fig. 4.13 Temporal comparison between the flame area (a) temperature and (b) KL factor for split ratio 3:7.

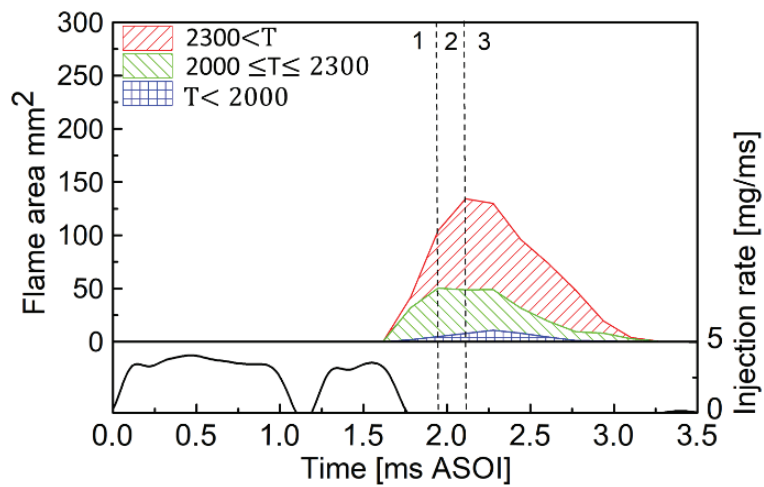


(a)

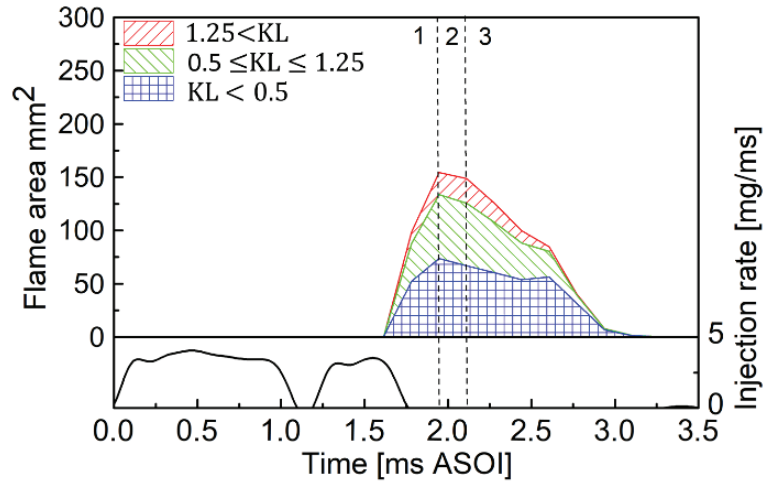


(b)

Fig. 4.14 Temporal comparison between the flame area (a) temperature and (b) KL factor for split ratio 5:5.



(a)



(b)

Fig. 4.15 Temporal comparison between the flame area (a) temperature and (b) KL factor for split ratio 7:3.

For the process of soot formation, the local equivalence ratio is an important factor for the soot improvement to be made in fuel-rich premix regions [143 144]. The period of soot oxidation, total temperature, and mixing capacity are the significant factors, and a parameter was also set for the study of the mixing capacity [145]. However, the net soot propagation was resolved by adjusting the soot formation and soot oxidation after combustion. The values of the temperature and KL factor for each chart at a certain time could be realised by calculating the pixel numbers. However, the flame areas of temperature and KL distribution are categorised statistically at a particular instant in time based on the number of pixels. In this study, the low, medium, and high-temperature areas are defined in Fig. 4.15 (a) by the range of $T < 2000$, $2000 \leq T \leq 2300$, and $2300 < T$, respectively. Similarly, the ranges for the low, medium, and high KL factor areas, for every split ratio, are defined in Fig. 4.15 (b) by the range of $KL < 0.5$, $0.5 \leq KL \leq 1.25$, and $1.25 < KL$, respectively. The Fig. 4.15 shows that the high-temperature area in each split ratio was much higher than the low and medium-temperature areas in the temperature index. With regard to the distribution of the KL factor area, the low KL factor area was comparatively greater than the high and medium KL factor areas. Fig. 4.13 illustrates the relationship between the flame area of temperature and KL factor under the 3:7 split ratio, and this could be split into five steps. The first step shows that the temperature area and KL factor area increase owing to the initial combustion. The second step shows the period of soot oxidation as the temperature zone increases and the KL factor area decreases. In the third step, the

temperature zone decreases as the KL factor area decreases, and the fourth step begins. The fourth step is the period of maximum soot formation because the combustion of the second injection fuel causes the creation of fresh soot. The high KL factor area decreases with the temperature in the fifth step, due to the end of combustion, while the low and medium KL factor areas increase marginally. Fig. 4.14 shows the relationship between the flame area of temperature and the KL factor ASOI under the 5:5 split ratio. This is also split into five steps, similar to what was done for the 3:7 split ratio. The first step is similar to that for the 3:7 split ratio due to the initial combustion. The second step is the period of soot oxidation, which is the same as that for the 3:7 split ratio. The third step is also identical to that of the 3.7 split ratio. The second injection fuel is then ignited, and in the fourth step, new soot is produced. In this step, the second injection fuel catches up to the previous flame, as discussed for the 3:7 split ratio. Therefore, a large amount of soot is produced in the region around the tip of the flames. Therefore, the KL factor region in this step increases. However, the fifth stage is slightly different from the 3:7 split ratio because when combustion ends, only the low KL area increases marginally. Fig. 4.15 shows the relationship between the flame area of temperature and the KL factor of the 3:7 split ratio. This can be split into three steps, which vary from those for the 3:7 and 5:5 split ratios. The first step is similar to that for the 3:7 and 5:5 split ratios owing to the initial combustion. The second step is the process of soot oxidation and is the same as that for the 3:7 and 5:5 split ratios. However, the soot formation process is negligible because the lower fuel quantity of the second injection mixes with the ambient gas, nitrogen in this case, and provides better air entrainment inside the combustion chamber. In the last step, the combustion ends, similar to that for the 3:7 and 5:5 split ratios.

According to Kamimoto et al. [146], the equation for the KL factor can be obtained by applying the Rayleigh–Debye–Gans model, as follows:

$$KL = \frac{6\pi E(m)c_m}{\rho_p} L \quad (4.2)$$

Here, $E(m)$ is expressed as

$$E(m) = \text{Im} \left(\frac{m^2 - 1}{m^2 + 2} \right) \quad (4.3)$$

where ρ_p denotes the density of the elementary particles, L the geometric thickness including its spray flame along the optical detection axis, c_m the soot mass concentration, and m the soot particles' complex reflection index, expressed as $m =$

$n - ik = (2.0 \pm 0.1) - i(0.55 \pm 0.10)$. In this study, we selected $n = 2.0$ and $k = 0.55$.

The mass of soot (m_s) can be obtained as follows:

$$m_s = \Delta a_{pix} \frac{\rho_p}{6\pi E(m)} \sum KL \quad (4.4)$$

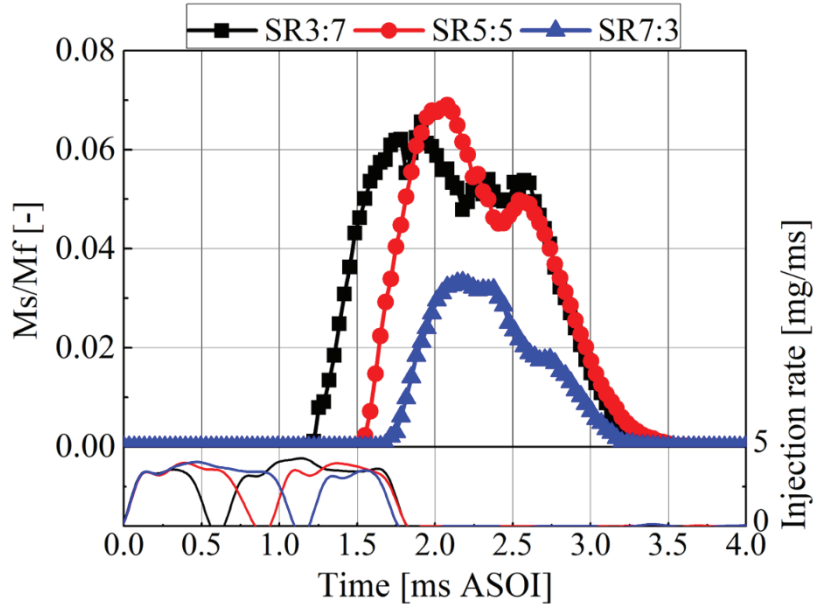


Fig. 4.16 Ratio of soot mass to fuel mass.

The time-dependent ratio of soot mass to injected mass is depicted in Fig. 4.16. The soot mass ratio was divided into two sections: the SOI to EOI section, where the injected amount fluctuated over time, the other section was the EOI, where the injected amount stayed constant. However, based on Eq. (4.4), the soot mass and integrated KL factor are correlated [147]. The ratio of soot mass to fuel mass should have the same shape as the integrated KL factor if the injection amounts are comparable. This concept can be compared to the results in Fig. 4.10. For each split ratio condition, the highest ratio matched the highest integrated KL factor. For 7:3 split ratio case, the highest integrated KL factor occurred after the end of injection, where the injected amount was stable. The gradient of the mass ratio for the 7:3 split ratio case from the SOI to EOI was lower than the other cases. This implies that the 7:3 split ratio case yielded a low amount of soot. Fig. 4.17 shows the soot index for the combustion. The paths in the curve represent the soot mass slope. The slopes of the two surrounding time points are defined in the curve. A curve greater than zero

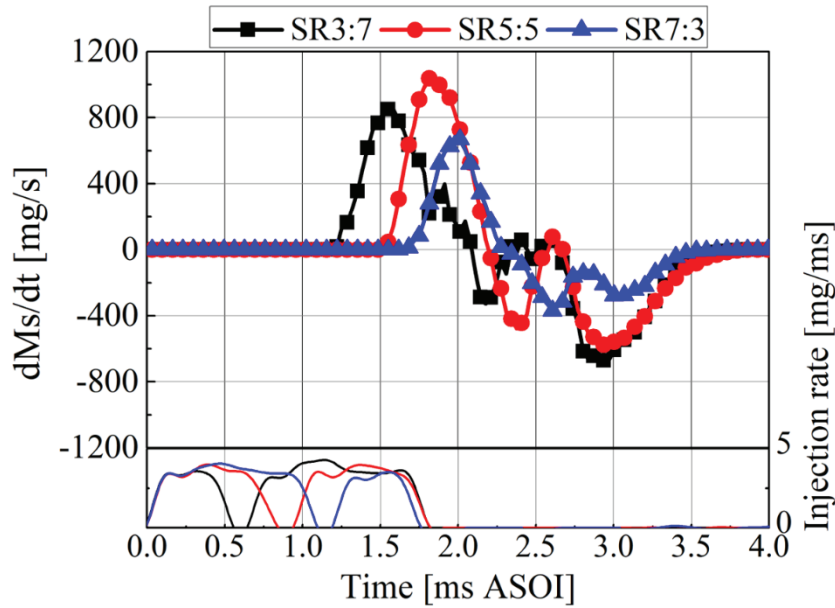


Fig. 4.17 Soot index for combustion.

indicates ‘during the soot-formation-dominated process’, whereas those lower than zero indicate ‘during the soot-oxidation-dominated process’. The soot index of the 3:7 split ratio case is primarily categorised into six phases: 1.15 ms to 2.1 ms ASOI; 2.1 ms to 2.32 ms ASOI; 2.32 ms to 2.37 ms ASOI; 2.37 ms to 2.47 ms ASOI; 2.47 ms to 2.63 ms ASOI and 2.63 ms to EOI. 5:5 split ratio is primarily categorised into four phases: 1.48 ms to 2.2 ms ASOI; 2.2 ms to 2.57 ms ASOI; 2.57 ms to 2.7 ms ASOI and 2.7 ms to EOI. However, 7:3 split ratio is primarily categorised into two phases: 1.61 ms ASOI to 1.3 ms ASOI and 1.3 ms ASOI to EOI. Split ratio of 3:7 represents soot formation, oxidation, formation, oxidation, formation, and oxidation processes. Split ratio of 5:5 exhibits soot formation, oxidation, formation, and oxidation processes. On the other hand, split ratio of 7:3 has soot formation as well as oxidation dominated processes. The duration of the soot evaluation period varies because of the varied mass ratio. Nevertheless, the ratio of the 7:3 split ratio case was lower than that of the other cases during the ignition period. In the 7:3 split ratio case, soot formation reduced during the preliminary combustion. Furthermore, the gradient of the ratio for the 7:3 split ratio case was smaller than those of the other cases during the soot oxidation period, which is consistent with the results shown in Fig. 4.10. This implies that small amount of soot was oxidised during the combustion time in the 7:3 split ratio case.

4.4 EFFECT OF DWELL TIME

4.4.1 Injection Conditions and Injection Rate

Table 4.2 Single and split injection conditions

Split ratio	1 st injection Quantity [mg]	2 nd injection Quantity [mg]	SOI1 [ms ASOI]	EOI1 [ms ASOI]	Injection dwell [ms]	SOI2 [ms ASOI]	EOI2 [ms ASOI]
10:0	5	0	0	1.5	(Single injection)		
7:3	3.5	1.5	0	1.1	0.12	1.22	1.77
7:3	3.5	1.5	0	1.1	0.32	1.42	2.02
7:3	3.5	1.5	0	1.1	0.54	1.64	2.22

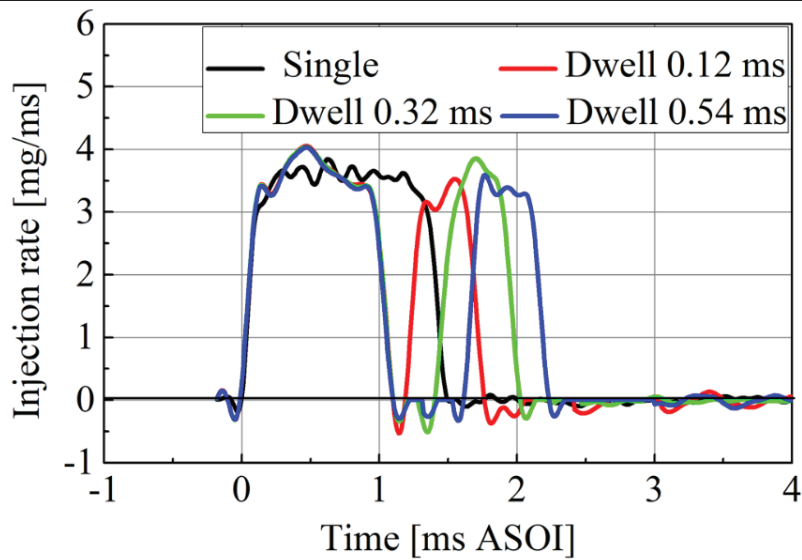


Fig. 4.18 Temporal variation in injection rate for various dwell times.

Table 4.2 shows the injection conditions used to investigate the effects of various dwell times between injections. The split ratio ‘10:0’ indicates that a single injection injected 100% of the fuel mass. Split ratio ‘7:3’ implies a split injection, with 70% of the overall fuel amount injected during the first injection and 30% in the second injection. The injection rates are shown in Fig.4.18. The Zeuch method was used to measure the injection rate. The pressure of the chamber and the mass flow rate were the main parameters of this method. When fuel was injected into the chamber, the fuel mass increased, allowing the chamber pressure to increase [136]. As mentioned previously, a seven-hole injector with a 0.123 mm hole diameter was used to determine the injection rate; the total amount of injected fuel mass was 5 mg per hole, and the backpressure

was 2 MPa. The total amounts of tracer LAS and diesel fuel were identical. The second injection rate profiles differed slightly depending on the dwell times. It was speculated that this was due to the high-pressure tube and the oscillation of the injector pressure within the injector. In the current method, oscillations in the injector pressure were inevitable because during injection, a series of recharging and pressure release occurred. Nevertheless, to maintain a constant total volume of the injected fuel mass, the injection duration was adjusted slightly for every dwell time case. For various dwell time conditions, the injection duration (= EOI2-SOI1, where EOI and SOI represent the end of injection and start of injection, respectively) varied, as shown in Table 4.2. However, the process of mixture formation at different dwell times will be discussed and compared comprehensively based on the EOI2 timings in the next section.

4.4.2 Spray Mixture Concentration Distribution

Fig. 4.19 shows the equivalence ratio distributions of the liquid and vapor phases of single- and split-injection sprays for various dwell times. The image achievement times were as follows: EOI (EOI2 for the split injection) and 0.15 ms AEOI (after the end of the injection) from the left to right of each injection strategy to demonstrate the spray characteristics. In each image pair, the liquid- and vapor-phase spray are on the left and right sides, respectively. In addition, for all conditions, the maximum liquid- and vapor-phase equivalence ratios were 4 and 3, respectively. For the single injection, the mixture formation was leaner after the end of injection, as shown in Fig. 4.19 (a) because the injection event ended sooner compared with the split injection. However, the positive effects of the split injection with 0.12 ms dwell time were observed when aligned with the EOI time domain, as shown in Fig. 4.19 (b). In terms of homogeneity, the mixture distribution was better in the split injection with a dwell of 0.12 ms compared with those of other dwell time cases, for the same EOI timing. The wave of air entrainment generated by the first injection produced a lean region promptly at the tip of the nozzle [14]. In addition, the mass of the second injection was positioned around the tip, where the first injected fuel was leaned. The small injection amount of the second injection (compared to the first injection) promoted a leaner mixture formation of fuel without creating a rich region, as in the first injection; this finding is similar to the result reported in [148].

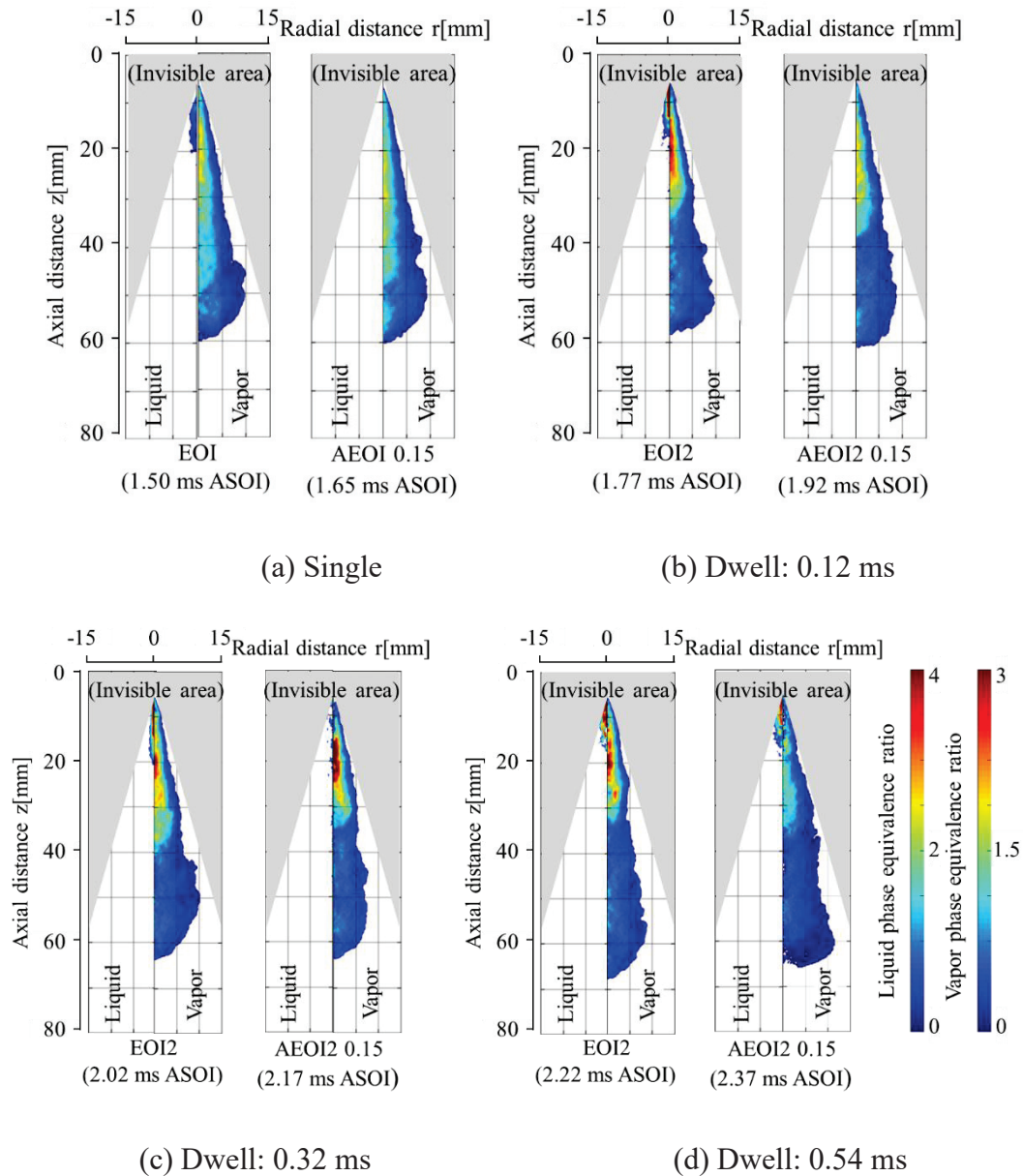
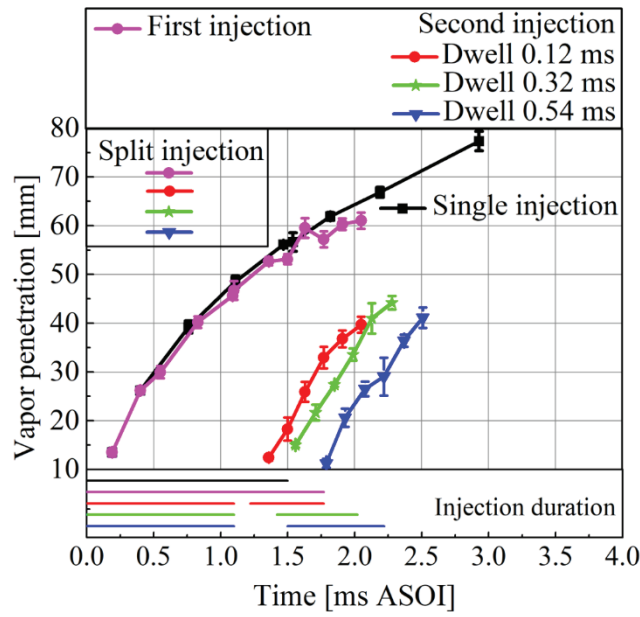
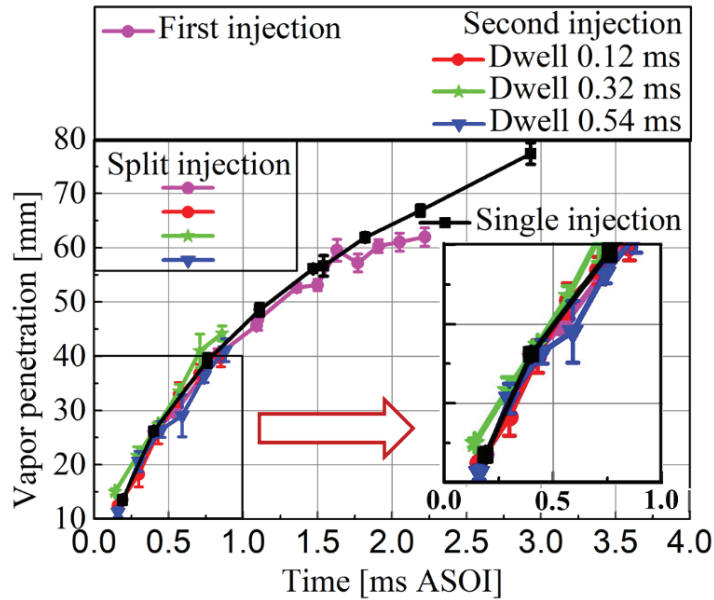


Fig. 4.19 Temporal evolution of distributions of liquid and vapor phase equivalence ratios at EOI (EOI2) and AEOI 0.15 ms.

The mixture formation under a dwell time of 0.32 ms indicated a slight difference compared with those of other dwell times at 0.15 ms AEOI. A more concentrated area of the rich mixture was observed in the 0.32 ms dwell time case. Moreover, the liquid phase could still be seen at EOI2+0.15 ms for the 0.54 dwell case, which supports the claim that mixture formation slows down at longer dwell times.



(a)



(b)

Fig. 4.20 Vapor penetration positions.

Fig. 4.20 shows the vapor penetration of single and split injections for different dwell time cases. The vapor penetration can be determined based on the optical thickness of the UV image and by detecting the spray boundary. Fig. 4.20 (a) shows the original vapor penetration positions of the first and second injections. At EOI1, the vapor penetration of the first injection of the split injection was shorter than that of the single injection because the injection amount of the former injection was smaller than that of the single injection. The vapor penetration of the second injection can be determined from the image because the richer mixture yielded a distinct boundary from

the first injection. Identical to the first injection, the second injection penetration shifted, synchronised, and enlarged with the time domain, as shown in Fig. 4.20 (b). The first injection affected the penetration of the second injection, and the results varied depending on the dwell time. In the 0.32 ms dwell time case, the vapor penetration of the second injection was comparatively higher than that of the first injection owing to the slipstream [84]. By contrast, in the 0.54 ms dwell time case, the penetration of the second injection vapor was the lowest. Hence, the effect of the first injection on the vapor penetration of the second injection is negligible for a long dwell duration. The evaporation ratio is closely related to the vapor mass. The vapor mass calculated by applying the onion-peeling method to the spray image. The accuracy of the experiment was checked by evaluating the total vapor mass at fully evaporated timing [149].

Fig. 4.21 shows the temporal changes in the evaporation ratio for the single and split injections for different dwell time cases. Image analysis was used to calculate the vapor mass, and the integral of the injection rate profile was used to calculate the total injected fuel mass.

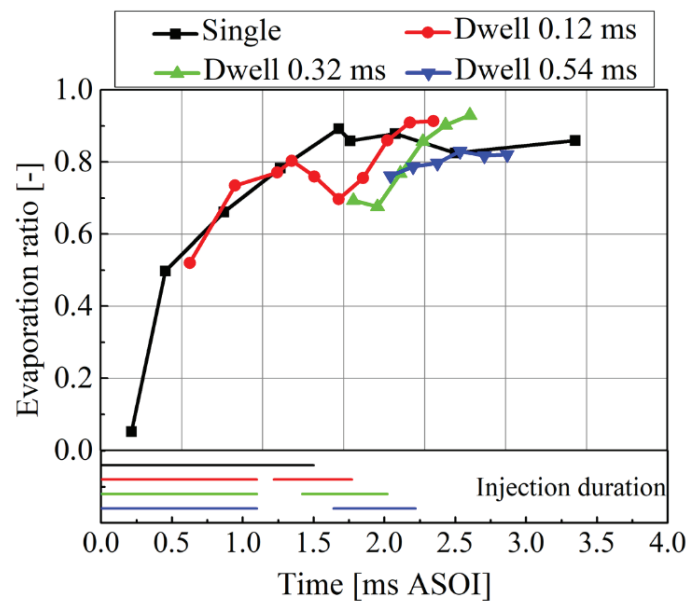


Fig. 4.21 Evaporation ratio.

The evaporation ratio of the first split injection was comparable to that of the single injection. However, the second injection fuel evaporation ratios for dwell times of 0.12 and 0.32 ms were higher than those of the remaining case. The shortest duration of the injection rate measurement is expected to induce more potent air entrainment and a faster liquid recession after EOI2 [150]. In the 0.54 ms dwell time case, a delayed

injection owing to a long dwell time resulted in an insufficiently hot temperature for evaporating the remaining fuel; as a consequence, the combustion within the chamber was slowed down.

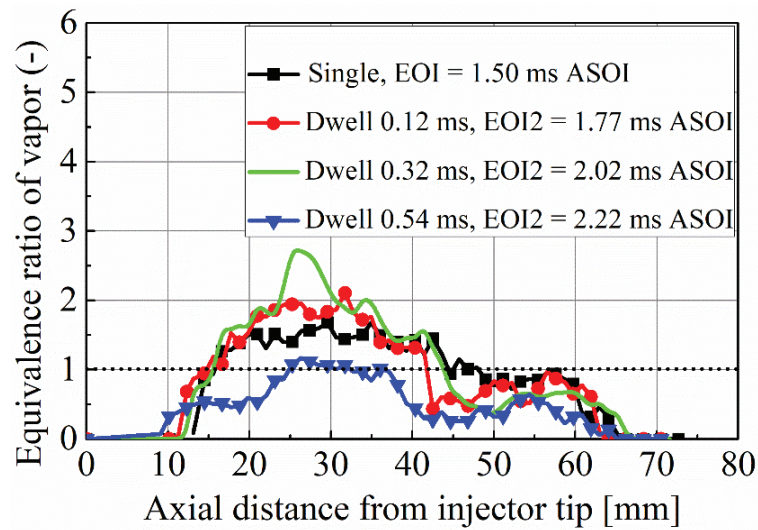


Fig. 4.22 Distributions of equivalence ratios along spray axis.

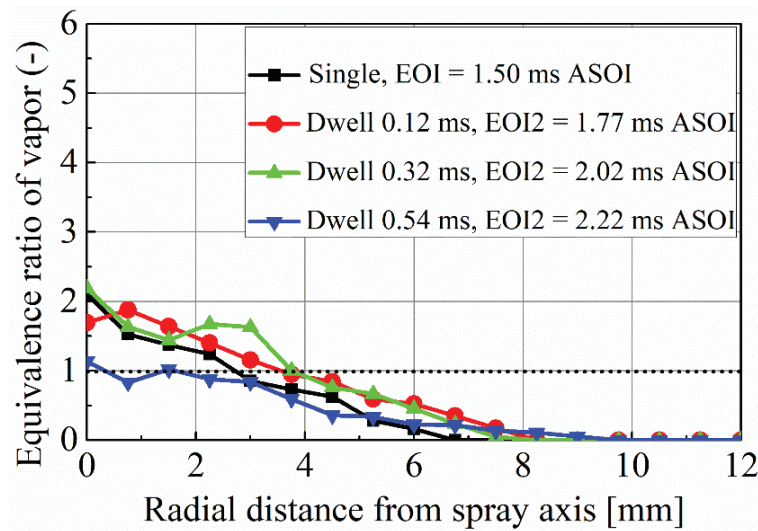


Fig. 4.23 Distributions of equivalence ratios along radial direction ($Z = 40$ mm).

Figs. 4.22 and 4.23 show the effects of various dwell times on the distributions of the equivalence ratios in the direction of the spray axis (the graph of the equivalence ratio distribution in the axial direction shows that the average equivalence ratio is maintained at every 2 mm for the measurement accuracy) and in the radial direction 40 mm downstream of the nozzle tip after the end of injection. The dotted line partitions the mixture distribution region into two regions: the lean mixture region where the equivalence ratio is less than 1, and the rich mixture region where the equivalence ratio

is greater than 1. As shown in Fig. 4.22, a comparatively rich mixture appeared in the upstream region. However, the mixture became richer in the 0.32 ms dwell time case. In this case, the penetration of the second injection was comparatively longer, and the weaker air entrainment between the dwell durations may have contributed primarily to the richer mixture. However, a comparative lean mixture appeared in the downstream region. As shown in Fig. 4.23, the radial distribution of the equivalence ratio decreased gradually from the rich mixture region to the lean mixture region under all conditions. It was observed that the equivalence ratio distribution decreased more uniformly in the 0.12 ms dwell time case. A suitable position for the second injection around the boundaries of the first injection accomplished in the shorter dwell time case is attributable to the smooth growth of the lean mixture and avoidance of the rich mixture's large zone. Meanwhile, in Figs. 4.22 and 4.23, it can be seen that the longest dwell time results in overall leaner mixtures. One of the possible reasons behind that the first injection had more time to spread and mix with air at the time that the image is recorded. Further, in Fig 4.23, the mixture is leaner near the axis, but there is more fuel away from it. This implies that the first injection fuel has spread more.

Fig. 4.24 shows the vapor mass distribution vs. equivalence ratio for single and split injections at different AEOI dwell times. Although the vapor mass peak value fluctuated in the single injection case, it decreased gradually from the peak for the split injection. However, in the lower equivalent ratio peak region (i.e. below 1.0), it increased primarily from the first injection and shifted towards the leaner edge with increasing dwell time. The longer dwell time offered more time for the lean mixture to settle at the nozzle tip, where the second injection occurred. At a lower dwell time of 0.12 ms, the vapor mass peak occurred at the equivalence ratio of approximately 1.5. However, after combustion, the net soot generation was determined by the soot formation and oxidation balance. In the absence of combustion, it is difficult to derive a valid conclusion for the ideal dwell time case. Furthermore, the longer dwell time case would result in a relatively lean mixture for most fuels with an equivalence ratio of less than 0.5, thereby resulting in a low combustion efficiency and hence an insufficient supply of hot gas for soot reduction as well as unburned hydrocarbon emissions [151].

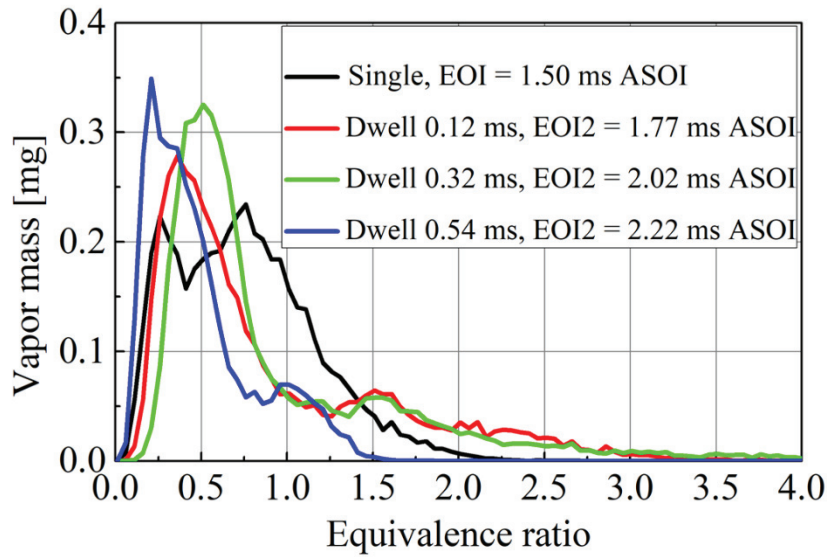


Fig. 4.24 PDF of vapor phase equivalence ratio.

Significant deviations from a constant-volume combustion can reduce the engine efficiency [152]. Therefore, a dwell time of 0.12 ms is suitable if the overall distribution of the equivalence ratio is to be considered. However, under the reaction conditions, the optimal dwell time corresponding to soot formation and oxidation should be investigated.

4.4.3 Spray Combustion Characteristics

The results of the combustion process investigation in the same conditions as those analysed for mixture formation are presented in this section. An overview of the ignition delay (luminous flame ignition) of both single and split injections at different dwell times is shown in Fig. 4.25. The blue, green, and white patterns indicate the durations of the first and second injections, and the dwell time, respectively, whereas the solid red circles represent ignition. The ignition delay is defined as the time from the beginning of the injection to the first luminous flame (diffusion flame). As shown in Fig. 4.25, a luminous flame was observed during the second injection of the split injection. Because the first injection was also ignited during the split period, it was burning in blue flames, which were invisible. However, comparing the results between the dwell times of the split injection, it was observed that the ignition delay was longer in the 0.54 ms dwell time case owing to the thin air involved. Moreover, the ignition delay of the second injection was diminished in the 0.12 ms dwell time case. The reduced dwell time can improve the hot-air fuel mixture, thereby promoting the ignition of the second injection and reducing the ignition delay.

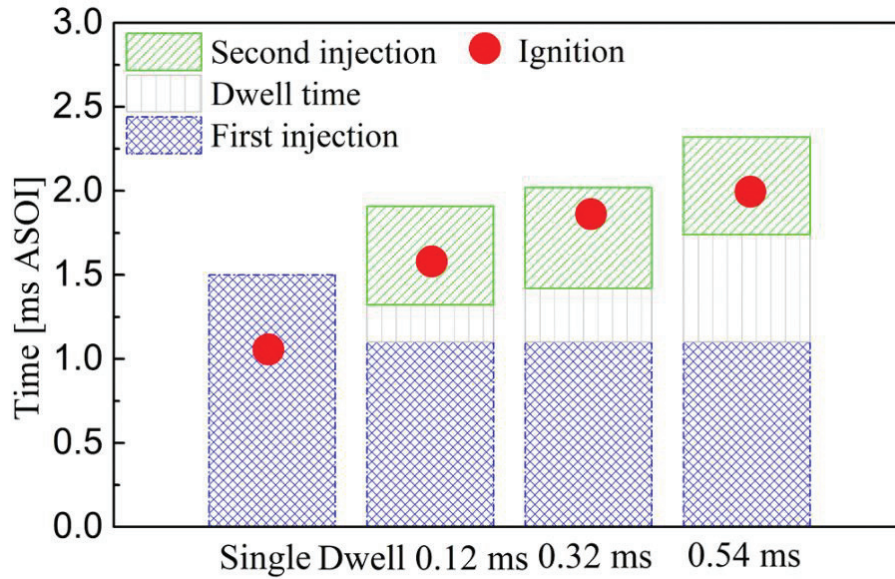


Fig. 4.25 Time from SOI to first luminous flame appearance for all conditions investigated.

Fig. 4.26 shows the distributions of the KL factor (where K is the absorption coefficient which is proportional to density of the soot particle and L is the geometric thickness of the spray flame along the optical detection axis) and flame temperature achieved by processing the images captured via the high-speed video camera using two-colour pyrometry. The flame temperature obtained was the soot temperature. Three output sets were used for each injection strategy. However, only one set of outcomes for each injection condition is shown. In Fig. 4.26, the images in the upper row exhibit the KL factor for each injection strategy, whereas those in the lower row represent the flame temperature. The image display timings were from the first luminous flame appearance, after the end (EOI2 for split injection) of injection (AEOI), and after 2.5 ms of injection (ASOI) for a single and split injection of various dwell times. The maximum KL factors were near the flame tip regions. The KL factors of the single injection case were significantly higher than those of the split injection case. This implies that split injection decreased the amount of soot. Meanwhile, the high temperature in the midstream region of the sooting flame persisted at the EOI for every injection strategy because of soot oxidation [153], which is a heat-releasing process. However, for the 0.12 ms dwell time case, the fuel of the second injection passed through only the nozzle tip of the first injection at EOI2.

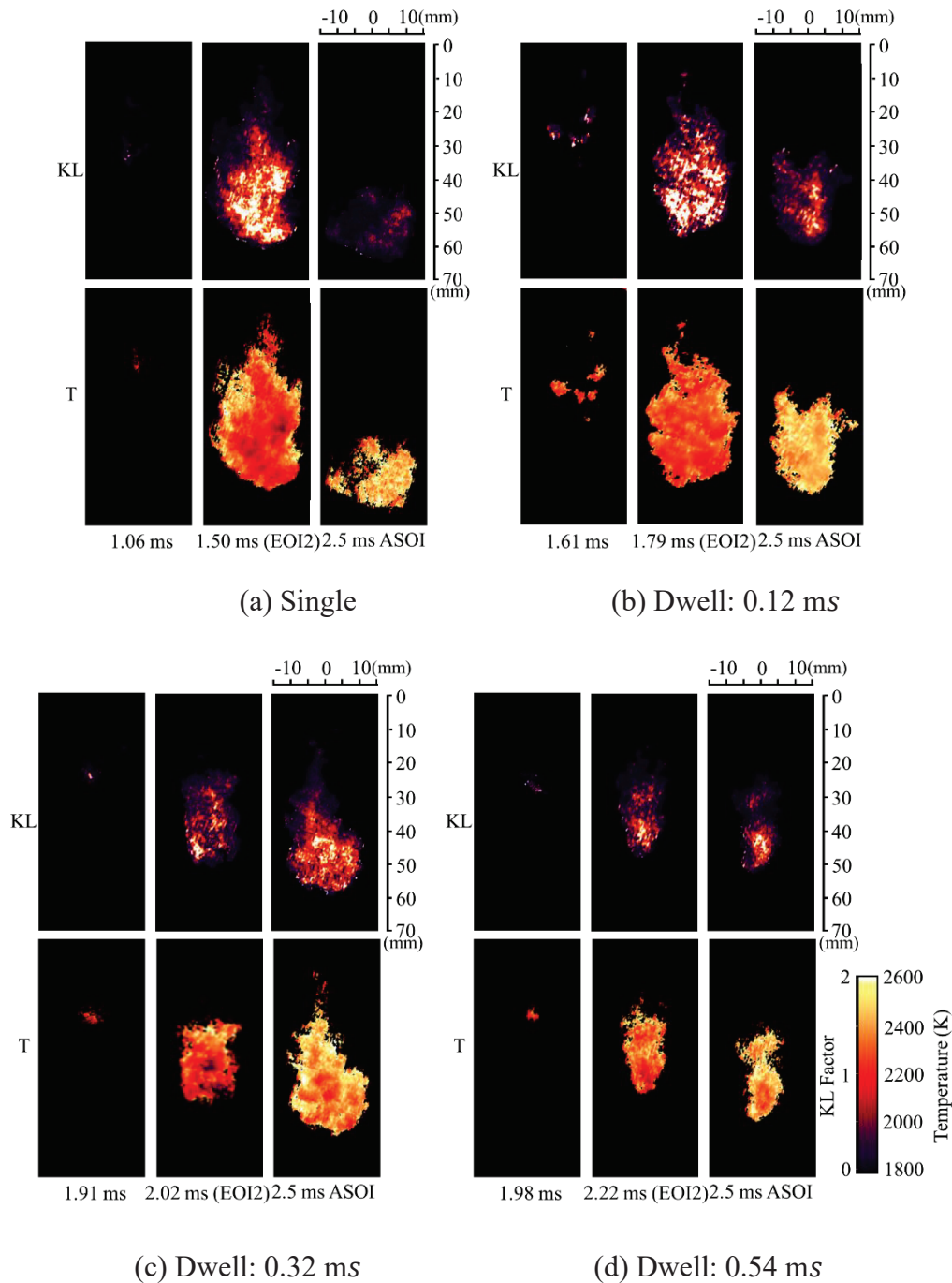


Fig. 4.26 Colour images of flame temperature and KL factor distributions.

This flame illustration implies that the deterioration did not affect the previous flame and did not result in a higher KL factor distribution in the vicinity of the flame tip location, as shown in Fig. 4.26 (b), similar to the result reported in [139]. By contrast, in the 0.54 ms dwell time case, the KL factor allocation and flame temperature were weaker and lower for every timing, respectively, as illustrated in Fig. 4.26 (d). The longer dwell time provided insufficient high temperature burning gases from the combustion of the first injection to that of the second injection.

The integrated KL factor after the start of ignition (ASOI) for single and split injections with different dwell times is shown in Fig.4.27. The integrated KL factor of the split injection was lower, indicating that split injection can decrease instantaneous soot amounts at a specific time during the combustion event.

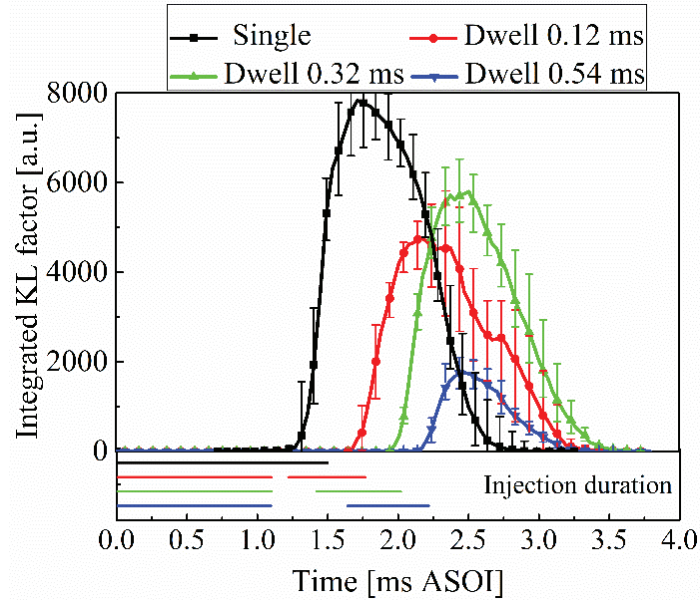


Fig. 4.27 Integrated KL factor.

However, the integrated KL factor for the 0.32 ms dwell time case was higher than those of the other dwell time cases. This is attributable to the higher equivalence ratio along the axial and radial distributions after the end of the injection. In fact, this was observed in the spray evaporation experiment. In addition, the integrated KL factor gradient of the 0.12 ms dwell time case from the peak point to the last edge of the integrated KL factor was lower than those of the other cases, which is contrary to the results of [154], wherein similar gradients were reported to be lower for the single injection. The single injection and 0.32 ms dwell time case indicated the maximum integrated KL factor, which decreased rapidly subsequently; this implies that the single injection and 0.32 ms dwell time case decreased the amount of soot rapidly. Therefore, 0.12 ms can be regarded as the optimal dwell time owing to the combustion efficiency and smooth soot emissions afforded. The average flame temperature ASOI for the single and split injections at different dwell cases are shown in Fig. 4.28. As shown, the shape of the average flame temperature of the single injection curve is similar to that of the split injection curve. Compared with the dwell time cases during the combustion period, the maximum average flame temperature was observed in the 0.54 ms dwell time case; this is because when the luminous flame

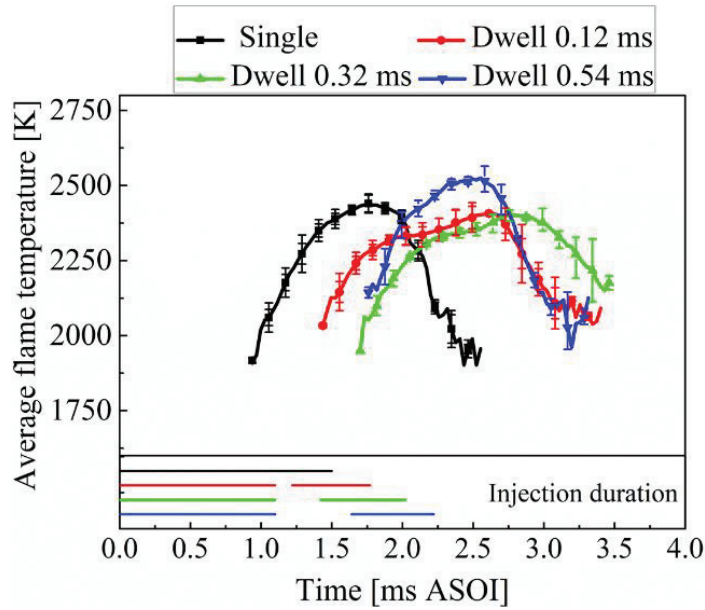


Fig. 4.28 Average temperature of spray flame.

cannot be observed clearly and the temperature information is insufficient, a higher average temperature than those of other cases may be obtained. Meanwhile, for the 0.12 and 0.32 ms dwell time cases, high soot production with low-temperature regions was captured on the images. Hence, the overall average temperature might be lower for these cases.

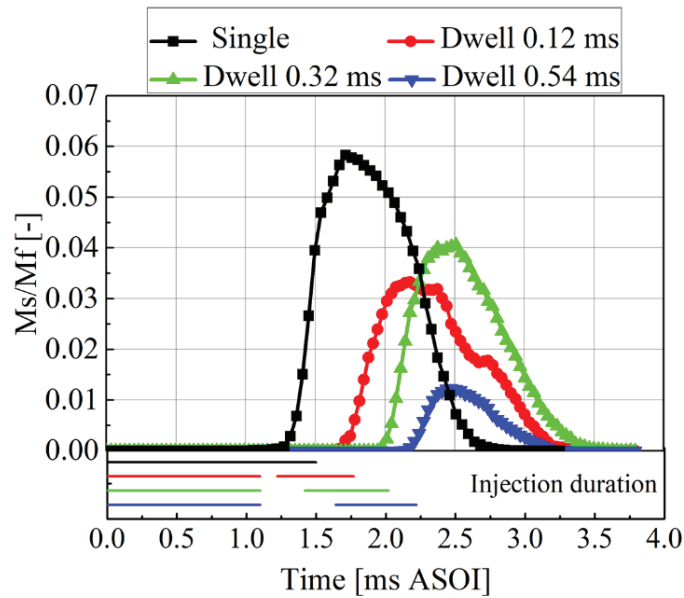


Fig. 4.29 Ratio of soot mass to fuel mass.

Fig. 4.29 shows the time-dependent ratio of soot mass to injected mass. The soot mass ratio was separated into two sections: one section was from the SOI to EOI, where the injected quantity shifted with time; the other section was after the EOI, where the

injected amount remained unchanged. However, based on Eq. (4.4), the soot mass and integrated KL factor are inter-related [147]. If the injected amounts are alike, then the shape of the ratio of soot mass to fuel mass should be the same as that of the integrated KL factor. This hypothesis is comparable to the results shown in Fig. 4.27. The highest ratio corresponded to the highest integrated KL factor for every injection strategy. The highest integrated KL factor occurred after the end of injection, where the injected amount was stable. The gradient of the mass ratio for the single injection from the SOI to EOI was higher than that of the split injection. This implies that the single injection yielded a significant amount of soot rapidly. However, the gradient of the mass ratio in the 0.32 ms dwell time case from the SOI to EOI was higher than those of the other dwell time cases. This suggests that the soot formation ratio of the 0.32 ms dwell time case was higher than those of the other dwell time cases. Fig. 4.30 shows the soot index for the combustion. The paths in the figure represent the soot mass slope. The slopes of the two surrounding time points are defined in the curve. A curve greater than zero indicates ‘during the soot-formation-dominated process’, whereas those lower than zero indicate ‘during the soot-oxidation-dominated process’.

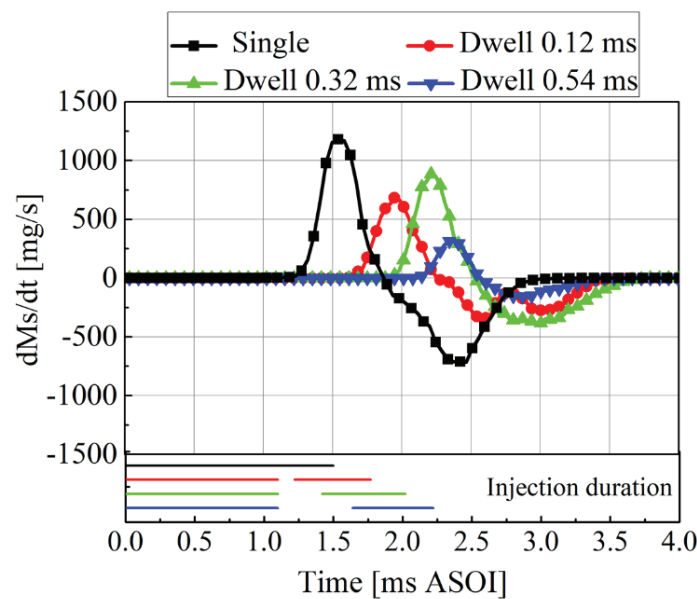


Fig. 4.30 Soot index for combustion.

The soot index of the single injection is primarily categorised into two phases: 1.06 ms ASOI to 1.7 ms ASOI, which is the duration of the soot-formation-dominated process; and 1.7 ms ASOI to 3.2 ms (EOI), which is the duration of the soot-oxidation-dominated process. A similar phenomenon was observed for split injection.

Nevertheless, owing to the different injection durations at various dwell times, the soot evaluation period exhibited various continuations. For the 0.54 ms dwell time case, the combustion efficiency was low when the soot formation and oxidation durations were low, as discussed previously. However, the ratio of the 0.12 ms dwell time case was lower than that of the single injection and 0.32 ms dwell time case during the ignition period. In the 0.12 ms dwell time case, soot formation reduced during the preliminary combustion. Furthermore, the gradient of the ratio for the 0.12 ms dwell time case was smaller than those of the other cases during the soot oxidation period, which is consistent with the results shown in Fig. 4.27. This implies that soot was oxidised smoothly at the combustion time in the 0.12 ms dwell time case.

4.5 SUMMARY

An experimental study was conducted to investigate the mixture formation and combustion characteristics of a split-injection diesel spray. Two different diagnostic techniques were used. LAS was employed to determine the mixture concentration of the spray, and the two-color pyrometer method was used to analyse the combustion flame structure. To overcome any differences in the spray structure from a single-hole injector, a commercial seven-hole injector was selected. To observe the effect of the split ratio and the dwell time on mixture formation and combustion, three split ratios, i.e., 3:7, 5:5, and 7:3, were selected whereas, three dwell times, i.e. 0.12, 0.32, and 0.54 ms, were chosen.

The main conclusions are summarised as follows:

Split ratio effect

1. The evaporation ratio of the first two injection setups was evidently higher than that for the third split ratio owing to the lower amount of fuel quantity in the first injection. Moreover, the 3:7 split ratio resulted in a wider “over rich” mixture inside the spray. This is because the vapor of the second spray merged with the vapor of the first spray and resulted in a compact structure, which consequently turned into the “over rich” mixture.
2. Considering the three split ratios, it could be concluded that 7:3 is the best for mixture formation in the present study. The ambient air and fuel mixture made from the first injection is applied to the spray of the second injection; accordingly, the leaner mixture made from the first injection is in a convenient place. After the first injection is completed, the air inlet wave rapidly shapes the nozzle flow mixture. Furthermore, this

split ratio provides the right amount of fuel for exploring the lean area in the first injection fuel mixture. Thus, compared with the other two split ratios, an overall leaner structure is formed.

3. The 7:3 split ratio has shown a positive effect on the soot reduction of KL against the flame temperature. All three split ratios showed that the high temperature range was considerably higher, and the low KL factor area was greater for the flame area of temperature and KL factor distributions.

4. The soot formation process for the 3:7 and 5:5 split ratios was investigated. The first injection fuel blends with the greater amount of the second injection fuel to create a fuel pile; this deteriorates the combustion region and influences soot formation. For the 7:3 split ratio, the interaction of the burned gas with the ambient gas inside the combustion chamber during the injection pause time promoted combustion and reduced soot formation.

Dwell time effect

1. In the 0.32 ms dwell time case, the vapor penetration of the second injection was comparatively higher than that of the first injection owing to the slipstream effect. However, the mixture became rich in the 0.32 ms dwell time case. With the extended penetration of the second injection, the weaker air entrainment between the dwell durations might have resulted in the rich mixture.

2. In the 0.12 ms dwell time case, the equivalence ratio distribution decreased uniformly from the rich mixture region to the lean mixture region. The shorter dwell time case yielded a suitable position for the second injection around the boundaries of the first injection by smoothly growing the lean mixture and avoiding the rich mixture's large zone.

3. The KL factor of the single injection was significantly higher than that of the split injection. Furthermore, the single and 0.32 ms dwell case indicated the highest integrated KL factor, which decreased rapidly subsequently; this implied that the single injection and 0.32 ms case decreased the amount of soot rapidly.

4. At a short dwell time, the interaction between nitrogen gas and the combustible gas within the combustion cell during the injection pause promoted ignition and oxidised the soot smoothly.

CHAPTER 5 TEMPORAL DEVELOPMENT OF MIXTURE DISTRIBUTION OF FUEL SPRAY

5.1 INTRODUCTION

Fuel injection and the air-fuel mixture quality play a vital role in the diesel engines combustion performance. Direct injection (D.I.) diesel engines require a better understanding of the fuel injection process as well as liquid and vapor phase fuel concentration to improve engine efficiency, performance, and emissions. This is because, when the liquid fuel in the diesel engine is injected into the high-temperature and high-pressure atmosphere, the liquid fuel jet breaks up, the fuel evaporates as well as mixes with the ambient air [120,155].

The fundamental concept of the LAS technique is to understand the fuel concentration by attenuation of both visible as well as ultraviolet light. The intensity of visible light is only attenuated by the scattering of droplets, while that of ultraviolet light is attenuated by not only the scattering of droplets but also the absorption of vapors. The conventional LAS uses the ND: YAG pulse laser, CCD cameras and one shot for one spray [156-158], which takes time and effort. Moreover, temporal variation measurement of a single shot spray is not possible by the conventional LAS. To record the distribution of the whole vapor phase in an injection event and measure the liquid and vapor concentration inside the spray, a high-speed laser absorption scattering (HS-LAS) technique was developed applying continuous diode light source, high-speed video cameras, and image intensifier for UV light, which can provide the temporal variation of a single shot spray. Tracer LAS fuel was used for the fuel injection. The deconvolution named onion-peeling model, which is the most important algorithm for deducing the concentration distribution from the line-of-sight optical thickness, is not applicable. Therefore, as mentioned in our previous publication [57,138], the application of the UV-Vis LAS method to asymmetric evaporating fuel sprays was offered. Following those studies, the detailed measuring concept of this technique is reviewed in this work. A symmetric uncertainty analysis is performed, and the measurement precision is validated using a series of experiments on completely evaporated fuel spray. Finally, imaging results for non-axisymmetric diesel sprays are reported using the expanded LAS technique.

5.2 EXPERIMENTAL CONDITIONS

In the LAS technique, the commercial diesel fuel cannot be used because the UV absorption of most commercial diesel fuels is high (due to a high aromatic content), but difficult to predict and calibrate and may vary from different qualities and suppliers and even batch to batch. Therefore, the selected fuel needs to meet the physical properties of diesel fuel, and to have sufficient

Table 5.1 Experimental conditions.

Injection Condition	Value	
Fuel	Tracer LAS (97.5% n-tridecane, 2.5% α -MN)	
Injector type	Piezo type Denso G3P	
Number of holes	7	
Nozzle diameter [mm]	0.123	
Spray including angle [deg]	155	
Injection amount [mg/hole]	2.5, 5.0	
Injection pressure [MPa]	100	
Ambient Condition	Value	
Ambient gas	Nitrogen	
Temperature [K]	300	800
Pressure [MPa]	1.8	4.8
Density [kg/m ³]	20.2	

absorption complying with the Lambert-Beer's law. The Tracer LAS fuel with the composition of 97.5 % n-Tridecane and 2.5 % 1-MN fuel was therefore chosen for this study. Furthermore, the chamber was filled with pure nitrogen gas to create a vaporizing atmosphere for the diesel spray but avoid reaction. The ambient temperature and pressure were set at 800 K and 4.8 MPa, respectively, while the gas density was kept about 20.2 kg/m³. The fuel injection pressure of 100 MPa was achieved using a common rail system. A multi-hole injector with seven holes (whose diameter was 0.123 mm each) was used in this study. The injector was attached to a multi-hole adaptor, which was fixed at the chamber's top. The injector was controlled by an ECU (electronic control unit) and a delay pulse generator (Stanford Research system Model DG645)

was used to control the injection mass and injection timing. The experimental conditions are shown in Table 5.1

The main topic of this chapter is the effect of injection mass on the mixture formation process for evaporating diesel spray. Fig. 5.1 depicts the injection rates. Using an injection rate meter (Ono Sokki's co. Ltd, FJ-07000), the Zeuch method was used to measure the injection rate shape. The main principle of the Zeuch method is the mass flow rate and chamber pressure. As more fuel is injected into the chamber, the fuel mass increases, allowing the chamber pressure to rise [159].

As previously stated, the injection rate was determined using a seven-hole injector with a 0.123 mm hole diameter; the total amount of injected fuel mass was 2.5 mg and 5 mg per hole, respectively, and the backpressure was 2 MPa. It shows that the 5 mg case the injection rate can reach the stable and quasi constant value between 0.2 and 0.7 ms ASOI. However, the 2.5 mg case the injection rate cannot reach the quasi-steady constant stage. The maximum injection rate of both cases almost similar around 3.6 mg/ms. The injection rate of 2.5 mg case comes to the maximum value at around 0.5 ms ASOI, which is very close to the quasi-steady condition injection rate of 5 mg case. However, the characteristics of the shot-to-shot variation, mixture formation process and total vapor mass in the spray at different cases will be comprehensively compared and discuss based on the various injection timings in the following section.

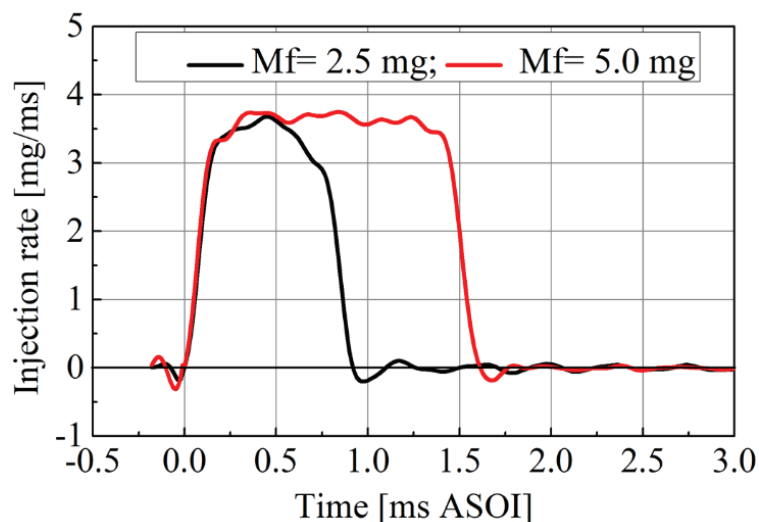
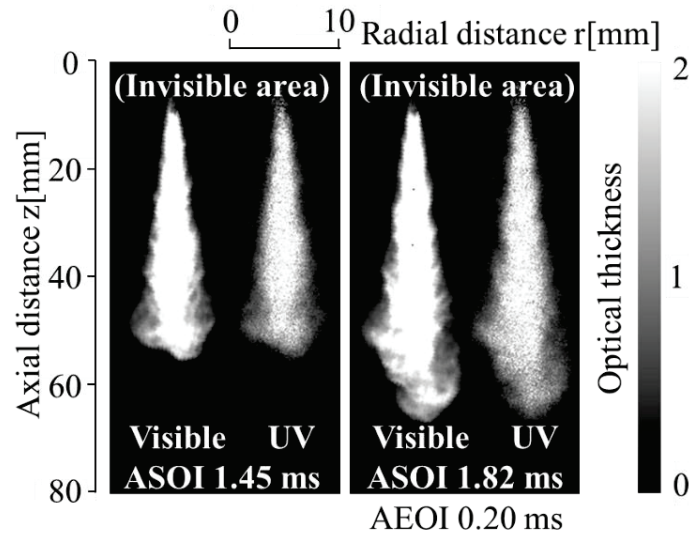


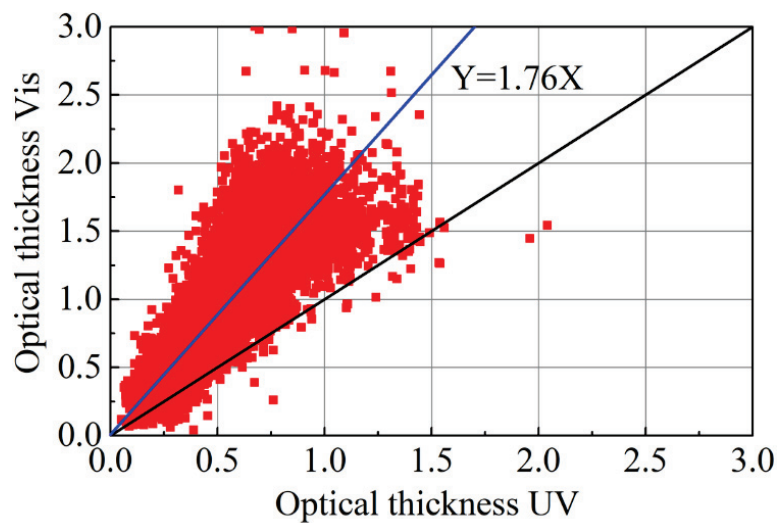
Fig. 5.1 Temporal variation of injection rate.

5.3 RESULT AND DISCUSSION

5.3.1 Comparison of UV and Vis Optical Thickness of Non-Evaporating Spray



(a) Non-evaporating spray optical thickness images



(b) Visible vs UV optical thickness

Fig. 5.2 Non evaporating spray image and line-of-sight optical thickness of UV vs visible light ($T_a=300$ K, $P_a=1.8$ MPa, $P_{inj}=100$ MPa, $M_f=5.0$ mg).

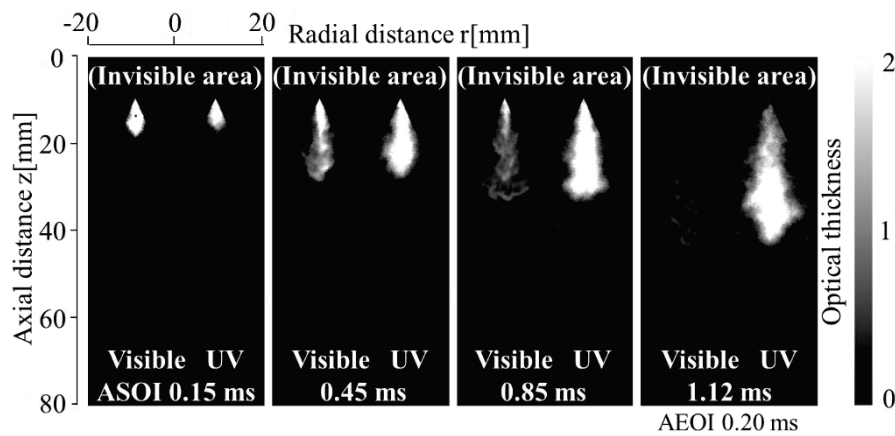
The line-of-sight optical thickness images of a non-evaporating spray injected into an environment of high pressure and room temperature are shown in Fig. 5.2 (a). For the non-evaporating experiment, the ambient density was selected to 20.2 kg/m^3 , which is like that of the evaporating condition. Images captured 1.45 ms ASOI and 0.20 ms

AEOI (=1.82 ms ASOI) are displayed to show representative sprays during and after the end of injection. In both pairs of images the left part shows the visible optical thickness whereas the right part shows the UV optical thickness. In addition, the maximum Gray scale color palette shows the absolute values of the optical thickness. The optical thickness of visible vs UV light for each point in the whole spray region is shown in Fig. 5.2 (b). From the figure it is clear that the values of visible optical thickness are much higher than the UV optical thickness. This is due to the use of image intensifier to capture the UV image. The least square method has been used for comparability of visible and UV phase optical thickness. The blue line $y = 1.76x$ in the Fig. indicates the best fit where x and y represent the visible and UV optical thicknesses. In this paper 1.76 is defined as the correction factor (CF) for the image intensifier. This CF is applied in the analysis of the UV optical thickness of the evaporating spray.

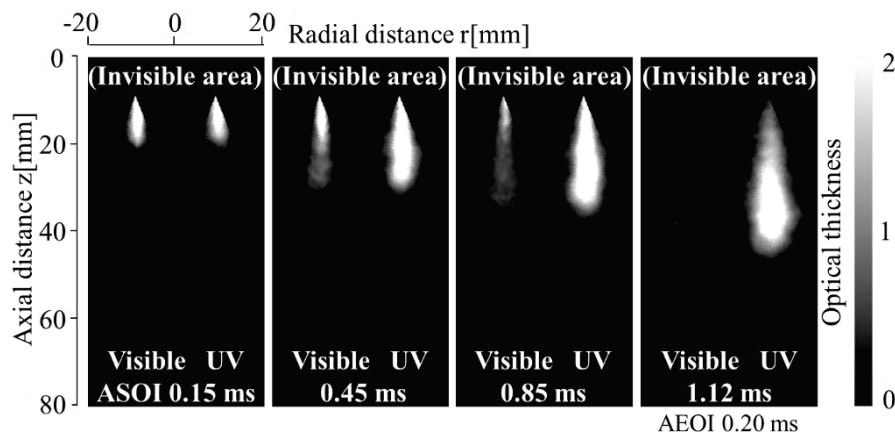
5.3.2 Optical Thickness Images

Figs. 5.3 and 5.4 show the optical thickness images simultaneously at Vis (left column) and UV (right column) wavelengths of the single and average shot spray for two injection mass conditions. In the Figs., the line-of-sight optical thickness at the two wavelengths is shown by the brightness in the spray region of each image, and the gas area around it is colored black. As previously stated, the visible image is only due to the scattering by droplets and hence refers to the distribution of liquid phase, whereas the UV image includes the extinction by both vapor and liquid phases. Since the main purpose of this study is to investigate the spray structure at shot-to-shot variation of the diesel spray, which was not possible by conversional LAS system, maintaining the same ambient condition the experiment was repeated six times. The image acquisition timings displayed in the Fig. 5.3 are selected for the 2.5 mg case at 0.15 ms (SOI transient stage), 0.45 ms (middle quasi-steady stage), 0.85 ms (EOI transient stage) and 1.12 ms ASOI (0.2 ms AEOI), whereas in the Fig. 5.4 for the 5.0 mg case at 0.20 ms (SOI transient stage), 0.85ms (middle quasi-steady stage), 1.55 ms (EOI transient stage) and 1.82 ms ASOI (0.2 ms AEOI) to observe the representative spray characteristics during and after the injection for single and average shot of the spray. However, from Fig. 5.3 (a), at 0.15 ms ASOI, the Vis. (liquid phase) optical thickness is larger than the UV (vapor phase) optical thickness for the single shot spray, because at the SOI

transient stage, the air entrainment was not sufficient for injected fuel evaporation. At 0.45 ms ASOI images represent a similar penetration phenomenon of the spray for single and average shot, except that the vapor phase width is a little bigger. At 0.85 ms ASOI, the droplets evaporate quickly, and fast evaporation rate appears at the spray downstream region. Moreover, at 0.2 ms AEOI, it should be noted that near the nozzle tip, there is a region with UV optical thickness, but visible optical thickness is unclear, which conform that more air entrained into the spray after EOI at the spray tail region for single and average shot spray.

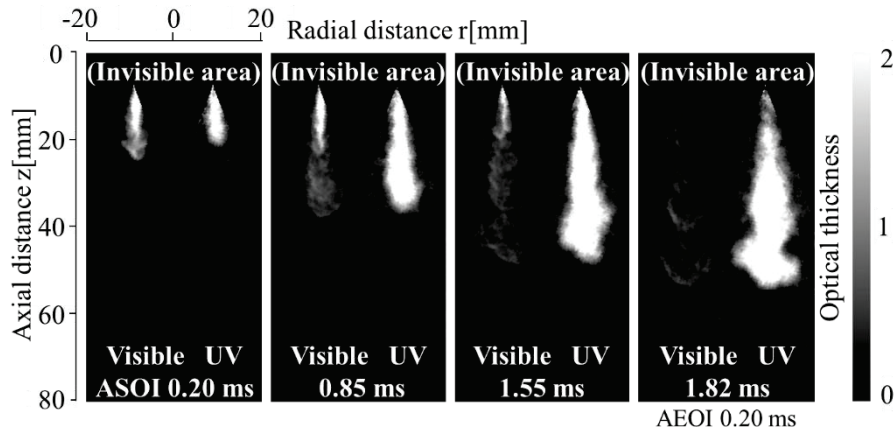


(a) Single shot spray

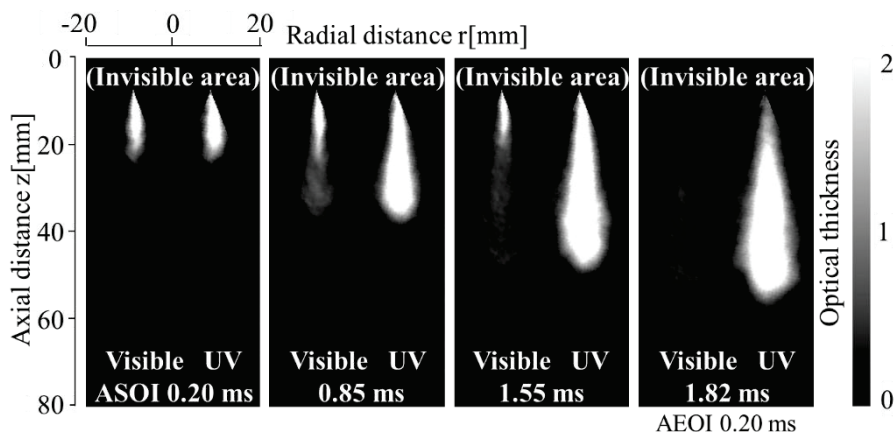


(b) Average shot spray

Fig. 5.3 Spray images in optical thickness at Vis (left column) and UV (right column) wavelengths $M_f=2.5$ mg.



(a) Single shot spray



(b) Average shot spray

Fig. 5.4 Spray images in optical thickness at Vis (left column) and UV (right column) wavelengths $M_f=5.0$ mg.

When injection amount increases to 5 mg as shown in Fig. 5.4, the spray characteristics are same as 2.5 mg condition during the injection period. Considering Fig. 5.3, Fig. 5.4 simultaneously, under the same ambient condition, the larger injection amount has longer penetration, which is a widely accepted phenomenon. However, for the 5.0 mg injection mass condition at 0.2 ms AEOI the spray structure is as like a mushroom shape at the spray tip region for the single shot spray. In contrary, it can be observed that the spray shape is symmetric around the spray axis for the average shot spray.

5.3.3 Comparison of Fuel Mass of Completely Evaporated Spray and Injected Mass

The measurements varying the injection amount were made on a completely evaporated fuel spray to verify the vapor mass measurement accuracy using the LAS technique. For this measurement the injection amounts 2.5 and 5.0 mg/hole were selected. The measurement timings were considered at an adequately long time after the end of injection, so that the liquid fuel would be fully evaporated. It was assumed that the droplets within the spray had fully evaporated when the vapor mass stopped growing over time and no liquid phase could be observed in the visible image. The vapor fuel mass was determined using molecular absorption coefficient data. The results of measured cumulative vapor mass by image analysis versus amount of injected fuel mass are illustrated in Fig. 5.5.

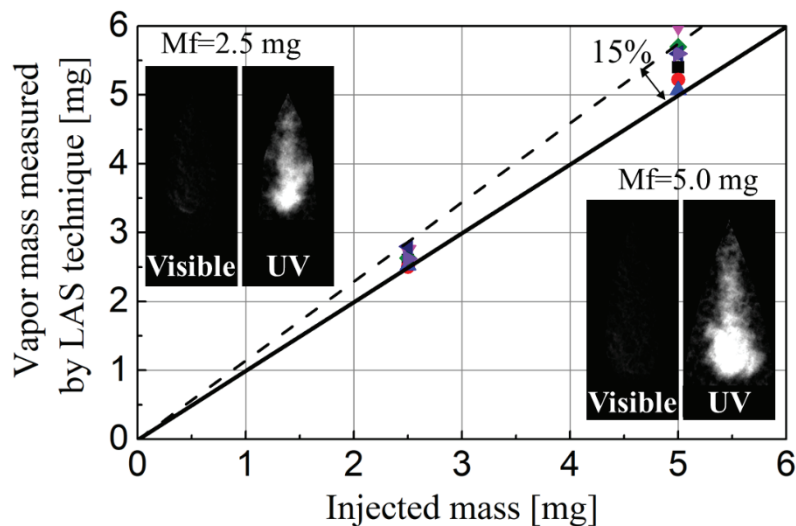
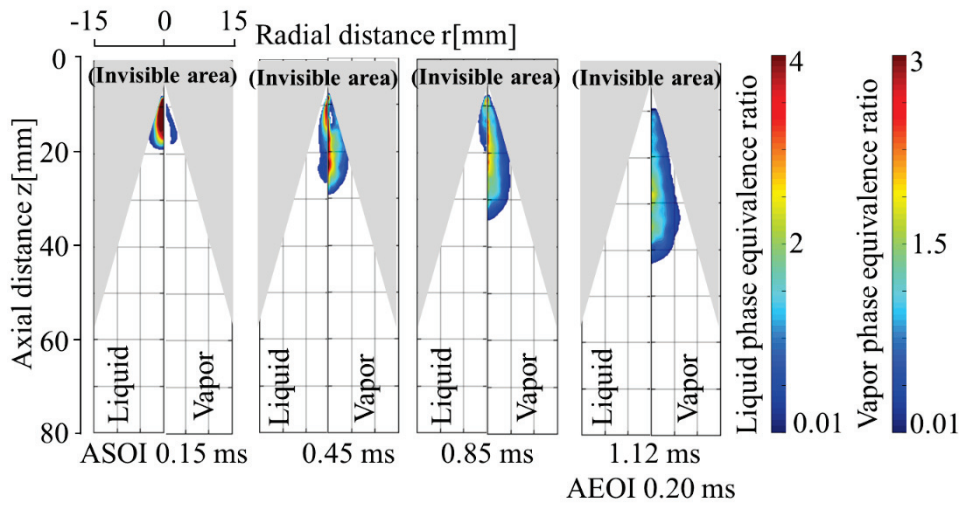


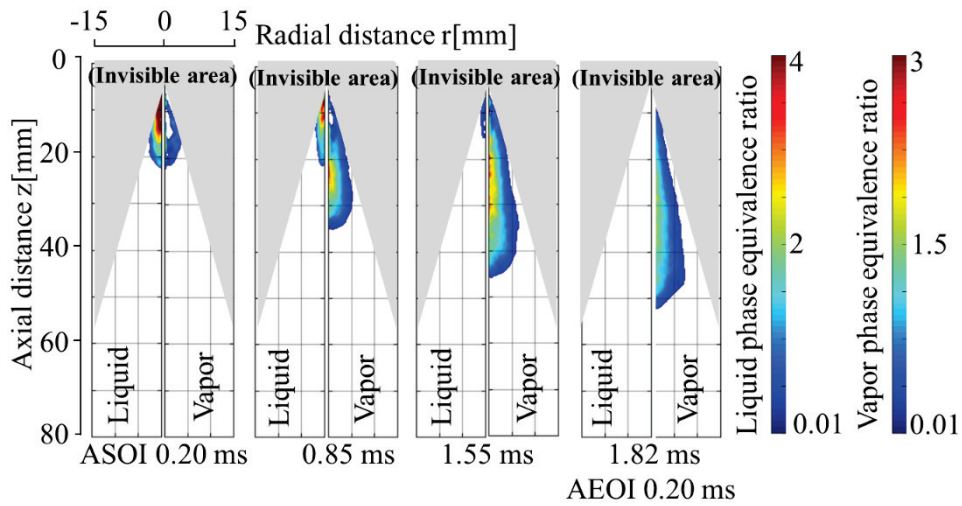
Fig. 5.5 Comparison of vapor mass measured by the LAS technique to injected fuel mass ($T_a=800\text{ K}$, $P_a=4.8\text{ MPa}$, $P_{inj}=100\text{ MPa}$, $M_f=2.5, 5.0\text{ mg}$).

The results obtained by the LAS measurement technique are generally a little different to the total injected fuel mass. However, it should be noted that the estimated vapor mass vs the amount of fuel injected was generally contained within 15% error line. As a result, the vapor measurement applying the LAS technique can be considered reliable to a large extent. The above inaccuracy analysis is based on measurements taken on sprays that have completely evaporated. It should be observed that when liquid droplets are included in the spray, the measuring inaccuracy rises. In the area where the droplets prevail, the inaccuracy can reach ~25-30 %, according to an estimate [160].

5.3.4 Axisymmetric Analysis



(a) $M_f=2.5$ mg

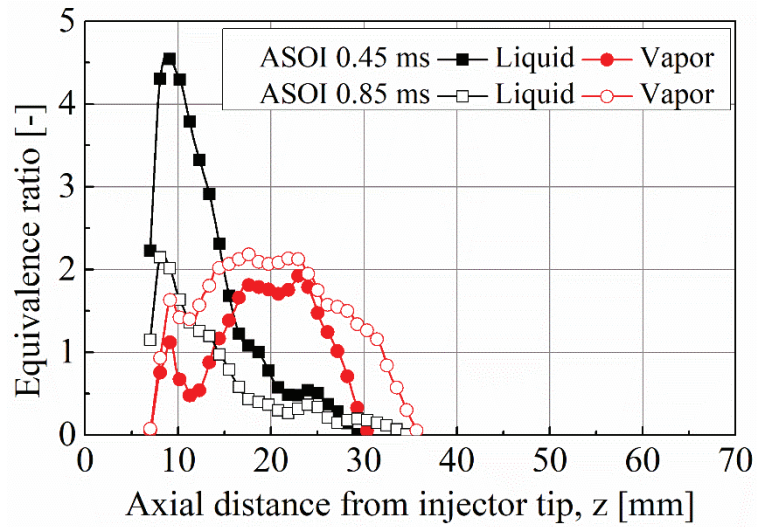


(b) $M_f=5.0$ mg

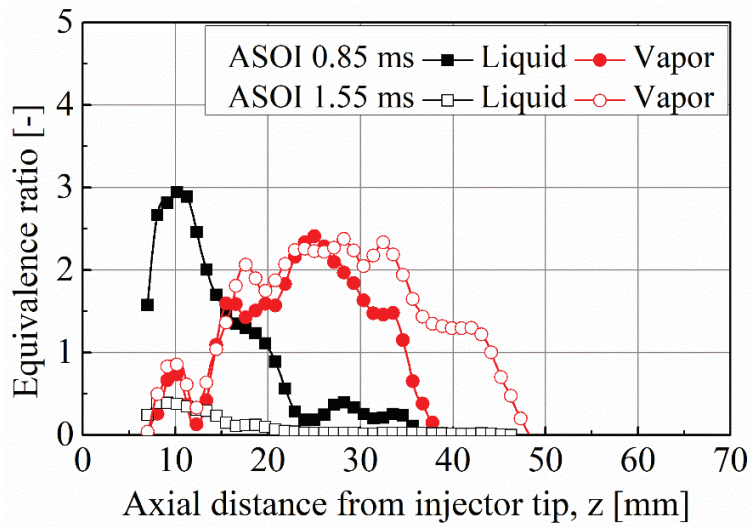
Fig. 5.6 Temporal development of liquid and vapor phase equivalence ratio distributions.

Fig. 5.6 shows the equivalence ratio distributions result of the liquid and vapor phases deconvoluted via the onion-peeling method from the line-of-sight optical thickness images as time elapses under two injection mass conditions. The image acquisition times are selected similar to optical image timings to observe the liquid and vapor phase equivalence ratio distribution during and after the injection. In each case, the Fig. was separated into two parts i.e. the left part shows the liquid phase equivalence ratio whereas the right part shows the vapor phase equivalence ratio. In addition, the

maximum values of the vapor and liquid phase equivalence ratios are 3 and 4, respectively. During the injection period the liquid phase equivalence ratio dominates first and then decreases whereas the vapor phase equivalence ratio increases as time elapses under the two injection mass conditions.

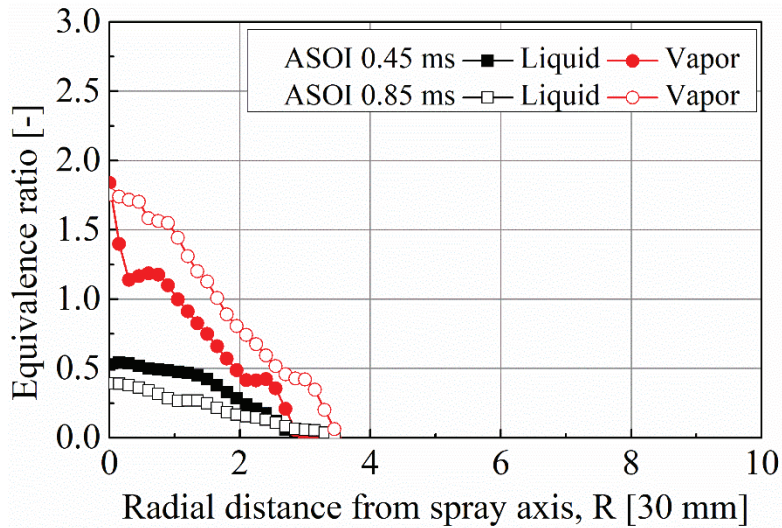


(a) $M_f=2.5$ mg

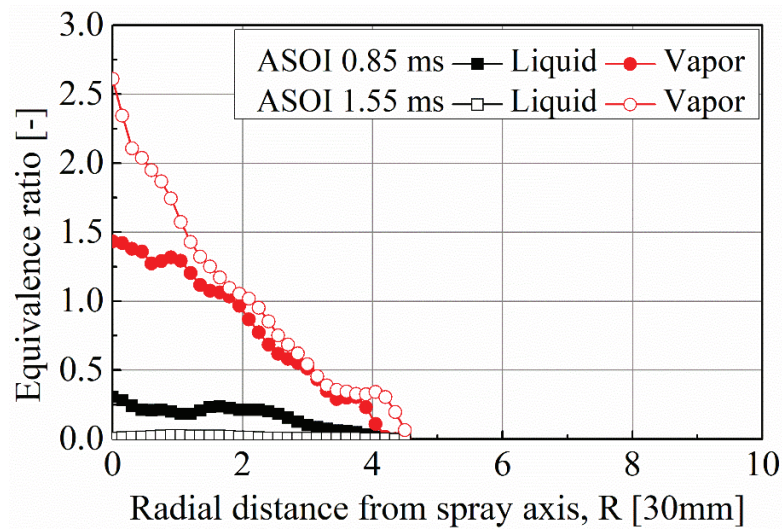


(b) $M_f=5.0$ mg

Fig. 5.7 Axial distribution of liquid and vapor phases equivalence ratio.



(a) $M_f=2.5$ mg



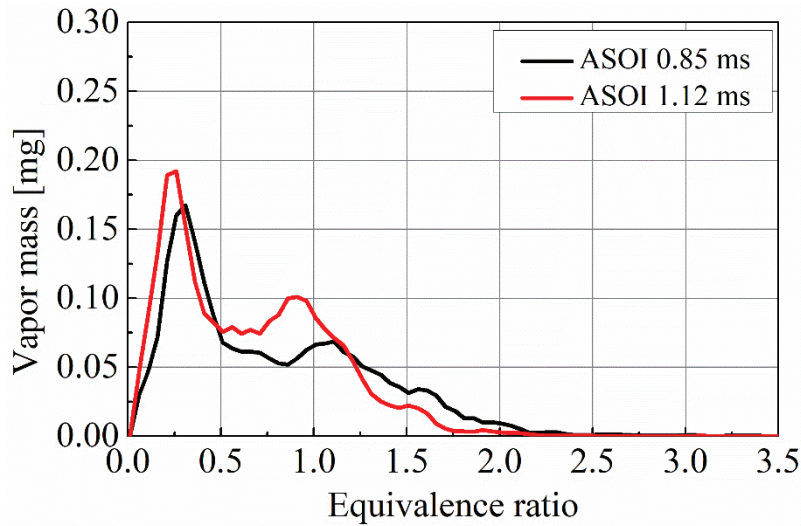
(b) $M_f=5.0$ mg

Fig. 5.8 Radial distribution of liquid and vapor phases equivalence ratio at an axial distance from nozzle tip.

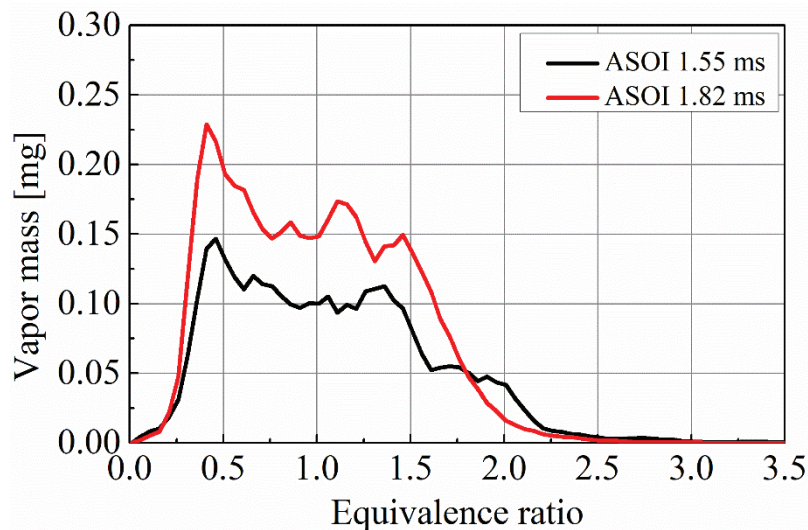
It was previously mentioned that the visible OT was not clear at 0.20 ms after EOI, thus the corresponding equivalence ratio is absent in this timing. At EOI transient stage, it shows that the higher injection amount gives the longer spray tip penetration (STP). The rich vapor concentration phase is formed at 5.0 mg injection mass condition. Moreover, the vapor phase equivalence ratio at this stage is distributed homogeneously at the center position of the spray cloud. However, the magnitude seems lower at 0.20 after EOI which indicates that a leaner mixture dominates after the end of injection timing for the small injection mass condition.

Fig. 5.7 shows the equivalence ratio distributions of liquid and vapor along the spray axis (the average equivalence ratio is determined at every 2 mm from the spray axis for measurement precision) and Fig. 5.6 in the radial direction from the spray center line 25 mm for small injection amount condition whereas 30 mm for large injection mass condition downstream of the nozzle tip at the middle of the quasi-steady stage and the EOI transient stage of the spray. In Fig. 5.7, the liquid phase equivalence ratio curves show a single peak that reduces with axial distance, indicating that the fuel evaporates at the same rate as it is injected. At middle quasi-steady stage, the liquid phase equivalence ratio under small injection mass condition shows the higher peak than vapor phase equivalence ratio even under the large injection mass condition. It means that under the small injection mass condition, the droplet dominated zone is present at this stage. On the other hand, the vapor phase equivalence ratio shows that each curve has two peaks for both conditions. The first peak can be found at a distance of around 10 mm along the spray axis. The cause of this phenomenon is unclear. However, it should be noted that there is a relatively large uncertainty in the determination of the vapor phase equivalence ratio due to the evaluation of a narrow spray close to the invisible area in the presence of a very high drop density. As the spray evolves, the second peak appears closer to the spray tip, according to the stagnation region. In short, the shape of curves is something like a saddleback [57]. The vapor phase equivalence ratio curves are higher than the liquid phase equivalence ratio curves, as shown in Fig. 5.8. The curves of vapor show that the equivalence ratio decreases with respect to radial distance from the centreline of the spray axis (Gaussian shape). This suggests that as the fuel spray penetrates further, greater air entrainment occurs. However, under large injection mass condition, the liquid phase equivalence ratio is quite low and close to zero at 1.55 ms ASOI. This means that as the air-fuel mixing quality improves, the majority of the liquid fuel evaporates and is transformed to vapor.

As illustrated in Fig. 5.9, the contour data from Fig. 5.6 can be rearranged to represent the vapor mass distribution as a function of equivalence ratio. The curve shows the quantity of vapor mass that is present at every 0.05 interval in the equivalence ratio. As a result, the total amount of fuel in the vapor phase is equal to the integration of the area produced by the profile divided by 0.05. In Fig. 5.9 (a), it displays the correlation between the vapor mass and equivalence ratio under the 2.5 mg injection mass condition. After the end of injection there is a relatively significant volume with lean mixture with a peak at an



(a) $M_f=2.5$ mg

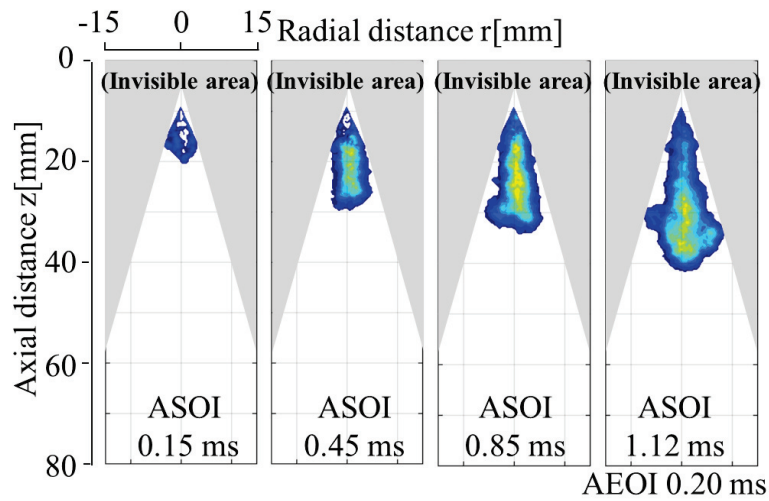


(b) $M_f=5.0$ mg

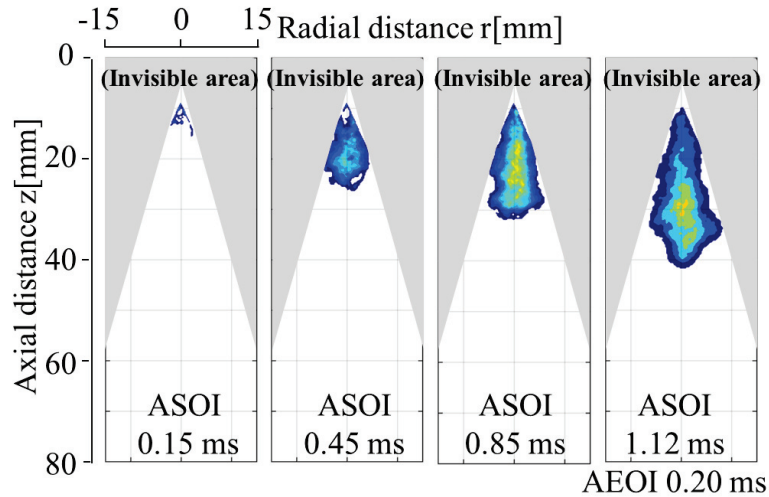
Fig. 5.9 The comparison of the vapor mass distribution against equivalence ratio. equivalence ratio of less than 0.3. On the other hand, the mass distribution at 0.85 ms ASOI timing also revealed that, the total mass of rich mixture with an equivalence ratio of above 1.5 was slightly greater that after the end of injection timing. In Fig. 5.9 (b), it shows the relationship between the vapor mass to the equivalence ratio under 5.0 mg injection mass condition. After the end of injection there is a relatively significant volume with lean mixture with a peak at an equivalence ratio of less than 0.5. On the other hand, the mass distribution at 1.85 ms ASOI timing also revealed that, the total mass of rich mixture with an equivalence ratio of above 2 was slightly greater that after the end of injection timing. Comparing with the result of Fig. 5.9, it is evident that as the injection mass rises, the air-fuel combination gets richer.

5.3.5 Non-Axisymmetric Analysis

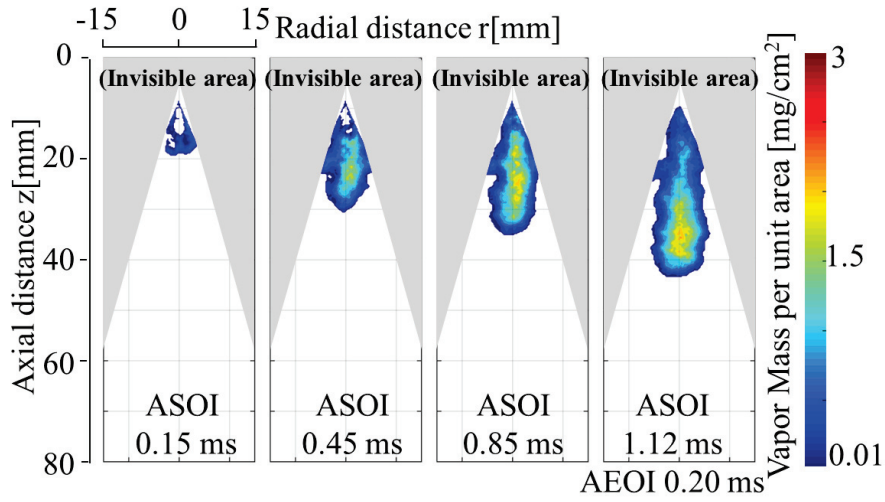
The time evolution of individual line-of-sight vapor fuel mass concentration shot to shot variation for two conditions are presented in Fig. 5.10 and 5.11. The color palette in Fig. 5.10 (c) and 5.11 (c) show the absolute values of vapor mass per unit area mg/cm^2 in the vapor phase image. The maximum value of the vapor mass for the vapor phase was set to 3. The representative acquisition timings are at 0.15 ms, 0.45 ms, 0.85 ms ASOI and 0.2 ms after the end of injection for 2.5 mg injection mass condition



(a) Shot 1

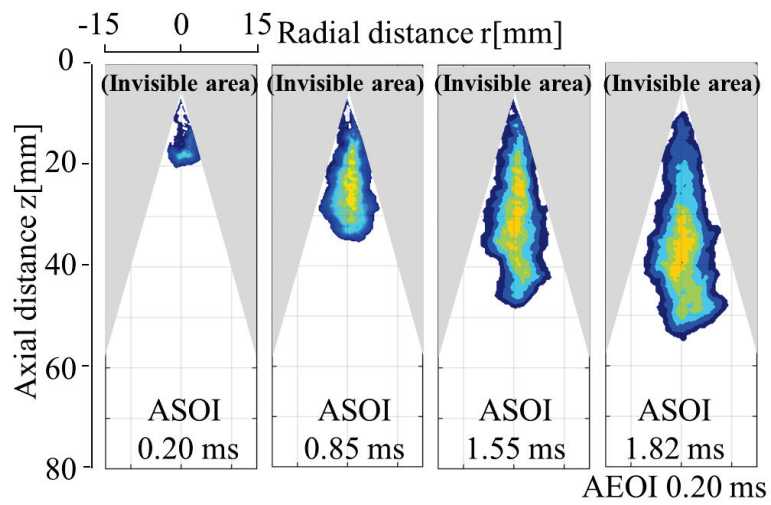


(b) Shot 2

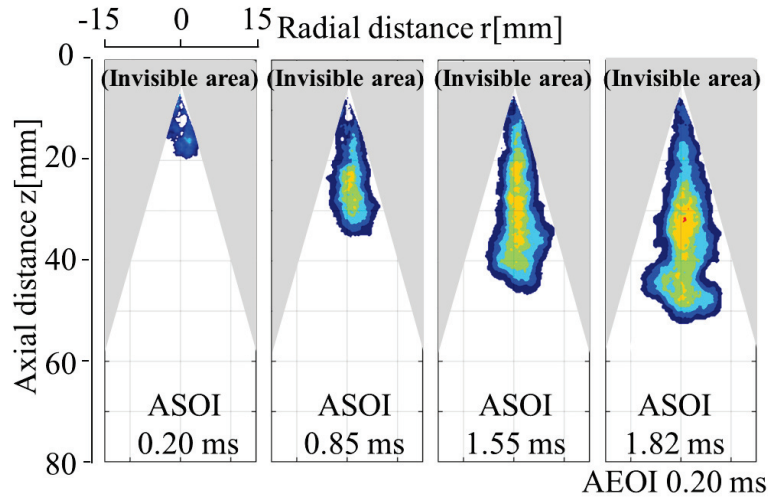


(c) Shot 3

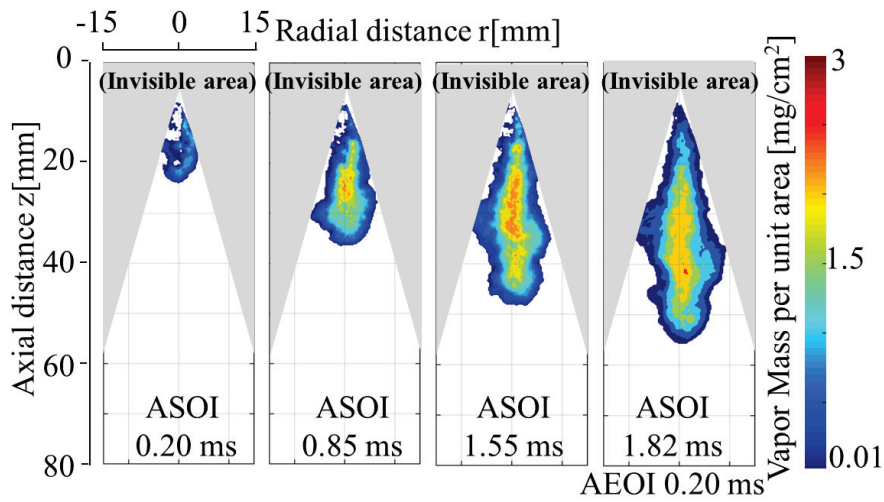
Fig. 5.10 Evaluation of individual vapor fuel mass distribution fields for $M_f=2.5$ mg.



(a) Shot 1



(b) Shot 2



(c) Shot 3

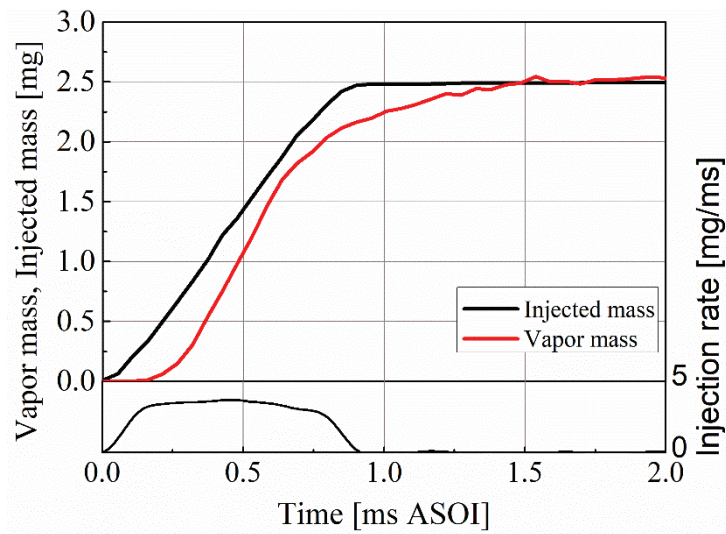
Fig. 5.11 Evaluation of individual vapor fuel mass distribution fields for $Mf=5.0$ mg.

whereas at 0.20 ms, 0.85 ms, 1.55 ms ASOI and 0.2 ms after the end of injection for 5.0 mg injection mass condition. Fig. 5.10 depicts the penetration of fuel vapor into the spray chamber as time elapses for each spray shot. Large fluctuations are probably responsible for the corrugated shape of the spray tip location. The high concentration zone for the third shot following the end of injection timing can be seen downstream of the spray, indicating that the fuel mass concentration gradients are steep. However, the fuel mass concentration gradients rise to be less progressive on the spray's upstream sides. In Fig. 5.10, at 0.85 ms ASOI, for the first and third shot, it can be seen that the comparatively high vapor concentration regions are visible at the middle of the spray,

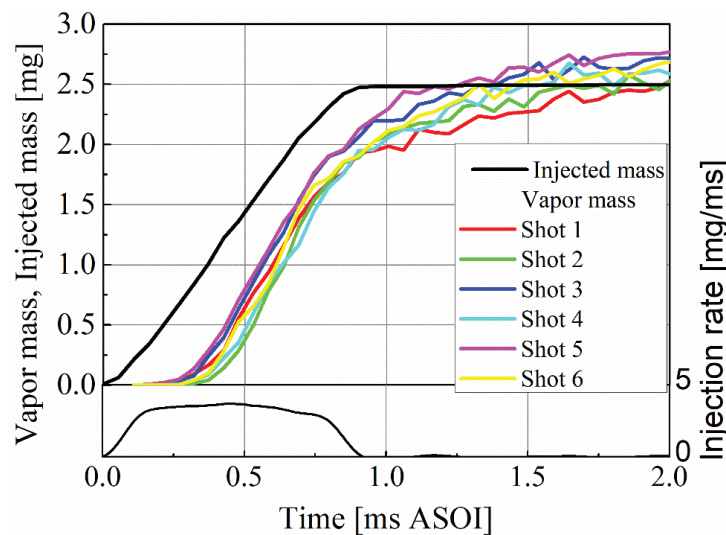
which increases slowly while the spray penetrates as time elapse. After the end of injection for every shot, the high vapor concentration regions near the nozzle quickly mix with ambient gas, reducing vapor concentrations to low levels in a few tenths of a millisecond. This finding is due to the air entrainment conservation kinematics after the end of injection. Consequently, a low-vapor-concentration region forms rapidly at the spray's tail, represented by green and blue color, after the end of injection, while a high-vapor-concentration region remains close to the spray's tip, represented by yellow color, where the mixing with air is considerably high [109,110]. Therefore, at the first glance every shot spray seems to follow the same path. Also, when precisely comparing the structure at the tip, a difference can be observed between the different shots. However, some larger lean fuel concentration areas (indicated by the blue color) are observed at the radial periphery of the third shot. For this shot, injected fuel mix with the air quickly after the end of injection and form lean fuel concentration areas in peripheral regions.

The temporal variation of the vapor mass distribution on average (axisymmetric) and shot-to-shot (non-axisymmetric) variation compared with nominally injected mass under case 1 and case 2 are shown in Fig. 5.12 and 5.13. The evaporation ratio of every injection timing can be calculated by the measured vapor mass since the evaporation ratio is dependent on the vapor mass and injected mass. In Fig. 5.12, The vapor mass is smaller than the injected mass for every shot during the injection time, except for the axisymmetric spray, because liquid droplets predominate in the spray during the injection phase. This indicates that the fuel has not completely evaporated. However, for the axisymmetric spray, the vapor mass is quite comparable to the injected mass after the end of injection timing, whereas for some non-axisymmetric spray shot sprays, the vapor mass increases as time elapses. In Fig. 5.13, it should be observed that from 0.0 to 0.6 ms ASOI for the axisymmetric spray whereas, from 0.0 to 0.80 ms ASOI for the non-axisymmetric spray the vapor mass is much lower than the injected mass for all shots since at this injection duration liquid droplets are dominating in the spray. However, the vapor mass increases with time elapse for average, and all shot sprays. In general, AEOI the vapor mass curve should be parallel to the injected mass curve after completely evaporating spray, but some curves do not follow the above rule. This is one of the possible reasons why the error of vapor measurement accuracy using the extended LAS technique. The fact that the measured vapor mass appears to increase after end of injection may among other things also be

related to temperature-dependent molar absorption coefficient (MAC), since when the fuel mixture is further diluted the average temperature of the fuel molecules should increase.

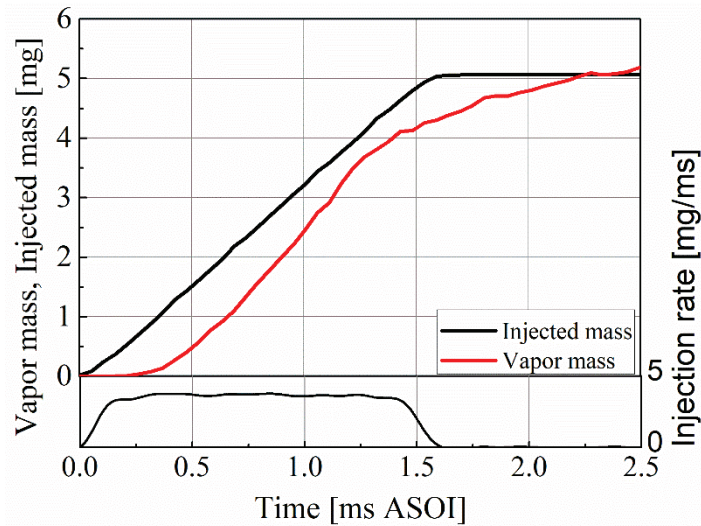


(a) Axisymmetric

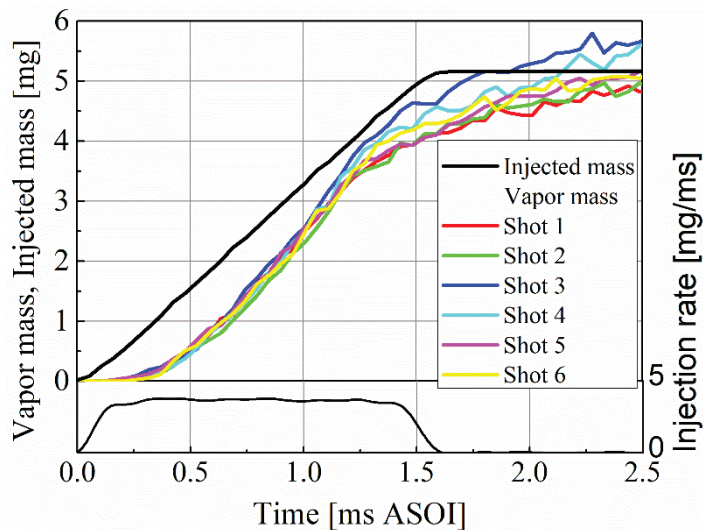


(b) Non-axisymmetric

Fig. 5.12 Temporal development of the vapor mass distributions $M_f=2.5$ mg.



(a) Axisymmetric



(b) Non-axisymmetric

Fig. 5.13 Temporal development of the vapor mass distributions $M_f=5.0$ mg.

5.4 SUMMARY

The high-speed laser absorption scattering (HS-LAS) technique for measuring quantitative information of vapor as well as liquid in fuel spray has been developed by using UV LED and CW laser as continuous light sources, high-speed video cameras, and image intensifier for UV light. The diesel replacement fuel which consists of 97.5 % n-tridecane and 2.5 % of volume-based 1-methylnaphthalene was used. Quantitative studies of vapor and liquid fuel distribution in injected diesel sprays into a high-temperature and high-pressure environment were carried out using this technique. The summary of the conclusions are as follows:

1. The difference in the UV and visible optical thickness, which significantly affects the accuracy of vapor resolve, was observed using simultaneous measurements of optical thickness at 266 nm and 532 nm wavelengths of a non-evaporating fuel spray injected into a high-density atmosphere by a high-pressure injection technique. Due to the employment of an image intensifier to capture the UV image, the result indicates that there is a significant variation in optical thickness between the two wavelengths. During the processing of the evaporating spray images, an intensifier correction factor was applied to the UV phase optical thickness in order to compare the visible and UV phase optical thicknesses.
2. A sequence of experiments on the completely evaporated fuel spray were conducted to confirm the vapor measurement. The vapor mass measured from the optical thickness of vapor phase by imaging approach agrees well with the injected fuel mass.
3. Simultaneous vapor and droplet measurements are carried out. The following points are drawn from the findings.
 - (a) In most areas of the spray plume, vapor optical thickness is substantially greater than droplet optical thickness, except in the upstream, droplet-dominated zone.
 - (b) During the injection period the liquid phase equivalence ratio dominate first and then decreases whereas the vapor phase equivalence ratio increases as time elapses under the two injection amount conditions.
 - (c) Under large injection mass condition, the liquid phase equivalence ratio is quite low and close to zero at EOI transient stage. This means that as the air-fuel mixing quality improves, the majority of the liquid fuel evaporates and is transformed to vapor. Also, the air-fuel mixture becomes rich when the injection mass increases.
 - (d) At 5.0 mg injection mass condition, after the end of injection the high vapor concentration regions near the nozzle quickly mix with ambient gas, reducing vapor concentrations to low levels, while a high-vapor-concentration region remains at the spray's tip.

CHAPTER 6 CLOSURE

The mixing of evaporating fuel spray with air is known to have a key role in the subsequent ignition and combustion process, as well as pollutant generation in diesel engines. The ignition characteristics and development of combustion are all controlled by spatial and temporal variations in the fuel-air mixing process. The atomization and vaporization features of the intermittent fuel spray are greatly dependent on this turbulent mixing event. However, due to a lack of adequate diagnostic techniques, the reciprocal relationships of these individual effects are not well recognized.

On the other side, as the world's population of automobiles grows, global environmental concerns have become more severe. In addition to harmful exhaust emissions, global warming produced by the greenhouse effect has received a lot of international attention in recent years. Despite the remarkable accomplishment of passenger car engines in decreasing gaseous and particulate emissions to a fraction of what they were a decade ago, the accompanying development in thermal efficiency and fuel consumption has been, by any standard, extremely modest. Automobile experts are focusing their efforts on developing diesel engines and spark ignition direct injection engines in order to reduce exhaust pollutants and fuel consumption at the same time. However, today's automotive diesel engine technology, such as turbocharging, improved combustion, multi-valve, and injection pressure level elevation, are unable to meet the new rules. As a result, in addition to upgrading all of the basic technologies, new technologies must be included. Aside from some novel exhaust gas aftertreatment technologies, the electronic control and injection rate shaping are expected to increase diesel engine performance significantly. One of these novel techniques is split injection.

The particulate vs. NO_x emission tradeoff curves of diesel engines can be pushed closer to the origin utilizing split-injection approach combined with high injection pressure than when using single-pulse injection, according to experiments. For internal combustion engines, this is a brand-new fuel injection concept. Clarifying the mechanism of fuel-air mixture production in split injection diesel spray will yield much greater benefit, not only in terms of recognizing a novel fuel-air mechanism, but also in terms of determining what sort of spray formation method will be used in future diesel engines. However, how are the properties of split-injection diesel spray associated to

injection mass ratios and dwell, and why might NO_x-particulate emissions be reduced by employing split-injection? and so on, are still unidentified.

The high-speed absorption-scattering (HS-LAS) optical diagnostic system was developed for achieving a reliable simultaneous measurement of vapor and liquid concentration in diesel sprays in this research. Using tracer LAS as the test fuel and irradiating with the fourth harmonic and the second harmonic of a UV LED and CW laser, the accuracy of the vapor measurement based on the ultraviolet-visible laser absorption-scattering imaging approach was improved. The distributions of vapor concentration in diesel sprays were simultaneously measured using this LAS technique on single-pulse and double-pulse injection diesel sprays, and the features of the equivalence ratio of fuel-air mixture, fuel evaporation, and air-entrainment in free injection sprays were quantitatively analyzed. The split ratio and dwell between injections were used to determine the parameters of split injection diesel sprays. The ultraviolet visible LAS technique was also used to qualitatively visualize the line-of-sight distributions of optical thickness of vapor and droplets in split-injection evaporating diesel sprays to better understand the fuel-air mixing behavior of the single and double-pulse injection diesel sprays.

In chapter 1, review of the characterization of diesel sprays, diagnostics of vapor and liquid concentration in the fuel spray, split-injection spray, and their combustion in diesel engines was presented. This chapter showed the significance of this research subject.

In chapter 2, the experimental apparatuses and measurement methods are introduced. The apparatuses include the high-pressure high temperature constant volume chamber, fuel injection system, injection rate measurement system, the principle of Laser Absorption Scattering technique, optical arrangement of the conventional LAS and the HS-LAS system, Multi-hole Injector Adaptor, Image processing area and Constant Volume Spray Chamber, natural luminosity recording system, Two-Color pyrometry method and calibration method.

In chapter 3 illuminates the molar absorption coefficient measurement of tracer LAS test fuel. It can be observed that the 1-MN have absorbance at a wavelength of 266 nm. For the high temperature case, the absorbance peak is greater, and the absorbance spread is narrower. The absorption spectra near the wavelength of 266 nm are in similar

value for the different temperature. The absorbance has linearity with respect to the molar concentration up to the typical conditions. However, the best fitting line of the 3.0 and 4.0 MPa cases are almost similar. The molar absorptivity is found to have a low temperature dependence. For the 4.8 MPa condition, when the atmospheric temperature reaches 800K, the absorbance tends to increase compared to the range of 550K-750K.

In Chapter 4, an experimental study was conducted to investigate the mixture formation and combustion characteristics of a split-injection diesel spray. LAS technique was employed to determine the mixture concentration of the spray, whereas the two-color pyrometer method was used to analyse the combustion flame structure. To overcome any differences in the spray structure from a single-hole injector, a commercial seven-hole injector was selected. To observe the effect on mixture formation and combustion fixing the small dwell time, three split ratios, i.e., 3:7, 5:5, and 7:3, were selected. It is found that, the evaporation ratio of the first two split ratio setups was evidently higher than that for the third split ratio owing to the lower amount of fuel quantity in the first injection. Moreover, the 3:7 split ratio resulted in a wider “over rich” mixture inside the spray. This is because the vapor of the second spray merged with the vapor of the first spray and resulted in a compact structure, which consequently turned into the “over rich” mixture. Considering the three split ratios, it could be concluded that 7:3 is the best for mixture formation in the present study. The ambient air and fuel mixture made from the first injection is applied to the spray of the second injection; accordingly, the leaner mixture made from the first injection is in a convenient place. After the first injection is completed, the air inlet wave rapidly shapes the nozzle flow mixture. Furthermore, this split ratio provides the right amount of fuel for exploring the lean area in the first injection fuel mixture. Thus, compared with the other two split ratios, an overall leaner structure is formed. The 7:3 split ratio has shown a positive effect on the soot reduction of KL against the flame temperature. All three split ratios showed that the high temperature range was considerably higher, and the low KL factor area was greater for the flame area of temperature and KL factor distributions. The soot formation process for the 3:7 and 5:5 split ratios was investigated. The first injection fuel blends with the greater amount of the second injection fuel to create a fuel pile; this deteriorates the combustion region and influences soot formation. For the 7:3 split ratio, the interaction of the burned gas with the ambient gas inside the combustion chamber during the injection pause time promoted combustion and reduced soot oxidation.

However, the limitation of this study is that this conclusion is valid only for the free spray conditions and could differ when an impinging spray, such as the combustion inside an actual engine, is considered. To investigate the effects of dwell time on mixture formation and combustion processes for the same split ratio, three dwell times, i.e. 0.12, 0.32, and 0.54 ms, were selected. It has been observed that, in the 0.32 ms dwell time case, the vapor penetration of the second injection was relatively higher than that of the first injection owing to the 'slipstream' effect. Nevertheless, the mixture became rich in the 0.32 ms dwell time case. With the extended penetration of the second injection, the weaker air entrainment between the dwell durations might have resulted in the rich mixture. In the 0.12 ms dwell time case, the equivalence ratio distribution decreased uniformly from the rich mixture region to the lean mixture region. The shorter dwell time case yielded a suitable position for the second injection around the boundaries of the first injection by smoothly growing the lean mixture and avoiding the rich mixture's large zone. The combustion results demonstrated that, the KL factor of the single injection was significantly higher than that of the split injection. Moreover, the single and 0.32 ms dwell case indicated the highest integrated KL factor, which decreased rapidly subsequently; this implied that the single injection and 0.32 ms case decreased the amount of soot rapidly. At a short dwell time, the interaction between nitrogen gas and the combustible gas within the combustion cell during the injection pause promoted ignition and oxidised the soot smoothly.

In Chapter 5, the high-speed laser absorption scattering technique to record the distribution of whole vapor phase in an injection event and measuring quantitative information of vapor and liquid in fuel spray has been developed by using UV LED and CW laser as continuous light sources, high-speed video cameras, and image intensifier for UV light. Firstly, the comparison of UV and Vis optical thickness of non-evaporating, optical thickness image of evaporating spray and comparison of fuel mass of completely evaporating spray and injected mass are discussed. Second, the contours of equivalence ratios of droplets-gas mixture and vapor-gas mixture in diesel sprays are obtained, clarifying the spray mixture structures, and temporal variations in fuel distributions are shown to know the development of flow behavior at a time after the start of injection in accordance with axially symmetric sprays. Finally, the non-axisymmetric analysis' shot to shot variation temporally vortex/eddy features are investigated. The following conclusions are based on the findings:

Simultaneous measurements of optical thickness at 266 nm and 532 nm wavelengths of a non-evaporating fuel spray injected into a high-density atmosphere using a high-pressure injection technique revealed the difference in UV and visible optical thickness, which has a significant impact on vapor resolve accuracy. The result reveals that there is a considerable difference in optical thickness between the two wavelengths due to the use of an image intensifier to capture the UV image. In order to compare the visible and UV phase optical thicknesses, an intensifier correction factor was applied to the UV phase optical thickness during the processing of the evaporating spray images. To confirm the vapor measurement, a series of experiments were carried out on completely evaporated fuel spray. The vapor mass determined by imaging the optical thickness of the vapor phase agrees well with the injected fuel mass. Simultaneous vapor and droplet measurements are carried out. The following points are drawn from the findings.

(i) In most areas of the spray plume, vapor optical thickness is substantially greater than droplet optical thickness, except in the upstream, droplet-dominated zone.

(ii) During the injection period the liquid phase equivalence ratio dominates first and then decreases whereas the vapor phase equivalence ratio increases as time elapses under the two injection amount conditions.

(iii) Under large injection mass condition, the liquid phase equivalence ratio is quite low and close to zero at EOI transient stage. This means that as the air-fuel mixing quality improves, the majority of the liquid fuel evaporates and is transformed to vapor. Also, the air-fuel mixture becomes rich when the injection mass increases.

(iv) At 5.0 mg injection mass condition, after the end of injection the high vapor concentration regions near the nozzle quickly mix with ambient gas, reducing vapor concentrations to low levels, while a high-vapor-concentration region remains at the spray's tip.

RECOMMENDATIONS FOR FUTURE WORKS

For further research in this area, several recommendations might be made. Further research is required to determine the precise process by which liquid influences spray development and combustion. In order to avoid the significant difference between the visible and UV optical thickness of the non-evaporating and evaporating diesel sprays, it is imperative that the HS-LAS optical arrangement should be improved. Until now,

the LAS/HS-LAS technique cannot measure the liquid mass of the evaporating spray. So, the precision of LAS/HS-LAS technique on the liquid phase should be improved. To develop a better injection strategy that can prevent the second main injection from catching up with the first injection flame, other injection techniques, such as another split main injection mass ratios, should be further researched. To discover the appropriate oxygen concentration that can greatly reduce soot emissions, various oxygen concentrations should also be researched. Further research on the characteristics of liquid fuel should also be done using computational fluid dynamics to simulate the evolution of the spray.

According to recent findings, the split injection helps to reduce soot emissions. The main injection combustion can be enhanced via pre-injection combustion. A decrease in soot emissions should result from increasing the split injection interval. Therefore, additional foundational studies using various injection techniques are advised.

The ultimate goal of this research is to boost an actual engine's performance. Although this work's physical ambient circumstances are similar to those in a genuine engine, the mixture formation and combustion process may be impacted by turbulent flow. It is advised that alternative chamber shapes, injection pressures, injection amounts, and multiple injection strategies be used in order to examine the mixture formation and combustion behaviors in an optical engine.

ACKNOWLEDGEMENT

Without the support and guidance of my supervisors, parents, relatives, and colleagues, I would not have been able to complete my study. To being, I would want to express my gratitude to my academic supervisor Professor Keiya NISHIDA. Thank you very much for giving me with adequate resources, flexibility, and an environment in which new ideas could be explored. Prof. NISHIDA has provided me with the most extensive,

relevant, and constructive support and guidance which I have never received before. I am extremely grateful and indebted to him.

Prof. Yasuhiro Suzuki, Prof. Yoichi Ogata, Prof. Hongliang Luo and Prof. Mats Andersson have also been invaluable mentors to me throughout this study period. Dr. Jaeheun Kim and Dr. Yu Jin were invaluable advisors, particularly in the area of experimental research. I am very thankful to my colleagues including Dr. Rizal, Dr. Safiullah. Dr. Zhai, Mr. Fan, Dr. Guo, Mr. Kakami and Mr. Naito for their support in building experimental works, rigs and off-campus events. I would want to express my gratitude to Japan's Ministry of Education, Culture, Sports, Science, and Technology for supporting my education by providing a scholarship and tuition fees. Also, I am grateful to SIP for providing injection system.

Finally, I am extremely fortunate to have my parents always at my side. From the beginning of my basic education through achieving the highest academic award, their unwavering love and encouragement have aided me in obtaining a respectable profession. My wife Laboni Rani Sarder and son Jayce Ray deserve deepest gratitude for their love, mental support, and patience.

REFERENCES

- [1]. Pierpont DA, Montgomery DT and Reitz RD. Reducing particle and NO_x using multiple injection and EGR in a D.I. diesel. SAE Paper 950217, 1995.
- [2]. Scolari P. Towards a sustainable mobility at the turn of the century: the environmental challenge. *ATA-Ingegneria Automotoristica* 1997; 50:11-12.
- [3]. Endo S. Powertrain Technologies of Commercial Vehicles for Today and Future. *SAE/JSAE International, Keynotes*. Kyoto, Japan, 2011.

- [4]. Alperstein M, Swim WB and Schweitzer PH. Fumigation Kills Smoke-Improves Diesel Performance. *SAE Technical Paper* 580058, 1958.
- [5]. Musu E, Gentili R and Reitz RD. Homogeneous Charge Progressive Combustion (HCPC): CFD Study of an Innovative Diesel HCCI Concept. *SAE Technical Paper* 2009-01-1344, 2009.
- [6]. Sandia National Laboratories. <http://crf.sandia.gov/how-low-temperature-combustion-enables-cleaner-more-efficient-engines/>.
- [7]. Kalghatgi G, Hildingsson L and Johansson B. Low NO_x and Low Smoke Operation of a Diesel Engine Using Gasoline-Like Fuels. *ASME ICES*, 2009.
- [8]. *Wisconsin Engine Research Consultants* <https://www.w-erc.com/services/rcci/>.
- [9]. Li J, Yang WM, An H, et al. Application of Dynamic ϕ -T Map: Analysis on a Natural Gas/Diesel Fueled RCCI Engine. *Journal of Engineering for Gas Turbines and Power* 2016; 138.
- [10]. Dec JE. Advanced Compression-Ignition Engines-Understanding the In-Cylinder Processes. *Proc. Combust. Inst.* 2009; 32(2):2727-2742.
- [11]. Splitter D, Kokjohn S, Rein K, et al. An Optical Investigation of Ignition Processes in Fuel Reactivity Controlled PCCI Combustion. *SAE Int. J. Engine* 2010; 3(1):142-162.
- [12]. Hiroyasu H and Arai M. Structures of Fuel Sprays in Diesel Engines. *SAE Technical Paper* 900475, 1990, doi:10.4271/900475.
- [13]. Crua C, Heikal MR and Gold MR. Microscopic Imaging of the Initial Stage of Diesel Spray Formation. *Fuel* 2015; 157:140-150.
- [14]. Musculus M and Kattke K. Entrainment Waves in Diesel Jets. *SAE Int. J. Engines* 2009; 2(1):1170-1193.
- [15]. Pickett L, Manin J, Genzale C, Siebers D, et al. Relationship between Diesel Fuel Spray Vapor Penetration/ Dispersion and Local Fuel Mixture Fraction. *SAE Int. J. Engines* 2011; 4(1):764-799.
- [16]. Siebers DL. Scaling Liquid-Phase Fuel Penetration in Diesel Sprays Based on Mixing Limited Vaporization. *SAE Technical Paper* 1999-01-0528, 1999, doi:10.4271/1999-01-0528.
- [17]. Musculus MPB, Lachaux T, Pickett LM, et al. End-of-Injection Over-Mixing and Unburned Hydrocarbon Emissions in Low-Temperature-Combustion Diesel Engines. *SAE Technical Paper* 2007-01-0907, 2007.

- [18]. Naber JD and Siebers DL. Effects of Gas Density and Vaporization on Penetration and Dispersion of Diesel Sprays. SAE Technical Paper 960034, 1996, doi:10.4271/960034.
- [19]. Arai M. Physics behind Diesel Spray and Its Combustion (LAP Lambert Academic Publishing, 2016), ISBN 13: 9783659971600.
- [20]. Arai M. Physics behind Diesel Sprays. In: *ICLASS 2012, 12th Triennial International Conference on Liquid Atomization and Spray Systems*, Heidelberg, Germany, Sep. 2-6, 2012.
- [21]. Desantes JM, Payri R, Salvador FJ, et al. Development and Validation of a Theoretical Model for Diesel Spray Penetration. *Fuel* 2006; 85:910-917.
- [22]. Dec JE. A Conceptual Model of DI Diesel Combustion Based on Laser-Sheet Imaging. SAE Technical Paper 970873, 1997, doi:10.4271/970873.
- [23]. Aizawa T, Kosaka H and Mastui Y. Imaging of Soot Formation Process in a Diesel Spray Flame Via Double Wavelength Laser Sheet Method. In *17th Internal Combustion Engine Symposium*, Japan 2002, 229-232.
- [24]. Payri R, Gimeno J, Venegas O, et al. Effect of Partial Needle Lift on the Nozzle Flow in Diesel Fuel Injector. SAE Technical Paper 2001-01-1827, 2001, doi:10.4271/2001-01-1827.
- [25]. Salvador FJ, Martines-Lopez J, Caballer M, et al. Study of the Influence of the Needle Lift on the Internal Flow and Cavitation Phenomenon in Diesel Injector Nozzles by CFD Using RANS Methods. *Energy conversion and management* 2013; 66:246-256.
- [26]. Ricaud JC and Lavoisier F. Optimizing the multiple injection settings on an HSDI diesel engine. In: Whitelaw JH, Payri F, Arcoumanis C, et al. (eds) *Thermo- and Fluid Dynamic Processes in Diesel Engine*, Berlin, Heidelberg: Springer-Verlag, 2004, pp. 199–234.
- [27]. Magdi KK and Hannu J. Diesel fuel injection. https://www.dieselnet.com/tech/diesel_fi.php (2013, accessed).
- [28]. Cung K, Moiz A, Johnson J, et al. Spray-combustion interaction mechanism of multiple-injection under diesel engine conditions. *Proc Combust Inst* 2015; 35(3): 3061–8.
- [29]. Miyaki M, Fujisawa H, Masuda A, et al. Development of New Electronically Controlled Fuel Injection System ECD-U2 for Diesel Engines. SAE Technical Paper 910252, 1991, <https://doi.org/10.4271/910252>.

- [30]. Guerrassi N and Dupraz P. A Common Rail Injection System for High Speed Direct Injection Diesel Engines. SAE Technical Paper 980803, 1998.
- [31]. Bachalo WD. Spray Diagnostics for The Twenty-First Century. *Atomization and Sprays* 2000; 10(3):439-474.
- [32]. Dec J. A Conceptual Model of DI Diesel Combustion Based on Laser-Sheet Imaging. SAE Technical Paper 970873, 1997, <https://doi.org/10.4271/970873>.
- [33]. Soid SN and Zainal ZA. Spray and combustion characterization for internal combustion engines using optical measuring techniques—a review. *Energy* 2011;36(2):724-41.
- [34]. Jin Y. Characterization of Diesel Spray and Mixture Formation Processes Under Small Injection Amount Condition. Doctor degree dissertation, Hiroshima University, 2020.
- [35]. Ha JY, Iida N, Sato GT, et al. Experimental Investigation of the Entrainment into Diesel Spray. *SAE paper* 841078, 1984.
- [36]. Cossali GE, Brunello G and Coghe A. LDV Characterization of Air Entrainment in Transient Diesel Sprays. SAE paper 910178, 1991.
- [37]. Cossali, G. E., Coghe, A., and Brunello, G. Effect of Spray-Wall Interaction on Air Entrainment in a Transient Diesel Spray. SAE paper 930920, 1993.
- [38]. Araneo, L., Coghe, A., Brunello, G., and Cossali, G. E. Experimental Investigation of Gas Density Effects on Diesel Spray Penetration and Entrainment. *SAE paper* 1999-01-0525, 1999.
- [39]. Rajalingam, B. V., and Farrell, P. V. The Effect of Injection Pressure on Air Entrainment into Transient Diesel Sprays. *SAE paper* 1999-01-0523, 1999.
- [40]. Rhim, D.R., and Farrell, P. V. Air Flow Characteristics Surrounding Evaporating Transient Diesel Sprays. SAE paper 2002-01-0499, 2002.
- [41]. Sepret, V., Bazile, R., Marchal, M., and Couteau, G. Effect of Ambient Density and Orifice Diameter on Gas Entrainment by a Single-Hole Diesel Spray. *Exp. Fluids* 2010; 49:1293-1305.
- [42]. Bruneaux, G., Causse, M., and Omrane, A. Air Entrainment in Diesel-Like Gas Jet by Simultaneous Flow Velocity and Fuel Concentration Measurements, Comparison of Free and Wall Impinging Jet Configurations. SAE paper 2011-01-1828, 2011.
- [43]. Browne, K. R., Partridge, I. M. and Greeves, G. Fuel property effects on fuel/air mixing in an experimental diesel engine. SAE Paper 860223, 1986.

- [44]. Yatsufusa, T., Nishida, K., Yoshizaki, T. and Hiroyasu, H. Behaviors of D.I. diesel sprays with split in a model combustion chamber (1st report, effect of injection interval). *JSME transactions (B)*, 2000, 66(643), 919-925.
- [45]. Yatsufusa, T., Nishida, K., Yoshizaki, T. and Hiroyasu, H. Behaviors of D.I. diesel sprays with split in a model combustion chamber (2nd report, effect of injection mass ratio) *JSME transactions (B)*, 2000, 66(644), 1229-1236.
- [46]. Nishida, K., Murakami, N. and Hiroyasu, H. Holographic measurement of evaporating diesel sprays at high pressure and temperature. *JSME transactions (B)*, 1986, 30(259), 107-115.
- [47]. Song, Y. C., Shi, F. M., Gao, X. Y., Yan, F. C. and Chen, J. H. The Laser Interfero-Holographic and Tomographic Analysis of Concentration and Temperature Distribution of a Three-Dimensional Transient Diesel Spray, SAE Paper 941756, 1994.
- [48]. Heinze, T. and Schmidt, T. Fuel-air ratios in a spray, determined between injection and autoignition by pulsed spontaneous Raman spectroscopy. SAE Paper 892102, 1989.
- [49]. Rabenstein, F., Egermann, J. and Leipertz, A. Quantitative analysis of vapor phase structures in transient liquid fuel sprays. *Proc. COMODIA '98*, Kyoto Japan, July 1998, pp. 435- 440.
- [50]. Miles, P. C. Raman line imaging for spatially and temporally resolved mole fraction measurements in internal combustion engines. *Appli. Opti.*, 1999, 38(9), 1714-1732.
- [51]. Espey, C., Dec, J. E., Litzinger, T. A. and Samtavicca, D. A. Planar laser Rayleigh scattering for quantitative vapor-fuel imaging in a diesel jet. *Combust. and Flame* 1997; 109(1-2), 65-86.
- [52]. Idicheria, C. A. and Pickett, L. M. Quantitative mixing measurements in a vaporizing diesel spray by Rayleigh imaging. SAE Paper 2007-01-0647, 2007.
- [53]. Melton, L. A. Spectrally separated fluorescence emissions for diesel fuel droplets and vapor. *Appli. Opti.* 1983; 21(14), 2224-2226.
- [54]. Senda, J., Fukami, Y., Tanabe, Y. and Fujimoto, H. Visualization of evaporative diesel spray impinging upon wall surface by Exciplex fluorescence method. SAE Paper 920578, 1992.
- [55]. Felton, P. G., Bracco, F. V. and Bardsley, M. E. On the quantitative application of Exciplex fluorescence to engine sprays. SAE Paper 930870, 1993.

- [56]. Bruneaux, G., Verhoeven, D. and Baritaud, T. A. High-pressure diesel spray and combustion visualization in a transparent model diesel engine. SAE Paper 1999-01-3648, 1999.
- [57]. Zhang, Y., Nishida, K., and Yoshizaki, T., "Quantitative Measurement of Droplets and Vapor Concentration Distributions in Diesel Sprays by Processing UV and Visible Images," SAE Technical Paper 2001-01-1294, 2001.
- [58]. Chang Zhai, Yu Jin, Keiya Nishida, et al. Diesel spray and combustion of multi-hole injectors with micro-hole under ultra-high injection pressure – Non-evaporating spray characteristics. *Fuel* 2021; 283: 119322.
- [59]. Chang Zhai, Yu Jin, Qing Wu, et al. Diesel Spray Of Multi-Hole Injectors With Micro-Hole Under Ultra-High Injection Pressure-Evaporating Spray Characteristics. *Atomization and Sprays* 2022; 044-5110.
- [60]. Yokota H, Kamimoto T, Kosaka H, Tsujimura K. Fast burning and reduced soot formation via ultra-high pressure diesel fuel injection. SAE Technical Paper; 1991.
- [61]. Lavoie GA, Heywood JB, Keck JC. Experimental and theoretical study of nitric oxide formation in internal combustion engines. *Combustion science and technology* 1970;1(4):313-26.
- [62]. Flynn PF, Durrett RP, Hunter GL, zur Loye AO, Akinyemi OC, Dec JE, et al. Diesel combustion: an integrated view combining laser diagnostics, chemical kinetics, and empirical validation. SAE Technical Paper 1999-01-0509, 1999.
- [63]. Cung K, Bitsis DC, Briggs T, Kalaskar V, Abidin Z, Shah B, et al. Effect of Micro-Hole Nozzle on Diesel Spray and Combustion. SAE Technical Paper; 2018.
- [64]. Duraisamy G, Rangasamy M, Govindan N. A comparative study on methanol/diesel and methanol/PODE dual fuel RCCI combustion in an automotive diesel engine. *Renewable Energy* 2020; 145:542-56.
- [65]. Hasegawa R, Yanagihara H. HCCI combustion in DI diesel engine. SAE transactions 2003:1070-7.
- [66]. Kato T, Tsujimura K, Shintani M, Minami T, Yamaguchi I. Spray characteristics and combustion improvement of DI diesel engine with high pressure fuel injection. SAE Technical Paper; 1989.
- [67]. Kosaka H, Aizawa T, Kamimoto T. Two-dimensional imaging of ignition and soot formation processes in a diesel flame. *International Journal of Engine*

- Research 2005;6(1):21-42.
- [68]. Minato A, Tanaka T, Nishimura T. Investigation of premixed lean diesel combustion with ultra-high-pressure injection. SAE transactions 2005:756-64.
- [69]. Pierpont DA, Reitz RD. Effects of injection pressure and nozzle geometry on DI diesel emissions and performance. SAE transactions 1995:1041-50.
- [70]. Shundoh S, Kakegawa T, Tsujimura K, Kobayashi S. The effect of injection parameters and swirl on diesel combustion with high pressure fuel injection. SAE transactions 1991:793-805.
- [71]. Han Z, Uludogan A, Hampson G, et al. Mechanism of soot and NO_x emission reduction using multiple injection in a diesel engine. SAE paper 960633, 1996.
- [72]. Chen S. Simultaneous reduction of NO_x and particulate emissions by using multiple injections in a small diesel engine. SAE paper 2000-01-3084, 2000.
- [73]. Benajes J, Molina S and Garcia J. Influence of pre- and post-injection on the performance and pollutant emissions in a HD diesel engine. SAE paper 2001-01-0526, 2001.
- [74]. Osada H, Uchida N, Shimada K, et al. Reexamination of multiple fuel injections for improving the thermal efficiency of a heavy-duty diesel engine. SAE paper 2013-01-0909, 2013.
- [75]. Arrègle J, Pastor J, López JJ, et al. Insights on postinjection-associated soot emissions in direct injection diesel engines. *Combust Flame* 2008; 154: 448–461.
- [76]. Desantes JM, Arrègle J, López JJ, et al. A comprehensive study of diesel combustion and emissions with post-injection. SAE paper 2007-01-0915, 2007.
- [77]. Kim J, Kakami S, Nishida K, et al. Effects of ratio and dwell of split injection on fuel spray and mixture formation process under evaporating, non-reacting condition. SAE paper 2019-01-2323, 2019.
- [78]. Payri R, Salvador FJ, Abboud R, et al. Study of evaporative diesel spray interaction in multiple injections using optical diagnostics. *Applied Thermal Engineering* 2020;176: 115402.
- [79]. Schoppe D, Stahl C, Kruger D, et al. Servo-driven piezo common rail diesel injection system. *ATZ Autotechnol* 2012; 12: 42-47.
- [80]. Liu Y and Reitz RD. Optimizing HSDI diesel combustion and emissions using multiple injection strategies. SAE paper 2005-01-0212, 2010.
- [81]. Wu, G.; Zhou, X.; Li, T. Temporal Evolution of Split-Injected Fuel Spray at

- Elevated Chamber Pressures. *Energies* **2019**, *12*, 4284.
- [82]. Bruneaux G and Maligne D. Study of the mixing and combustion processes of consecutive short double diesel injections. *SAE Int J Engines* 2009; 2: 1151–1169.
- [83]. Pickett LM, Kook S and Williams TC. Transient liquid penetration of early-injection diesel sprays. *SAE Int J Engines* 2018; 2(1): 785-803.
- [84]. Skeen S, Manin J and Pickett LM. Visualization of ignition processes in high-pressure sprays with multiple injections of n-Dodecane. *SAE Int J Engines* 2015; 8(2): 696–715.
- [85]. Tao F, Reitz RD, Foster DE, et al. Nine-step phenomenological diesel soot model validated over a wide range of engine conditions. *Int J Therm Sci* 2009; 48(6):1223–12 34.
- [86]. Herfatmanesh MR, Lu P, Attar MA, et al. Experimental investigation into the effects of two-stage injection on fuel injection quantity , combustion and emissions in a high-speed optical common rail diesel engine. *Fuel* 2013; 109: 137-147.
- [87]. Kim D and Bae C. Application of double-injection strategy on gasoline compression ignition engine under low load condition. *Fuel* 2017; 203: 792–801.
- [88]. Han S, Hyun S and Sik C. Effects of multiple-injection strategies on overall spray behavior , combustion , and emissions reduction characteristics of biodiesel fuel. *Appl Energy* 2011; 88(1): 88–98.
- [89]. Nishida K, Imanishi H, Sato T, et al. Wall impingement behavior of the diesel spray with split injection. *JSAE Trans* 1999; 30(3): 17–23.
- [90]. Hahn DW. Light scattering theory. Department of Mechanical and Aerospace Engineering, University of Florida 2009.
- [91]. Yang K. Effects of Piston Cavity Impingement and Split Injection on Mixture Formation and Combustion Processes of Diesel Spray. Doctor degree dissertation Hiroshima University, 2018.
- [92]. Siebers DL. Liquid-phase fuel penetration in diesel sprays. SAE transactions 1998:1205-27.
- [93]. Panigrahi PK and Muralidhar K. Schlieren and shadowgraph methods in heat and mass transfer. Springer; 2012.

- [94]. Espey C, Dec JE, Litzinger TA, et al. Planar Laser Rayleigh Scattering for Quantitative Vapor-Fuel Imaging in a Diesel Jet. *Combustion and Flame* 1997; 109: 65-78.
- [95]. Johnston S. Precombustion Fuel/Air Distribution in a Stratified Charge Engine Using Laser Raman Spectroscopy. *SAE technical paper* 790433, 1979.
- [96]. Sawersyn JP, Sochet L, Desenne D, et al. A Study of Spatial Distribution of Molecular Species in an Engine by Pulsed Multichannel Raman Spectroscopy. *Proc. 21st Symposium (International) on Combustion*, 1986,491-496.
- [97]. Miles P and Hinze P. Characterization of the Mixing of Fresh Charge with Combustion Residuals Using Laser Raman Scattering with Broadband Detection. *SAE technical paper* 981428, 1998.
- [98]. Reising HH. Application of Spontaneous Raman Scattering for Measurements of Thermal Non-Equilibrium in High-Speed Mixing and Combustion. Dissertation, The University of Texas, 2017.
- [99]. Talley D, Verdick J, Lee S, et al. Accounting for laser sheet extinction in applying PLLIF to sprays. *AIAA* 1996; 396-469.
- [100]. Seitzman JM, Hanson RK. Planar fluorescence imaging in gases. *Instrumentation for flows with combustion* 1993:405.
- [101]. Andresen P, Meijer G, Schlüter H, et al. Fluorescence imaging inside an internal combustion engine using tunable excimer lasers. *Applied optics* 1990;29(16):2392-404.
- [102]. Melton LA and Verdick JF. Vapor/Liquid Visualization for Fuel Sprays. *20th Symposium (International) on Combustion* 1984, 217-222.
- [103]. Melton LA. Spectrally Separated Fluorescence Emissions for Diesel Fuel Droplets and Vapor. *Applied Optics* 1983, 22(14):2224-2226.
- [104]. Melton LA and Verdick JF. Vapor/Liquid Visualization in Fuel Sprays. *20th Symposium (International) on Combustion* 1985, 1283-1290.
- [105]. Leidenberger U, Hüttl C, Haugg S, et al. Application of Laser-Induced Exciplex Fluorescence with Alternative Diesel Fuels. *23rd Annual Conference on Liquid Atomization and Spray Systems* 2010.
- [106]. Senda J, Kanda T, Kobayashi M, et al. Quantitative Analysis of Fuel Vapor Concentration in Diesel Spray by Exciplex Fluorescence Method. *SAE technical paper* 970796, 1997.

- [107]. Senda J, Kobayashi M, Iwashita S, et al. Modeling of Diesel Spray Impingement on a Flat Wall. *SAE technical paper* 941894, 1994.
- [108]. Senda J, Tanabe Y, Fujimoto H, et al. Visualization of Evaporative Diesel Spray Impinging Upon Wall Surface by Exciplex Fluorescence Method. *SAE technical paper* 920578, 1992.
- [109]. Bruneaux G. Liquid and Vapor Spray Structure in High-Pressure Common Rail Diesel Injection. *Atomization and Sprays* 2001; 11: 533-556.
- [110]. Bruneaux G. Mixing Process in High Pressure Diesel Jets by Normalized Laser Induced Exciplex Fluorescence Part I: Free Jet. *SAE technical paper* 2005-01-2100, 2005.
- [111]. Bruneaux G. Combustion Structure of Free and Wall-Impingement Diesel Jets by Simultaneous Laser-Induced Fluorescence of Formaldehyde, Poly-Aromatic Hydrocarbons, and Hydroxides. *International Journal of Engine Research* 2008; 9:249-265.
- [112]. Andersson M, Yamaguchi A and Wang H. Imaging of Gasoline-like Sprays with Planar Laser-induced Exciplex Fluorescence using a Stereoscopic Imaging System. *28th Conference on Liquid Atomization and Spray Systems* 2017, 546.
- [113]. Chraplyvy AR. Nonintrusive Measurements of Vapor Concentrations inside Sprays. *Appl. Opt.* 1981; 20(15): 2620-2624.
- [114]. Suzuki M, Nishida K and Hiroyasu H. Simultaneous Concentration Measurement of Vapor and Liquid in an Evaporating Diesel Spray. In: *SAE Technical Paper*. 1993.
- [115]. https://www.onosokki.co.jp/English/hp_e/products/keisoku/automotive_test/fj_system.htm
- [116]. Ishikawa, Satoshi, et al. Measurement of rate of multiple injection in CDI diesel engines. No. 2000-01-1257. *SAE Technical Paper*, 2000.
- [117]. Yamakawa M, Takaki D, Li T, et al. Quantitative measurement of liquid and vapor phase concentration distributions in a D.I. gasoline spray by the laser absorption scattering (LAS) technique. *SAE Tech Pap.* Epub ahead of print 2002. DOI: 10.4271/2002-01-1644.
- [118]. Itamochi M, Matsuo T, Li K, et al. Laser Absorption Scattering Technique Using Tracer-Doped Fuel (Tracer LAS) for Quantitative Measurement of Mixture Concentration Distribution in Diesel Spray. In: *ILASS-ASIA*. 2015.

- [119]. Zhang Y, Ito T, and Nishida K. Characterization of Mixture Formation in Split-Injection Diesel Sprays via Laser Absorption- Scattering (LAS) Technique. SAE Technical Paper 2001-01-3498, 2001, doi:10.4271/2001-01-3498.
- [120]. Gao J, Nishida K, Moon S, et al. Characteristics of Evaporating Diesel Spray: A Comparison of Laser Measurements and Empirical/Theoretical Predictions. *SAE Int. J. Engines* 2(1):805-818, 2009, doi:10.4271/2009-01-0854.
- [121]. Li KC, Matsuo T, Ido M, et al. Effect of Wall Impingement on Diesel Spray Characteristics. The 16th Annual Conference of ILASS-Asia, Dec 18-19, 2013, Nagasaki, Japan.
- [122]. Ray SC, Kim J, Kakami S, et al. Effects of Dwell Time of Split Injection on Mixture Formation and Combustion Processes of Diesel Spray. *Proc IMech Eng Part D: J Automobile Engineering*. October 2021. doi:[10.1177/09544070211053693](https://doi.org/10.1177/09544070211053693).
- [123]. Hammond DC. Deconvolution technique for line-of-sight optical scattering measurements in axisymmetric sprays. *Appli Opti* 1981; 20(3): 493-498.
- [124]. Zhang Y. A study on mixture formation in diesel spray with split-injection strategies. Dissertation of Hiroshima University, 2001.
- [125]. Safiullah, Mahmud R, Nishida K, et al. Experimental and computational study of diesel spray under nonevaporating and evaporating conditions - Effects of nozzle hole diameter and injection pressure. *At Sprays* 2020; 30: 627–649.
- [126]. Ray SC, Kim J, Kakami S, et al. Effects of split ratio of diesel spray injection on mixture formation and combustion process. *Proc IMech Eng Part D: J Automobile Engineering* 2021; 235(14): 3404–3415.
- [127]. Kuichun LI. Effects of Wall Impingement and Multiple Injection on Mixture Formation and Combustion Processes of Diesel Spray. Doctor degree dissertation, Hiroshima University, 2014.
- [128]. Morawski P, Coutinho JAP and Domanska U. High Pressure (Solid + Liquid) Equilibria of n-alkane Mixtures Experimental Results, Correlation and Prediction. *Fluid Phase Equilibria* 2005; 230:72-80.
- [129]. Milhet M, Pauly J, Coutinho JAP, et al. Liquid Solid Equilibria under High Pressure of Tetradecane + Pentadecane and Tetradecane + Hexadecane Binary Systems. *Fluid Phase Equilibria* 2005; 235:173-181.
- [130]. Zhang Y and Nishida K. Vapor Distribution Measurement of Higher and Lower Volatile Components in an evaporating Fuel Spray via Laser Absorption

- Scattering (LAS) Technique. *Combustion Science and Technology* 2007; 179(5).
- [131]. Zhao H and Ladommatos N. Optical diagnostics for soot and temperature in diesel engines. *Prog. Energy Combust Sci* 1998; 24(3): 221–55.
- [132]. Hottel H and Broughton F. Determination of True Temperature and Total Radiation from Luminous Gas Flames. *Ind and Eng. Chem.* 1932; 4(2):166-174.
- [133]. Svensson, K.I., Mackrory, A.J., Richards, M.J., and Tree, D.R. Calibration of an RGB, CCD Camera and Interpretation of its Two-Color Images for KL and Temperature. *SAE technical paper* 2005-01-0648, 2005.
- [134]. Zhang Y and Nishida K. Imaging of Vapor/Liquid Distributions of Split-Injected Diesel Spray in a Two-Dimensional Model Combustion Chamber. *Combust. Sci. and Tech.* 2004; 176: 1465-1471.
- [135]. Yin L, Lundgren M, Wang Z, et al. High efficient internal combustion engine using partially premixed combustion with multiple injections. *Appl Energy* 2019; 233–234:516–523.
- [136]. Bower GR and Foster DE. A Comparison of the Bosch and Zuech Rate of Injection Meters. SAE technical paper 910724, 1991.
- [137]. Bin Abdullah MFE, Toyama Y, Takahara K, et al. Optical Diagnostics of Inversed-Delta Rate Shaping Diesel Spray Flame towards Reduction of Late Combustion. SAE paper 2018-01-1793, 2018.
- [138]. Nishida K, Matsuo T, Yang Y, et al. Spray, Mixture and Combustion Characteristics of Small Injection Amount Fuel Spray Injection by Hole Nozzle for Diesel Engine. SAE technical paper 20168064, 2016.
- [139]. Yang K, Yamakawa H, Nishida K, et al. Effect of split injection on mixture formation and combustion processes of diesel spray injected into two-dimensional piston cavity. *Proc IMech Eng Part D: J Automob Engineering* 2018; 232(8): 1121–36.
- [140]. Li T, Zhang Y, Nishida K, et al. Characterization of Mixture Formation Processes in DI Gasoline sprays with Split Injection Strategy via Laser Absorption Scattering (LAS) technique. SAE paper 2003-01-3161, 2003.
- [141]. Zhang X, Li T, Ma P, et al. Spray combustion characteristics and soot emission reduction of hydrous ethanol diesel emulsion fuel using color-ratio pyrometry. *Energies* 2017; 10(12): 1-13.
- [142]. Matsui Y, Kamimoto T and Matsuoka S. A study on the time and space resolved

- measurement of flame temperature and soot concentration in a D. I. diesel engine by the two-color method. SAE paper 0148-7191, 1979..
- [143]. Pickett LM and Siebers DL. Soot in diesel fuel jets : effects of ambient temperature , ambient density, and injection pressure. *Combust Flame* 2004; 138: 114-135.
- [144]. Tree DR and Svensson KI. Soot processes in compression ignition engines. *Prog. Energy Combust Sci* 2007; 33:272–309.
- [145]. López JJ, Martín J, García A, et al. Implementation of two color method to investigate late cycle soot oxidation process in a CI engine under low load conditions. *Appl Therm Eng* 2017;113:878–90.
- [146]. Kamimoto T, Uchida N, Aizawa T, et al. Diesel flame imaging and quantitative analysis of in-cylinder soot oxidation. *International Journal of Engine Research*. 2017;18(5-6):422-435.
- [147]. Yang K, Nishida K, Ogata Y, et al. Characteristics of fuelevaporation, mixture formation and combustion of 2D cavity impinging spray under high-pressure split injection. *Fuel* 2018; 234: 746-756.
- [148]. Kim J, Kakami S, Nishida K, et al. Effects of positive and negative dwell times of split spray development and mixture formation processes. SAE paper 2019-32-0596, 2019.
- [149]. Kim J, Kong L, Nishida K, et al. Comparison of fuel concentration distribution of diesel spray between single- and multi-hole injectors under evaporating , non-reacting condition. In: *14th triennial international conference on liquid atomization and spray systems ICLASS*, Chicago, IL, USA, 22–26 July 2018.
- [150]. Kook S, Pickett L and Musculus M. Influence of diesel injection parameters on end-of-injection liquid length recession. *SAE Int. J. Engines* 2(1):1194-1210, 2009.
- [151]. Lachaux T and Musculus M. In-cylinder unburned hydrocarbon visualization during lowtemperature compression-ignition engine combustion using formaldehyde PLIF. *Proc Combust Ins.* 2007; 31:2921-2929.
- [152]. Heywood J. *Internal combustion engines fundamental*. McGrawHill.
- [153]. Kosaka H, Aizawa T and Kamimoto T. Two-dimensional imaging of ignition and soot formation processes in a diesel flame. *International Journal of Engine Research*. 2005;6(1):21-42.
- [154]. Yang K, Yamakawa H, Nishida K, et al. Characteristics of free spray

- development, mixture formation, and combustion under high-pressure split injection. *Atomization and Sprays*. 2018;28(3):217-240.
- [155]. Du C, Andersson S and Andersson M. Time-Resolved Liquid and Vapor Phase Distribution Measurement in Diesel Sprays Using a Light Absorption Scattering Technique. *ILASS – Europe 2016, 27th Annual Conference on Liquid Atomization and Spray Systems*, 4-7 September 2016, Brighton, UK.
- [156]. Tian J, Zhao M, Long W, et al. Experimental study on spray characteristics under ultra-high injection pressure for DISI engines. *Fuel* 2016; 186: 365-374.
- [157]. Matsuo T, Li K, Itamochi M, et al. Tracer LAS Technique for Quantitative Mixture Concentration Measurement of Evaporating Diesel Spray. *ILASS Asia 2014, 17th annual conference on liquid atomization and spray system-Asia*, Shanghai, China.
- [158]. Kim J, Kakami S, Jin Y, et al. Internal Fuel Flow, Near-Field and Far-Field Spray Evaluation, and Mixture Formation Characteristics of Diesel Injectors-A Comparison between Multi-and Single Hole Injectors. SAE Technical Paper 2019-01-0273, 2019.
- [159]. Safiullah, Nishida K and Ogata Y. Evaporation and mixture formation characteristics of diesel spray under various nozzle hole size and injection pressure condition employing similar injection rate profile. *International Communications in Heat and Mass Transfer* 2021; 123.
- [160]. Gao J and Nishida K. Laser absorption-scattering technique applied to asymmetric evaporating fuel sprays for simultaneous measurement of vapor/liquid mass distributions. *Applied Physics B* 2010; 101: 433-443.